POOL BOILING ON NANO-FINNED SURFACES

A Thesis

by

SHARAN RAM SRIRAMAN

Submitted to the Office of Graduate Studies of
Texas A&M University
in partial fulfillment of the requirements for the degree of

MASTER OF SCIENCE

December 2007

Major Subject: Mechanical Engineering

POOL BOILING ON NANO-FINNED SURFACES

A Thesis

by

SHARAN RAM SRIRAMAN

Submitted to the Office of Graduate Studies of
Texas A&M University
in partial fulfillment of the requirements for the degree of

MASTER OF SCIENCE

Approved by:

Chair of Committee,   Debjyoti Banerjee
Committee Members,   Kalyan Annamalai
                        Arul Jayaraman
Head of Department,   Dennis O' Neal

December 2007

Major Subject: Mechanical Engineering

ABSTRACT

Pool Boiling on Nano-Finned Surfaces. (December 2007)

Sharan Ram Sriraman, B.E., Hindustan College of Engineering, India

Chair of Advisory Committee: Dr. Debjyoti Banerjee

The effect of nano-structured surfaces on pool boiling heat transfer is explored in this study. Experiments are conducted in a cubical test chamber containing fluoroinert coolant (PF5060, Manufacturer: 3M Co.) as the working fluid. Pool boiling experiments are conducted for saturation and subcooled conditions. Three different types of ordered nano-structured surfaces are fabricated using Step and flash imprint lithography on silicon substrates followed by Reactive Ion Etching (RIE) or Deep Reactive Ion Etching (DRIE). These nano-structures consist of a square array of cylindrical nanofins with a longitudinal pitch of 1 mm, transverse pitch of 0.9 mm and fixed (uniform) heights ranging from 15 nm – 650 nm for each substrate. The contact angle of de-ionized water on the substrates is measured before and after the boiling experiments. The contact-angle is observed to increase with the height of the nano-fins. Contact angle variation is also observed before and after the pool boiling experiments.

The pool boiling curves for the nano-structured silicon surfaces are compared with that of atomically smooth single-crystal silicon (bare) surfaces. Data processing is performed to estimate the heat flux through the projected area (plan area) for the nano-patterned zone as well as the heat flux through the total nano-patterned area, which includes the

surface area of the fins. Maximum heat flux (MHF) is enhanced by ~120 % for the nano-fin surfaces compared to bare (smooth) surfaces, under saturation condition. The pool boiling heat flux data for the three nano-structured surfaces progressively overlap with each other in the vicinity of the MHF condition. Based on the experimental data several micro/nano-scale transport mechanisms responsible for heat flux enhancements are identified, which include: "microlayer" disruption or enhancement, enhancement of active nucleation site density, enlargement of cold spots and enhancement of contact angle which affects the vapor bubble departure frequency.

DEDICATION

To God for His blessings.

To Amma for her endless love, support and encouragement.

To Kaushik and the rest of my family for their unconditional love.

To Divya for her constant love, patience and motivation.

To Dr. Debjyoti Banerjee for his inspiration and support.

ACKNOWLEDGEMENTS

First, I would like to express my heartfelt gratitude to Dr. Debjyoti Banerjee for identifying my potential and for his guidance and support throughout the course of my research at Texas A&M University. He has undoubtedly been a great mentor for my academic and professional pursuits.

I would like to express my gratitude to Dr. Kalyan Annamalai and Dr. Arul Jayaraman for being a part of my thesis committee. I would like to thank Dr. Hee Seok Ahn for providing me guidance with respect to the boiling apparatus setup. I appreciate the guidance provided by Vijaykumar Sathyamurthi in the laboratory. I would also like to thank Rudy, Jim and Manoj for assisting me in conducting the boiling experiments.

I would like to thank Dr. Marylene Palard at the Microelectronics Research Center (The University of Texas at Austin) for guiding me through and assisting me in the nano-fabrication process. I would also like to thank the staff at the same labs for the training they provided as well as constant equipment support.

I would also like to thank Dr. Orla Wilson at the Materials Characterization Facility and Dr. Amit Bhasin at the Texas Transportation Institute for allowing me to use their laboratory facilities at Texas A&M University for my research.

Thanks also go to my colleagues and friends in the research group and to the Mechanical Engineering Department faculty and staff for making my time at Texas A&M University a great experience. I also want to extend my gratitude to the National Science Foundation (NSF) for providing the funding for my research.

I would like to thank Kitchu, Sailaja, Arya, Sundu, Shobha and Pratik for being the best relatives. Finally, thanks to my Amma and Kaushik for their encouragement and love, and to Divya for her never-ending love, patience, support and motivation.

NOMENCLATURE

A_{Cu} - Top circular area of copper block (cm^2)

A_b - Total bare surface area on the test surface (cm^2)

A_w - Test surface area exposed to boiling (cm^2)

A_n - Total area of nano-patterned squares on the test surface (cm^2)

A_{nc} - Total nano-finned area exposed to boiling (cm^2)

h - Height of nano-fin (cylindrical or frustum of cone) (nm)

k_{Cu} - Thermal conductivity of copper (W/mK)

l - Slant height of nano-fin (frustum of cone) (nm)

n - Number of nano-fins per nano-finned square

N - Number of nano-finned squares on the test surface

q_{Cu}'' - Heat flux through the copper block (W/cm^2)

q_b'' - Heat flux through the smooth silicon surface (W/cm^2)

q_w'' - Heat flux through the test surface (W/cm^2)

q_n'' - Heat flux through the nano-patterned plan area (W/cm^2)

q_{nc}'' - Heat flux through the nano-patterned area (W/cm^2)

q_{CHF}'' - Heat flux at CHF (Critical Heat Flux) (W/cm^2)

Q_{Cu} - Total heat passing through the copper block (W)

Q_w - Total heat through the exposed test surface (W)

r - Radius of cylindrical nano-fin (nm)

r_1 - Smaller radius of nano-fin (frustum of cone) (nm)

r_2	- Larger radius of nano-fin (frustum of cone) (nm)
T_{Cu}	- Temperature of top of copper block (°C)
T_w	- Wall temperature of test surface (°C)
T_{CHF}	- Temperature at CHF (°C)
T_{sat}	- Saturation temperature of test liquid – PF5060 (56 °C)
T_2	- Thermocouple2 (0.125" from top of Cu block) temperature reading (°C)
T_9	- Thermocouple9 (0.875" from top of Cu block) temperature reading (°C)
ΔT	- Temperature difference between T_2 and T_9 (°C)
$(\Delta T)_{wall}$	- Wall superheat (°C)
$(\Delta T)_{Sub}$	- Test liquid (PF5060) sub-cooling (°C)
ω_q	- Uncertainty in heat flux (W/cm^2)
ω_k	- Uncertainty in thermal conductivity of copper (W/mK)
ω_{T2}	- Uncertainty in temperature reading T_2 (°C)
ω_{T9}	- Uncertainty in temperature reading T_9 (°C)
$\omega_{\Delta x}$	- Uncertainty in Δx measurement (cm)
x	- $q_w"/q_b"$
Δx	- Distance between temperature measurement positions, 2 and 9 (cm)
δ_0	- Thickness of film at the interline region (nm)

TABLE OF CONTENTS

LIST OF TABLES

LIST OF FIGURES

Page

1. INTRODUCTION

Recent advances in technology have led to the development of electronic devices with enhanced speeds and augmented computational capabilities with a concomitant increase in power density. Advances in manufacturing capabilities have enabled the shrinking of the device sizes. The combined effect of increasing power and speed as well as shrinking device size has resulted in an ever-increasing requirement for dissipation of high heat fluxes. Increase in power density causes additional requirements for cooling these devices. This presents a tough challenge as far as cooling schemes for these systems are concerned.

Thermal considerations in the design of high-heat-flux electronic devices play a major role because the computational performance is limited by the operating temperature of these devices. Literature data in this field can be found as early as the 1920s [1]. Conventional cooling schemes include natural and forced convection. While more efficient cooling was realized with forced convection compared to natural convection, researchers predict that direct liquid cooling accompanied with phase-change is required to meet the cooling needs of future devices.

_____

This thesis follows the style of *IEEE Transactions on Components and Packaging Technologies.*

It is expected that the average heat flux for high performance chips will exceed 150 W/cm^2 in the near future with non-uniformities in power dissipation resulting in hot-spots with heat fluxes approaching 1 kW/cm^2 [2]. Actual application of boiling in electronics applications was noted as early as 1935 by Mouromtseff and Kozanowski [3] where they refer to sub-cooled boiling of the coolant for cooling high power vacuum tubes.

Boiling is simply the rapid vaporization of liquid when the liquid is in contact with a heated surface. For boiling to occur, the fundamental requirement is that the heated surface temperature should exceed the saturation temperature of the liquid in contact. The temperature difference between the two at any time is typically called the "*superheat*" or *"wall superheat"*. During boiling incipience, the local superheat causes the first set of bubbles to nucleate. The nucleated bubbles grow in size until the buoyancy forces overcome the capillary forces. When buoyancy forces exceed the capillary forces (as well as the inertia and drag forces from the liquid and vapor phases) these vapor bubbles are released from the surface in to the pool of liquid. The rising vapor bubbles drag a part of the bulk fluid in contact with the bubble to the surface of the liquid pool. Thus, there is a constant pumping action which is the principle of operation of these *" virtual thermosyphons"* [4]. The advantage of pool boiling over flow boiling systems is that no external pumping source is required for coolant flow.

As the surface temperature is increased, more vapor bubbles are formed (bubble nucleation) and released thus dissipating increasing amounts heat from the heated surface into the liquid pool. There is however a limiting point when too many bubbles coalesce at the surface thus interfering with the supply of bulk fluid to the surface. This occurs because vapor bubbles are formed at a faster rate than they are released. Photographic studies [5, 6] suggest that these bubbles merge laterally to form "vapor-mushrooms" and sometimes vertically to form "vapor-jets". These vapor mushrooms are periodically formed and then swept away by buoyancy forces and/or liquid drag forces. This process reduces the liquid supply to the surface ultimately resulting in the pool boiling system to transition into film boiling. When film boiling occurs the pool boiling heat flux is reduced from that of the nucleate boiling. In this regime, the vapor film on the surface acts like an insulator and reduces the film boiling heat flux. Until this transition to film boiling occurs, the pool boiling heat flux increases with wall temperature (or wall superheat). The point just prior to the transition is termed as the "Maximum Heat Flux (MHF)" or the "Critical Heat Flux (CHF)". The range of points from boiling incipience to CHF is of particular interest to researchers because of the ability of the surface to dissipate large amounts of heat with only a modest increase in surface temperature.

Boiling literature dates back to 1756 when Ledienfrost [1] reported his observation on boiling of water droplets. In this paper [7], he noted that the rate of evaporation of a water droplet on a red-hot iron spoon would go up as the temperature of the spoon was

increased but with a limiting point after which the evaporation rate decreased. Subsequently, Nukiyama [8] pioneered the "boiling curve" by plotting pool boiling heat flux as a function of the wall superheat. He showed that contrary to the conclusions derived by previous researchers, the heat transfer coefficient is not a monotonic function of superheat. Through experimental results from the boiling on platinum, nickel, nichrome wires as well as on the flat surface of a copper cylinder, he proved the existence of CHF. Further, he also proved the existence of minima in heat flux (Leidenfrost point), and thus pioneered the boiling curve.

Coolant selection for pool boiling plays an important role in determining the efficacy of the cooling system. Water is a coolant with excellent transport properties. Its corrosive nature and poor dielectric strength renders it unsuitable for application in electronic component cooling in spite of its high latent heat of vaporization. This paved way for the increasing popularity of *"fluoroinerts"*. Compared to properties of water, these fluids have low latent heat of vaporization and specific heat. In spite of this shortcoming, the high dielectric strength and compatibility with materials (e.g. low corrosiveness) have resulted in their widespread use for cooling of electronic equipment. PF5060, FC-72 and FC-87 (Manufacturer 3M Co., MN) are commonly used fluoroinert coolants. Since their thermal transport properties are not as efficient as that of water, system modifications have to be made to improve their performance. Boiling heat flux can be improved by modifying the surface properties, increasing liquid sub-cooling and by increasing the liquid pressure [9].

In their review, Rohsenow et al. [10] observed that the effect of surface characteristics on pool boiling heat transfer depends on the thermophysical properties of the surface, and surface micro-geometry. This occurs due to the interaction between the solid, liquid and the vapor interfaces. Numerous surface modification techniques have been carried out and their effect on nucleate boiling heat transfer have been studied. Porous surfaces have been of great interest to researchers because of their potential for heat flux enhancement. Examples of porous surfaces studied include a thin layer of porous covering, layers of wire meshes or coatings of metallic granules [11-15]. Using one such surface, Afgan and Jovic [11] observed a two-fold increase in $q"_{CHF}$ compared to the bare surface where $q"_{CHF}$ is the heat flux at the CHF point. A comprehensive study was undertaken by Kaviany et al. [16] where different modulated porous layer coatings were fabricated, experimentally studied and possible heat transfer modes explained. They showed that one such coating with dual modulated structure height demonstrated a $q"_{CHF}$ of 762 kW/m^2 compared to 245 kW/m^2 of the bare surface which is a three-fold increase. In the recent past, Vemuri and Kim [17] studied the effect of nano-porous surfaces on boiling. They found a 30 % decrease in the incipient superheat. It is interpreted that the nano-porous surface increases the vapor/gas entrapment column and active nucleation site density and thus reduces the incipient superheat compared to the plain aluminum surface. Incipient superheat occurs because of the highly wetting nature of the fluoroinerts compared to less-wetting fluids like water. They flood cavities that normally serve as vapor entrapment sites. In such cases, bubble nucleation occurs from smaller micro-cavities at higher superheats. Chang and You [18] studied the effects of micro-

porous surfaces on heat transfer. They estimated the superheated liquid layer to be 100 μm. Coatings that were thinner than this value were classified as "micro-porous" and the rest as "porous". The micro-porous surfaces displayed a greater enhancement in heat flux at CHF compared to the porous surfaces and bare surfaces.

Studies were also undertaken by Honda et al. to observe the effect of micro-pin fins on silicon surfaces [19, 20]. The micro-pin fins were fabricated using dry etching technique. It was found that square pin fins with the largest width and height exhibited q_{CHF}" values four times as high as that of smooth surfaces with sub-cooling of 45 K. They further studied the effect of micro-fins and submicron-scale roughness on boiling of FC-72. They found that the fins with submicron-scale roughness showed the greatest enhancement (1.8 – 2.3 times that of the bare surface) depending on the degree of sub-cooling. Further, wall superheats at CHF for the enhanced surfaces were lower than the accepted maximum limit of 85 °C for Large Scale Integration (LSI) chips. Rainey and You [21] studied the effect of porous layer coatings on square pin-finned surfaces. Tests were performed for different fin lengths. The authors reported that the enhancement in CHF depended on the increase in active sites of the coating rather than the increase in surface area of the fins.

Joshi et al. [22] studied seven different modified surfaces on pool boiling using PF5060 and de-ionized water. The enhanced surfaces included a silicon surface roughened by dry etching, a carbon nanotube (CNT) coated surface, a surface with silicon pin-fin

microstructures, a surface with CNT pin-fin array and two 3D silicon surfaces (one coated with CNTs on the top surface). They found that, using PF5060, the silicon 3D structure exhibited the greatest enhancement of 2 times the q_{CHF}" that of a smooth surface. The CNT coated surfaces showed enhancement in heat flux only at lower superheats. Ujereh et al. [23] studied the effect of Multi-Walled-Carbon-Nano-Tubes (MWCNT) coating on pool boiling. The nanotubes were 30 nm in diameter and 20-30 μm in length. FC-72 was used as the working fluid and the coating was shown to enhance the CHF by 60 % compared to bare surface.

1.1 Motivation for the study

The literature review above shows that pool boiling is a complex phenomenon with numerous variables (parameters) affecting the boiling heat flux. The effect of pressure, dissolved gas, heater orientation, and sub-cooling has been studied to great depths. The thermal transport phenomena are complex and coupled non-linearly. Different types of surface enhancements have proven to improve the heat transfer. Literature data shows that nano-scale modifications have an effect on pool boiling [17, 22, 23] but the nano-scale transport properties are not yet well understood. Existing theories of pool boiling are largely based on continuum models (e.g., Hsu's criteria for bubble nucleation [24]). Since non-continuum flow occurs in the nano-structured surfaces the existing pool boiling theories are not applicable for these conditions. Hence, there is a pressing need for developing new theories for pool boiling on nano-structured surfaces.

1.2 Objectives

The objective of the present work is to experimentally study the effect of nano-scale surface perturbations on pool boiling heat transfer. The experimental results can be used to identify the dominant nano-scale transport mechanisms during pool boiling. Pool boiling experiments are run on different types of nano-structured surfaces and the results are compared with that of atomically smooth (bare) surfaces, for both nucleate and film boiling. The experiments are performed for saturated as well as various sub-cooled conditions. Suitable geometries and fabrication techniques are therefore identified for obtaining the different nano-structured surfaces.

Pool boiling experiments are performed for three types of nano-structured silicon surfaces and the results are compared with that of an atomically smooth single-crystal silicon surface. These surfaces are patterned to obtain an array of cylindrical *"nano-fins"* with a definite diameter, height, and pitch (longitudinal as well as transverse pitch). The first surface is denoted as *"100 nm"* to denote the nano-fin height of 100 nm. The average diameter of the fins is 200 nm. The second test surface, denoted as *"336 nm"*, contains nano-fins in the form of frustums of cones with 336 nm height with the diameter ranging from 100 nm and 65 nm at the top and bottom respectively. The third test surface is denoted as *"259 nm"*. This surface has cylindrical nano-fins of 259 nm in height and 186 nm in diameter. All test surfaces have longitudinal and transverse pitches of 0.9 μm and 1 μm respectively. Pool boiling experiments are run on the above test surfaces and also on a bare silicon test surface and the results are compared. Experiments

are run under saturation, 10 °C sub-cooling and 20 °C sub-cooling test conditions. Experiments are also repeated 2-3 times to check for repeatability of results.

In addition to this, the effect of the nano-fin height on the contact angles for de-ionized water and PF5060 is studied. The minimum superheat required for a bubble to grow from a cavity is inversely proportional to the smallest radius the vapor bubble attains during heterogeneous nucleation [9]. Literature data shows that during boiling incipience, the initial vapor embryo size depends on the contact angle between the liquid and the test surface [9]. Fluoroinerts are highly wetting fluids that make very low contact angles with most surfaces. Larger cavities that tend to be vapor entrapment sites for less-wetting liquids with larger contact angles (example water) get flooded by fluoroinerts and boiling incipience occurs only at smaller surface cavities. When flooding of cavities occurs, boiling incipience is difficult to predict. Fluoroinerts thus experience an "incipience temperature drop" where the heated surface would need unusually high wall temperatures before boiling initiates. Upon incipience, the vapors bubbles extract the heat from the surface which leads to a sudden drop in the surface temperature. This incipience temperature drop causes a "thermal shock" to the component and is undesirable in electronic cooling. Thus, the liquid-surface interaction plays an important role in boiling studies. Hence the effect of surface modifications on the contact angles is also studied.

1.3 Document overview

The second section of this thesis describes the nano fabrication of the enhanced test surfaces in detail. The third section explains the pool boiling experimental setup and procedure. The data obtained from the experiments is analyzed and the corresponding results are discussed in the fourth section. The final section reports the conclusions derived from this investigation and identifies the future directions for research.

2. NANO-FABRICATION OF TEST SURFACES

The aim of the present investigation is to explore the effect of nano-scale surface perturbations on pool boiling heat flux. The surface modification schemes should be capable of creating a definite pattern of features and not a random nano-scale roughness. For this purpose a simple square array of nano-scale silicon pillars (or *"nano-fins"*) were chosen as the test features. This array was required to have a definite diameter, height and pitch. A suitable patterning method had to be selected to fabricate these features on silicon substrates. A number of advantages including ease of processing and relatively lower overall costs encouraged the use of Step and Flash Imprint Lithography as the patterning method.

2.1 Step and flash imprint lithography

The results from the present study are applicable for cooling of electronic devices. Thus there was no better strategy than to choose a patterning method that is currently used in the electronics industry. Advances in microelectronics have resulted in decreasing feature sizes and increasing performance of electronic devices. Photolithography is one of the most vastly employed device-patterning techniques even to-date. The resolution of the pattern in such techniques is limited by the optics. As the feature sizes decreased the resulting need for higher resolution in the photolithography process required lower exposure wavelengths and higher numerical apertures of the lenses used in the photolithography process. The photolithography equipments progressively became more

sophisticated and the associated costs became prohibitive. As a result the need arose for alternate lithography techniques that had significantly lower costs (capital costs and operational costs). Nano Imprint Lithography (NIL) was invented as a solution to mitigate the increasing costs associated with photolithography. It simplified the lithography process by the use of silicon or silicon dioxide templates that contained the inverse replica of the pattern to be formed on the device in the place of photo-masks. Chou [25] and his group developed the thermal nano imprint lithography at Princeton. The process initially involved the coating of the substrate with a polymeric material like PolyMethyMethAcrylate (PMMA). The substrate is heated beyond the glass transition temperature of the resist and the template containing the inverse of the pattern is pressed onto the softened resist. The template is then withdrawn from the substrate once the resist had filled up its recesses. The pattern is then transferred to the device on the substrate through suitable etch steps. Patterns (or inverse replica of those on the template) with 25 nm resolution were successfully created. Offsets of the above process were developed, one example being the Step and Squish Imprint Lithography. This technique, making use of a bi-layer on the substrate as opposed to the single PMMA layer, allowed for greater etch selectivity after the pattern was pressed onto the resist. The first layer on the substrate was an organic crosslinkable transfer layer above which a silylated non-crosslinked imprint layer was coated. The transfer layer remains solid while the imprint layer is softened when heated above its glass transition temperature. The imprinting is done at elevated temperatures (140 °C) and pressures (600 to 1900 psi). This process was also successful in developing nano-scale features on the substrate.

The high pressures and temperatures used would not allow for effective use of this technique for patterning multi-layer devices since the thermal and mechanical stresses that the substrate is subjected to during the process hamper the alignment and overlay. Following these shortcomings, the SFIL technique was developed at the University of Texas at Austin [26].

The SFIL simplified the technique even more with the use of a low-viscosity, Ultra Violet (UV) curable, silicon-containing resist. It is also called the *"imprint resist"* or *"etch barrier"*. The substrate is first coated with an organic transfer layer. The SFIL process makes use of a quartz template that is transparent to the UV source. The template contains the inverse replica of the features to be patterned as in the NIL process. The template is fabricated by Electron Beam Lithography (EBL). After the transfer layer has been coated, a very small volume of the imprint resist is dispensed on the substrate. The template is brought within close proximity to the surface of the substrate. The low-viscosity imprint resist then fills up the recesses in the template by capillary action. Once the resist is given enough time to fill up the recesses, it is cured using the UV light through the template from the other side. The template is then released from the substrate leaving behind the required pattern on the imprint resist. Suitable etch steps then transfer the pattern to the substrate. The presence of silicon in the imprint resist gives good etch-selectivity while transferring the features to the transfer layer. This gives high aspect ratio features on the substrate. The SFIL process steps is shown in Fig. 1

Quartz Template

Anti-reflective
coating
(Transfer
layer)

Imprint resist

Silicon substrate

1. ORIENT TEMPLATE
OVER SUBSTRATE

2. DISPENSE IMPRINT
RESIST ON SUBSTRATE

UV cure

3. BRING TEMPLATE DOWN
WITHIN CLOSE PROXIMITY
OF THE SUBSTRATE

4. CURE RESIST WITH UV
LIGHT AFTER GIVING IT
SUFFICIENT TIME TO FILL UP
THE RECESSES IN THE
TEMPLATE

Residual layer

5. RELEASE TEMPLATE
FROM CURED RESIST

6. REMOVE RESIDUAL
LAYER THROUGH
"BREAKTHROUGH" ETCH

7. TRANSFER PATTERN TO
TRANSFER LAYER THROUGH
DRY ETCHING (RIE)

8. TRANSFER PATTERN TO
SILICON SUBSTRATE
THROUGH DRY ETCHING (RIE)

STEP AND FLASH IMPRINT LITHOGRAPHY – PROCESS STEPS

Fig. 1. Schematic diagram showing the process steps used in Step and Flash Imprint Lithography process (figure not to scale).

The key advantage of this process compared to the NIL techniques is that with the employment of a low-viscosity resist, it can be performed at room temperature and low pressures unlike the former. Also, the low viscosity of the imprint resist allows it to easily fill the recesses in the template irrespective of the nature of the pattern. In the case of more viscous resists like the one used in NIL (PMMA), it takes more effort for the resist to fill the recesses if the pattern consists of non-uniform pattern densities and sometimes results in bad imprints. The following sections will describe in greater detail the process steps used in SFIL for fabricating the required test surfaces.

2.1.1 Template fabrication

The template is the master that contains the inverse of the pattern that is to be transferred to the silicon substrate. Once the template has been fabricated with as few errors as possible, it can be used to create the same set of patterns on a number of substrates with routine cleaning and surface treatment. The template used starts off as quartz blank measuring 6 inch (15.2 cm) by 6 inch (15.2 cm) by 0.25 inches (0.635 cm). Four templates measuring 6.5 cm by 6.5 cm by 0.635 cm can be fabricated from one such blank. The center of each of these templates has a centrally positioned raised active region called the *"mesa"*. The mesa region contains the inverse of the pattern to be transferred to the substrate. The mesa can either be a 1 cm square or a 2.5 cm square. The present study uses a template with 1 cm square mesa. The mesa is raised to 15 μm height compared to the rest of the template. This is formed by etching the non-printable areas on the template using suitable wet Buffered Oxide Etch (BOE) technique. The

BOE solution used is typically 6 parts of 40 % NH₄F and 1 part of 49 % HF. The quartz blank with four potential templates is then diced, polished and beveled to obtain the individual templates. The template is then cleaned using Piranha solution (2:1 mixture of 96 % concentrated sulfuric acid to 30 % concentration of Hydrogen Peroxide). The mesa area is then coated with a 15 nm thick chromium layer. The pattern is then written on the template using electron beam lithography. The chromium coating serves to avoid charging during this process. The layer also serves as a mask for pattern transfer to quartz during the etching process. The high oxide to chromium selectivity in fluorocarbon based etches is taken advantage of for the pattern transfer into quartz.

Fig. 2 shows the process steps undertaken in the fabrication of the template. Prior to writing the pattern using Electron Beam Lithography (EBL), the blank is first spin-coated with a positive-tone electron beam resist ZEP520A (Zeon® Co.) to a thickness of approximately 400 nm or lower. A JEOL JBX6000FS/E EBL tool was used at the MRC (University of Texas at Austin) to write the pattern on the resist. The tool uses a modulated electron beam to write patterns with structures as small as 20 nm. Typically a layout editor such as L-Edit (Tanner EDA®, a division of Tanner Research®, Inc.) is used to create a layout of the pattern to be created on the computer. This file is then converted to a Graphic Design System (GDSII) file type. This is then loaded into the system which then converts it into JDF (Job file), SDF (Schedule file) and corresponding exposure set-up files to be read by the tool. The tool is then activated and the given pattern is exposed

on the resist (the help of Dr. Marylene Palard, MRC, University of Texas at Austin, in the fabrication of the template is gratefully acknowledged).

Smaller the feature size, greater is the time required for the template fabrication. Typical fabrication time for a single template was 20 hours; this required 12 hours for EBL as well as 2 to 8 hours for etching and chrome deposition. The template with the 1 cm square mesa was selected so that the entire mesa can be filled with the given structures at a faster rate compared to a 2.5 cm mesa template. The patterned resist is then developed by sitting in ZED-N50 developer (Zeon® Co.) for about 1 minute. The exposed regions of the positive tone e-beam resist get dissolved in the developer. The template is then rinsed thoroughly with Iso-Propyl-Alcohol (IPA).

Template is now ready for pattern transfer into the chromium layer. Dry chrome etch is a chlorine gas based etch. The RIE (Reactive Ion Etching) is done in the Trion® Oracle Plasma etcher's third chamber that is compatible with chlorine gas chemistry. The etching is performed in small time-steps with the template inspected between each step using an optical microscope. Prior to chrome etching, the exposed regions have a shiny color. Upon chrome etching, the regions not covered by the resist are removed by plasma etching. This process is complete when the shiny color of the exposed regions becomes dark in color.

15 μm raised platform on template called "Mesa"

Chromium coating

Quartz template

Chromium coated mesa on quartz template

E-beam

E-beam resist

Coat with E-beam resist. Pattern resist using E-beam lithography tool

Develop patterned resist using developer

Transfer pattern to chromium through dry etching (Reactive Ion Etching)

Transfer pattern to quartz mesa through dry etching (Reactive Ion Etching)

Fig. 2. Schematic diagram showing the process steps used for quartz template fabrication (figure not to scale).

Once the chrome etch is complete, the pattern is transferred into quartz using CF_4 based etch, again using the Trion® Oracle Plasma etcher. Since the pattern written in the present study was too intricate, the laser microscope was not powerful enough to evaluate the quartz etch. For this purpose a Digital Instruments® Atomic Force Microscope was used. The quartz etch is done to a target depth of 100 nm.

Once the pattern transfer to the quartz is complete, there may be some amount of chromium still sticking to the surface. The template is wet etched with Transene® solution until all the chromium is removed. Finally the process leaves behind a transparent template with the inverse replica of the desired pattern on its 1 cm square active area (or the mesa).

2.1.2 The pattern

The pattern created on the template is a square array of holes. These 100 nm deep holes had an average diameter of 200 nm, and pitches of 1 μm in the longitudinal direction and 0.9 μm in the transverse direction. Upon imprinting and etching into silicon using RIE, this pattern is used to create 200 nm diameter cylindrical *"nano-fins"* with a height of 100 nm and pitches of 1 μm in the longitudinal direction and 0.9 μm in the transverse direction. By substituting the RIE technique for pattern transfer into silicon with Deep Reactive Ion Etching (DRIE), fin-heights greater than 100 nm can be achieved. The process along with the different materials used and their functions are explained in greater detail below.

2.1.3 The imprinting process

Imprinting is done on 4 inch double-side-polished silicon wafers. It is done using IMPRIO 100 (Molecular Imprints® Inc.) imprinting tool at the Microelectronics Research Center (University of Texas at Austin). The IMPRIO 100 is essentially a high precision semi-automatic mechanical tool that allows for monitoring and performing the imprinting process.

2.1.3.1 Piranha clean

The wafers are first cleaned to ensure that small particles and residual organic matter are removed from the surface. For this, a piranha clean is done in an acid hood. The wafers are loaded on a wafer holder and set aside. The piranha solution is prepared by slowly adding 1 part of hydrogen peroxide to 2 parts of sulfuric acid. Typically 1650 ml sulfuric acid is taken in a quartz container. 825 ml hydrogen peroxide is then slowly added to the sulfuric acid. Care is taken to ensure that the sulfuric acid is not added to the hydrogen peroxide as this may lead to a violent reaction. The measurement is done using graduated beakers. The normal reaction is exothermic and the solution starts to bubble. The mixture is allowed to sit for 5 minutes to stabilize after which the wafer holder is lowered into the solution. The mixture is a strong oxidizer and it effectively removes organic residues from the substrates. The solution is allowed to react on the substrates for 8 to10 minutes. The substrates are then taken out from the solution and rinsed with de-ionized (DI) water in the cascade rinser that is part of the hood. Here two 5-rinse cycles are completed. Once this is done, the substrates are loaded into a Verteq®

Spin/Rinse Dryer (Akrion, Inc.) for drying. The clean silicon substrates are then carefully loaded in a wafer box that has been wiped clean with a clean-room wipe sprayed with Iso-propyl alcohol (IPA). The silicon wafers are now ready to be coated with the transfer layer. The advantage with this process is that the substrates that did not experience a good imprinting session can be reclaimed using the above process before re-use. The template is also cleaned in a similar fashion before the imprinting process with the exception that it is left in the piranha solution for about 15 minutes before rinsing with DI water in the cascade rinser. Nitrogen gas provided in the same acid hood is used for drying the template after rinsing with iso-propyl alcohol. Sometimes the template may have tough residue sticking to its surface, which is not effectively removed by normal piranha clean. For this the piranha bath is placed on a hot plate, which is heated to about 120 °C. The heated solution then gives the template a better cleaning effect compared to the normal piranha clean. Care is taken to ensure that partially heated DI water is first poured on the template after a heated piranha clean since it may undergo thermal shock if it comes directly in contact with relatively cold DI water from the supply line during the rinsing step.

2.1.3.2 Transfer layer coating

SFIL process uses a bi-layer scheme as explained above. The first layer is called the "transfer layer". Transfer layers are coated on the substrate to get high aspect ratio features on the substrate. The functions of the transfer layer are

   a. To promote adhesion of the imprint resist to the substrate after UV curing.

b. To improve the feature aspect-ratio.

c. To allow for easy flow of imprint resist to the recesses in the template through capillary action.

The selection of the material to be used for the transfer layer is done based on the requirements above. In addition, it should not dissolve or swell when the low-viscosity imprint resist is dispensed on the substrate during imprinting. The incorporation of silicon in the etch barrier gives a good selectivity between the etch barrier and the transfer layer during pattern transfer into the transfer layer. Anti Reflective Coatings (ARCs) such as DUV30J (Brewer Science®) is found to have all the important requirements of a transfer layer and is thus used in the present study. The advantage with these ARCs is that they can be easily spin coated on the substrate. After coating, the layer is soft-baked at 180 °C for 1 minute. A little less than 1 ml of DUV30J is dispensed on the silicon substrate. Care is taken to avoid air bubbles while dispensing. The three-step recipe followed for spinning the transfer layer on the substrate is as follows:

a. 1000 rpm with a ramp of 5000 revolutions/second for 5 seconds

b. 2500 rpm with a ramp of 1500 revolutions/second for 25 seconds

c. 3000 rpm with a ramp of 1000 revolutions/second for 5 seconds.

The above recipe yields a transfer layer coating of approximately 65 nm thick. Once the soft-bake is complete, the silicon substrates are ready for imprinting.

2.1.3.3 Imprinting

The clean template and silicon substrates are taken for imprinting using the IMPRIO100. The first step is to ensure that the helium supply is switched on. Helium gas helps in purging the area to be imprinted. The template is rinsed with IPA and dried with nitrogen gas in a material compatible hood. A release layer called Relmat™ (Molecular Imprints$^{®}$) is provided in liquid form. A drop of the highly volatile liquid is dispensed on the mesa. The template is then tilted in all directions so that the release agent reaches all its corners. Care is taken to ensure that the Relmat does not cross the borders of the mesa during this process. As the Relmat evaporates, the final drop is blown away from the mesa with nitrogen gas. This ensures that no particle residues are left on the mesa once the liquid has completely evaporated. The alignment of the template is done by focusing on one horizontal edge of the mesa and making adjustments to the alignment screws until the required accuracy is achieved. Aligning the template ensures that the sides of imprinted squares are parallel to the flat of the silicon wafer. The template is now loaded in the IMPRIO100 imprinting tool's vacuum chuck. Next, template leveling is performed. Leveling ensures that the template's mesa is held perfectly parallel to the substrate below which results in more uniform imprints. For this a particular measurement strategy is chosen. Since the mesa is 1 cm by 1 cm, a 4-point strategy is initially chosen. Under this strategy, the level of the template is measured at four different locations. After each measurement, manual adjustments are made to the leveling screws. The level is then re-measured and the process is repeated until the desired accuracy is achieved. If greater accuracy is desired, a 12 point or 16 point

measurement strategy can be employed after a relatively rough alignment using the 4 point strategy is obtained.

The next stage in the imprinting process is to load the substrate. IMPRIO100 is equipped with an automatic substrate loading system unlike the manual template loading system. The substrate coated with transfer layer is loaded in the tool. The alignment and leveling of the substrate relative to the positioned template is performed automatically. Care is taken to ensure that the template alignment is not altered afterward. If the template alignment is changed, the substrate has to be re-leveled with respect to the template's new leveling. The imprinting process is controlled by the user through a computer and Graphic User Interface provided by Molecular Imprints[®], Inc.

A number of parameters have to be selected before the first imprint. The etch barrier or imprint resist is dispensed on the substrate in the form of a droplet pattern. The template is then brought within close proximity of the substrate. The etch barrier fills the recesses in the template, is UV cured and the template is released to leave behind a 1 cm by 1 cm square imprinted area. The imprint is visually inspected and changes to input parameters are made if necessary. The process is then repeated at another position on the substrate. It is from this "stepping" scheme that the substrate is covered with imprints and the SFIL process derives its name.

The imprint resist droplet pattern is defined in the droplet recipe that is saved in the system. The recipe is provided with the total drop volume, number of drops, pattern of the drops and the droplet offset in the x and y directions. The size of the template mesa (1 cm by 1 cm), is also entered into the system. The pattern on the mesa is written in such a way that the nano-fins are contained in a 0.8 cm by 0.8 cm square centrally placed in the 1 cm by 1 cm mesa. Other parameters in the recipe include the gap between each imprint (or the "street size") and the stepping size (summation of the mesa size and the street size). Once this information is entered, the system generates a schematic of a four-inch silicon wafer model showing the square imprint positions on it. Depending on the surface coverage required imprinting could be done all over the substrate or only over the required areas. The UV cure step is also defined in the system by the user with the pre-exposure time, exposure time and the post exposure time. Pre-exposure time is given to allow the resist to fill all the recesses in the template. This again depends on the intricacy of pattern. For the present study a pre-exposure time of 110 seconds was used. Exposure time typically used was 10 seconds with no post-exposure. Droplet volumes as low as 0.05 μl are used for each imprint. These parameters are also sometimes adjusted depending on the visual inspection of the resulting imprint. The imprinting process is monitored on the computer. Template release forces of the order of 5-7 N can be expected to give good imprints.

For a given template and substrate, the imprinting parameters have to be optimized by trial and error until the optimum setting of the different parameters is achieved. Upon

UV cure, a good imprint should be a uniform light-blue film without fringes. Excess volume either all over the imprint or over parts of the imprint can cause fringes. By constant adjustment, the quality of the imprints can be improved. In addition, imprint parameters keep changing depending on the conditions of each imprinting session. Thus, the parameters that yielded good imprints in the previous session may have to be slightly modified to good imprints in the current session. Particles on the substrate may affect the imprinting process. Before choosing a particular area for imprinting, it is visually inspected for particles both large and small. Small particles may destroy an imprint and may get stuck to the mesa potentially spoiling future imprints. Large particles may destroy the template leveling itself. Thus, areas in which particles are clearly seen should be avoided for imprinting. Once the imprinting is complete on one substrate, it is unloaded and another substrate is loaded. If clean, the template can be used for imprinting more than one silicon substrate. If the Relmat™ (Molecular Imprints, Inc.) release agent wears away over a number of imprints, the resist may get stuck to the mesa and solidify upon UV curing. At this point, the template may have to be unloaded and cleaned. Depending on the condition of the template, it can either be spray-cleaned with IPA and treated with a new layer of release agent after drying with Nitrogen gas or it may have to be re-claimed using piranha clean (explained above) followed by the release layer treatment.

2.1.3.4 Pattern transfer

Once the imprinting is complete, the pattern on the substrate is transferred to the silicon to form the silicon nano-fins through Reactive Ion Etching (RIE). Since the template is only brought in close proximity to the substrate and not made to touch it, a thin residual layer of the etch barrier is present on the substrate. For transfer of pattern to the transfer layer, the residual layer is first removed. This step is called the *"breakthrough etch"*. Before etching, the thickness of the transfer layer and the residual layer is measured using NanoSpec/AFT film analysis system (Nanometrics® Inc.). Once the measurement is done, a Plasma-Therm® RIE system is used to perform the breakthrough etch. Before this, the chamber is wiped clean with IPA and then cleaned using oxygen plasma for around 15 minutes. The breakthrough etch is done using CHF_3 and O_2 gas-based etch. The etching is done is small steps. After each etch step, the film thickness is measured using NanoSpec/AFT and the process is repeated until the residual layer is removed. Once the residual layer is removed, the transfer layer is etched using an O_2 gas-based etch. Here too, the etching is done in small steps until the pattern transfer is complete. Finally Cl_2 and HBr based etch transfers the pattern into silicon. Since the transfer layer and the etch barrier films are now removed, the etching cannot be monitored using the NanoSpec/AFT film analyzer. In addition, the nano-fins are also too small to be observed under a lazer microscope. Thus a Digital Instruments® Atomic Force Microscope is used to analyze the silicon surface. Once the pattern transfer to silicon is complete, the substrate contains the array of silicon nano-fins.

2.1.4 Test surfaces

A total of three enhanced test surfaces were fabricated using the procedure described above. The first test surface was fabricated using the RIE process. Fig. 3 shows an Atomic Force Microscope (AFM) scan using which the diameter of the nano-fin was measured. The average diameter was found to be 200 nm. Fig. 4 shows a similar AFM scan used to measure the height of the nano-fins. The average height was found to be 100 nm. Finally the array has a pitch of 1 μm in the longitudinal direction and 0.9 μm in the transverse direction. Since the nano-fins were approximately 100 nm tall, this surface is denoted as *"100 nm"* after the height of the fins.
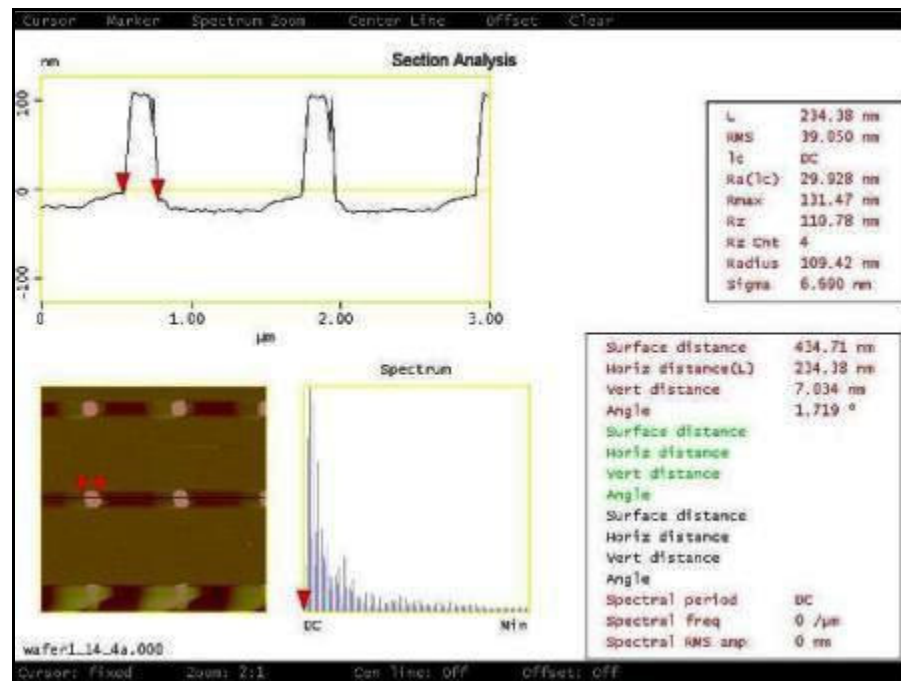
Fig. 3. *"100 nm"* test surface: An Atomic Force Microscope scan showing the measured diameter of the nano-fins on the *"100 nm"* test surface fabricated using Step and Flash Imprint Lithography. The average diameter of the nano-fins was found to be 200 nm. The pitches were found to be 1 μm in the longitudinal direction and 0.9 μm in the transverse direction.
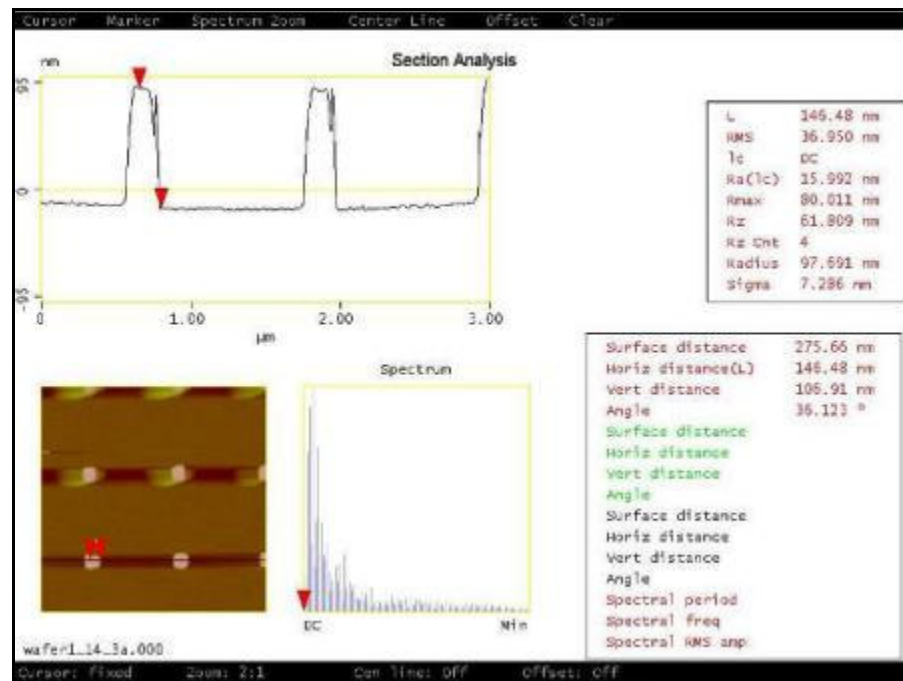
Fig. 4. *"100 nm"* **test surface: An Atomic Force Microscope scan showing the measured height of the nano-fins on the** *"100 nm"* **test surface fabricated using Step and Flash Imprint Lithography. The average height of the nano-fins was found to be 100 nm. The pitches were found to be 1 μm in the longitudinal direction and 0.9 μm in the transverse direction.**

The remaining two surfaces were fabricated using DRIE (Deep Reactive Ion Etching) in place of RIE (Reactive Ion Etching). The imprinting was performed in the same fashion as the first test surface. The imprinted substrates were sent to University of California at Irvine for the DRIE process. Two surfaces were fabricated by etching to different depths. The first test surface had fins in the shape of frustums of cones with a larger diameter of 100 nm, smaller diameter of 65 nm and a height of 336 nm. The DRIE process thus reduced the diameter of the fins from the original 200 nm fins on the etch barrier to the values above. This test surface is denoted as *"336 nm"* after its height. The distance between the centers of the fins in both the longitudinal and transverse directions remains the same as for the first test surface (1 μm and 0.9 μm respectively).
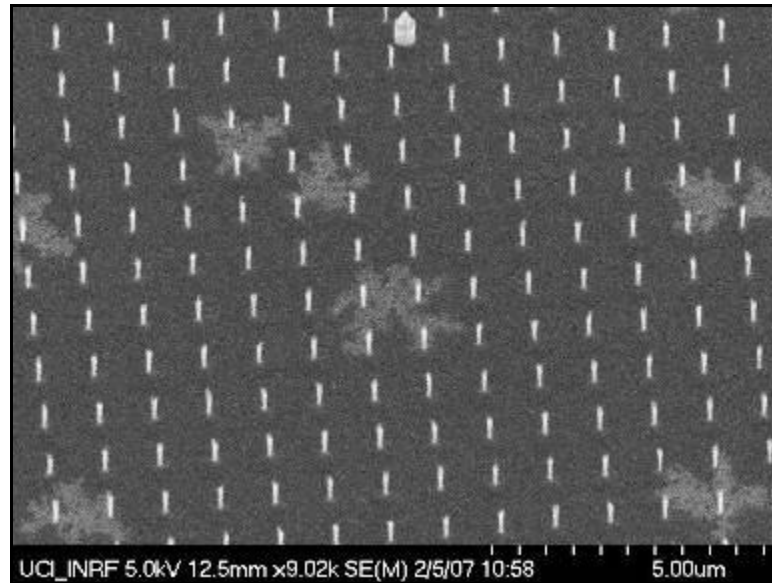
Fig. 5. *"336 nm"* **test surface: A Scanning Electron Microscope image showing the array of the nano-fins on the** *"336 nm"* **test surface fabricated using Step and Flash Imprint Lithography. The average height of the nano-fins was found to be 336 nm. The fins are in the form of frustums of cones with average larger and smaller diameters of 100 nm and 65 nm respectively. The pitches were found to be 1 μm in the longitudinal direction and 0.9 μm in the transverse direction.**
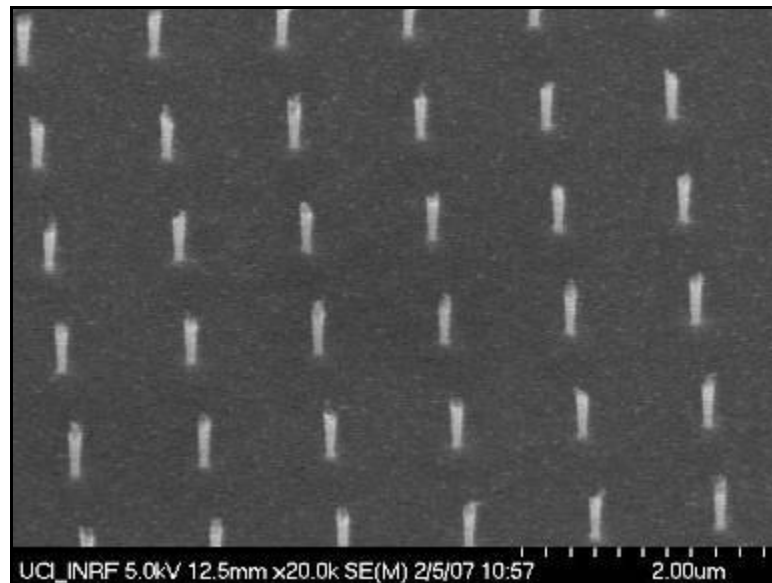
Fig. 6. *"336 nm"* **test surface: A magnified Scanning Electron Microscope image showing the array of the nano-fins on the** *"336 nm"* **test surface fabricated using Step and Flash Imprint Lithography.**

Fig. 5 and Fig. 6 show Scanning Electron Microscope (SEM) images of the array of nano-fins on the *"336 nm"* test surface at two different levels of magnification.

The second test surface fabricated through DRIE had well-defined cylindrical fins with a diameter of 186 nm and a height of 259 nm. Here again, it is observed that the diameter of the fins was reduced from the original 200 nm on the etch barrier. This test surface is denoted as *"259 nm"* after its height. The distance between the centers of the fins in both the longitudinal and transverse directions is the same as for the first test surface (1 μm and 0.9 μm respectively).
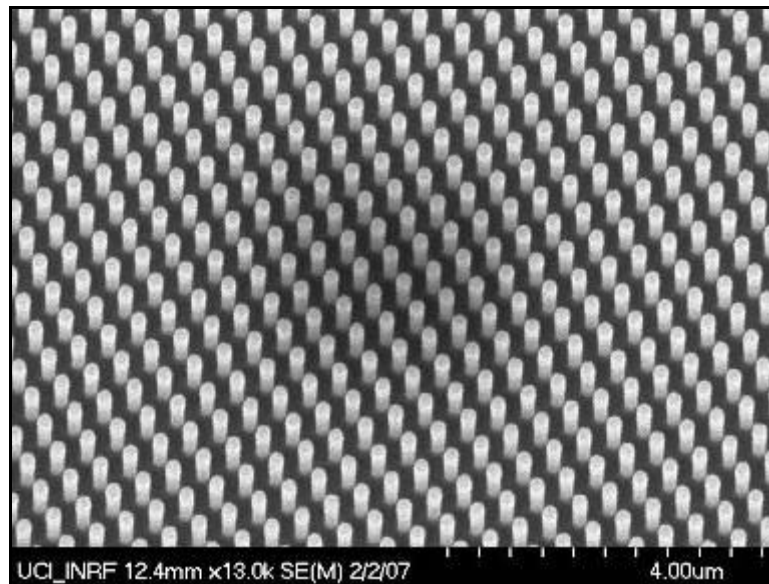
Fig. 7. *"259 nm"* test surface: A Scanning Electron Microscope image showing the array of the nano-fins on the *"259 nm"* test surface fabricated using Step and Flash Imprint Lithography. The average height of the nano-fins was found to be 259 nm. The fins are in the form of cylinders with average diameters of 189 nm. The pitches were found to be 1 μm in the longitudinal direction and 0.9 μm in the transverse direction.
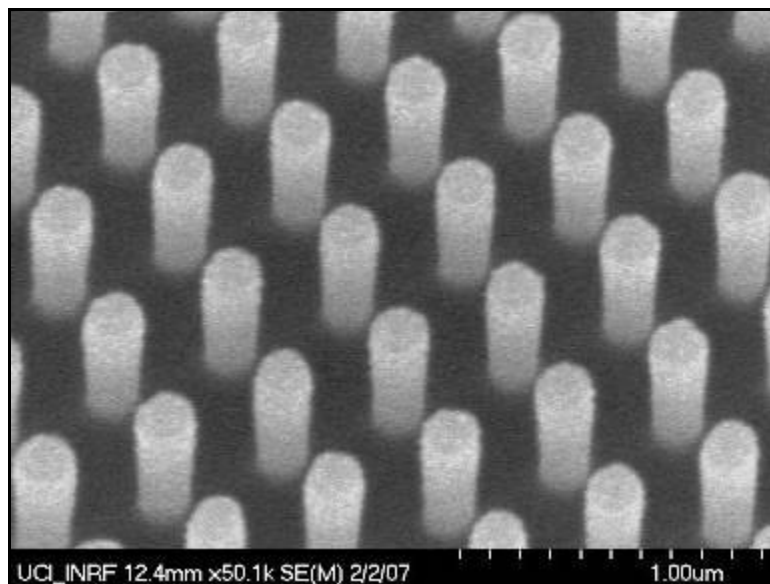
Fig. 8. *"259 nm"* **test surface: A magnified Scanning Electron Microscope image showing the array of the nano-fins on the** *"259 nm"* **test surface fabricated using Step and Flash Imprint Lithography.**

Fig. 7 and Fig. 8 show two SEM images of the array of cylindrical nano-fins on the *"259 nm"* test surface at two different levels of magnification. The "*100 nm*" test surface had a good coverage of imprints all over its surface. As explained earlier, a gap or "street" of 0.015 cm is present in-between the 1 cm by 1 cm imprints. In addition, because of the nature of the pattern, the nano-fins are contained only in a 0.8 cm by 0.8 cm square within the imprint. Thus the test surface area is not completely covered by the nano-fins subsequent to the SFIL process. The *"336 nm"* and *"259 nm"* test surfaces on the other hand had an issue with particles during the imprinting process. The presence of particles on the substrate precluded the use of certain areas on the substrate for imprinting. Thus, in addition to the lack of complete coverage as explained above for the *"100 nm"* test surface, further coverage was restricted because of particles.

3. EXPERIMENTAL SET-UP AND PROCEDURE

In this study, the pool boiling set-up used to perform the experiments was fabricated and assembled previously by Dr. Hee Seok Ahn, former graduate student, Mechanical Engineering, Texas A&M University. His assistance in this regard is gratefully acknowledged. The rationale behind the design of the pool boiling setup was to provide a simple, yet functional set-up that would assist in the visual observation and automated recording of the parameters. The boiling heat transfer experimental set-up consists primarily of the following parts:

1. A leak-proof cubical viewing test chamber that houses the heater apparatus in a pool of liquid.

2. A refrigerating/heating circulation unit that aids in maintaining the pool of test fluid at a constant temperature.

3. Power supply units for providing electrical power to heat the cartridge heaters and the tubular heater submerged in the liquid pool.

4. A data acquisition system for automated recording and processing the experimental data obtained from the thermocouples used in the experimental set-up.

Fig. 9 shows the schematic diagram of the experimental boiling set-up along with its different components. Each of those components is explained in detail below.
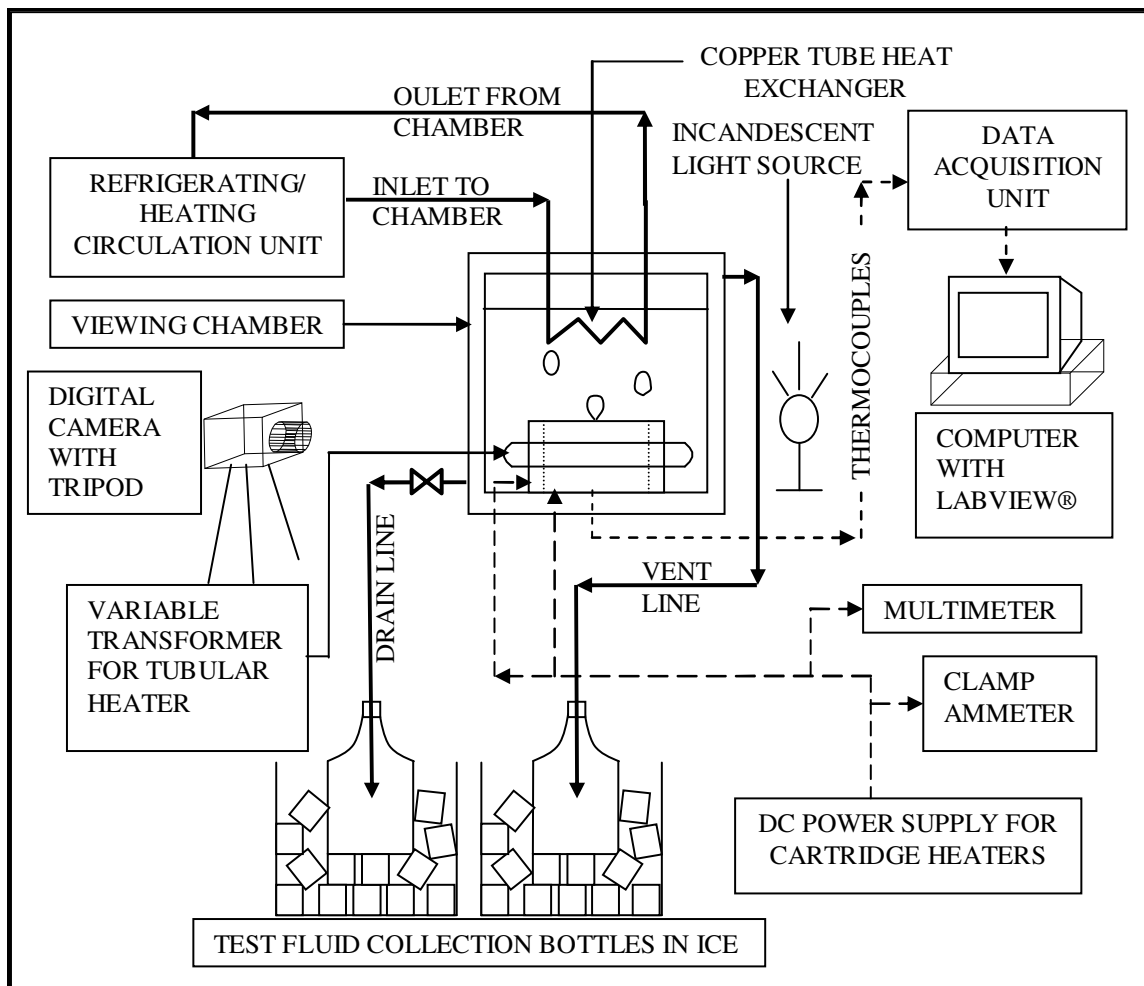
Fig. 9. Schematic diagram of the test set-up (figure not to scale).

3.1 The test chamber

The cubical test chamber was made by welding twelve L-shaped steel beams together. These beams are 0.125 inch (0.3175 cm) thick, have 1-inch (2.54 cm) long legs and form the cubical skeletal structure with a side of 5.9 inches (14.986 cm). In addition two steel plates, 0.25 inch (0.635 cm) thick, were welded to one side face and to the bottom of the structure. A hole is provided at the center of the bottom plate for the power supply wires to be inserted in the copper block and also for the thermocouple lead wires from the

copper block to be connected to the data acquisition system. The steel plate covering the side face is provided with holes for the tubular heater and its connections. In addition to these, two holes approximately 0.5 inches (1.27 cm) in diameter are provided for venting the test chamber (1.125 inches or 2.8575 cm from the top) and for draining the test fluid from the chamber (0.125 inches or 0.3175 cm from the bottom). The vent line ensures that the chamber is maintained at atmospheric pressure while running experiments. The vapor in the vent line is collected in a glass container buried in ice. The vent line also helps in condensation and collection of test fluid vapor during the degassing step that will be explained in later sections. The drain line allows the test fluid to be drained and collected in another glass container upon completion of each experimental run thus making the test fluid is reusable. The top of the cube is made from a detachable, 0.25 inch (0.635 cm) thick steel plate which is provided with four holes. Two holes are used for the entry and return of the cooling coil from and to the constant temperature bath. This coil is used to maintain a constant temperature of the pool of liquid within the chamber. One of the other holes is used for the temperature sensor from the chilling unit and the final hole is provided for pouring the test fluid into the chamber. The remaining three open sides of the cube are enclosed with 0.125 inch (0.3175 cm) thick Pyrex glass plates that are held between 0.125 inch (0.3175 cm) thick silicon gaskets. The Pyrex plates along with the silicone gaskets are assembled and clamped by plates using 16 screws. The steel clamping plates and the silicon gaskets are cut at the center in such a way that they allow a 4.5 inch by 4.5 inch (11.43 cm square) viewing areas through the Pyrex glass windows that are mounted on three sides. This procedure is used to assemble

the leak-proof cubical test chamber. Fig. 10 shows a three-dimensional rendering of the cubical test chamber along with its major components.
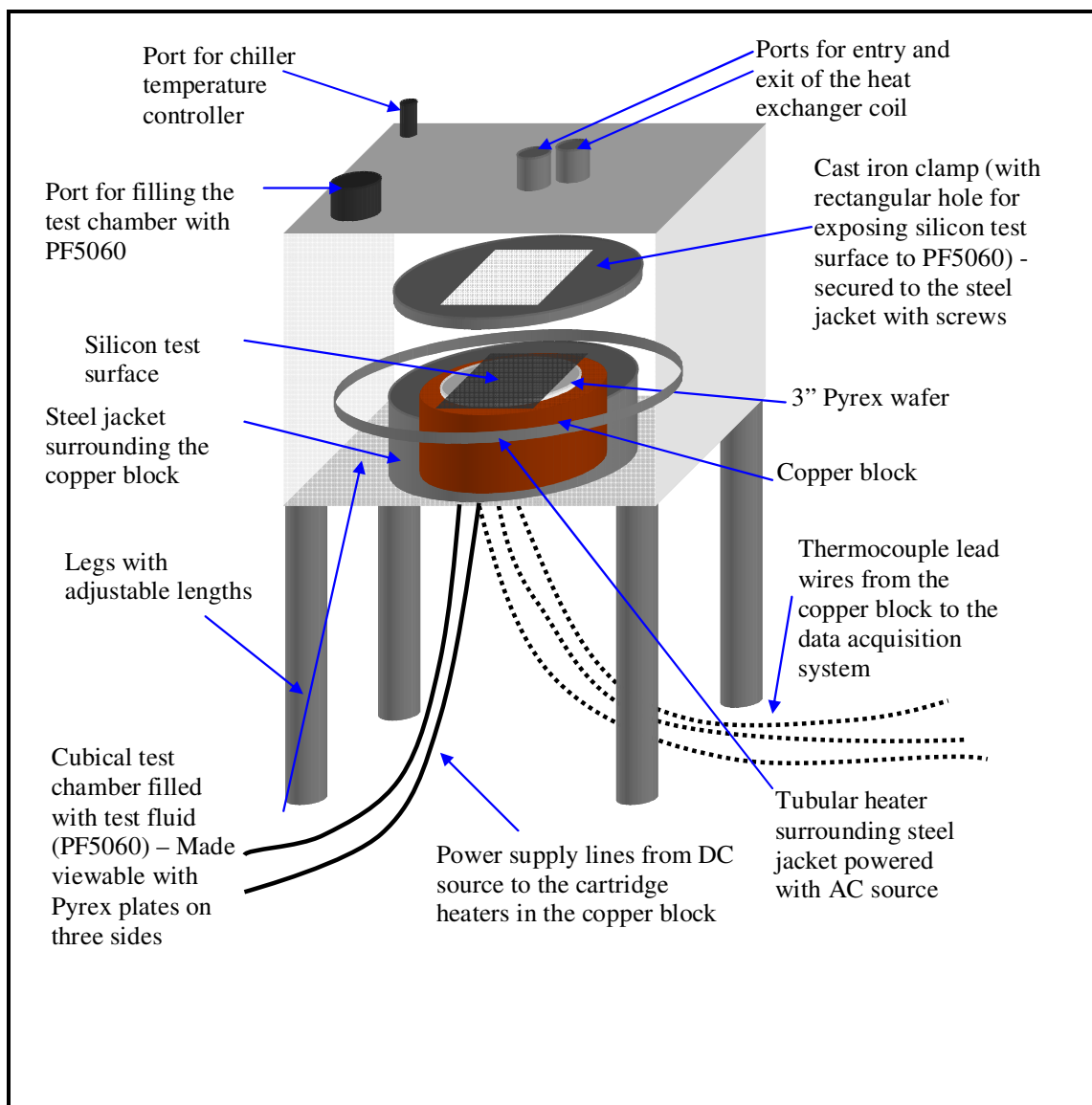
Fig. 10. The cubical test chamber set-up (figure not to scale).

3.1.1 Test surface assembly

Fig. 11 shows the placement of the test surfaces on the heater apparatus prior to the start of pool boiling experiments. The cubical test chamber houses the heater apparatus. The heater apparatus consists of a cylindrical copper block surrounded by a steel jacket. A Pyrex wafer is placed between the test surface and the copper block. The test surface is then mounted using a steel clamp.
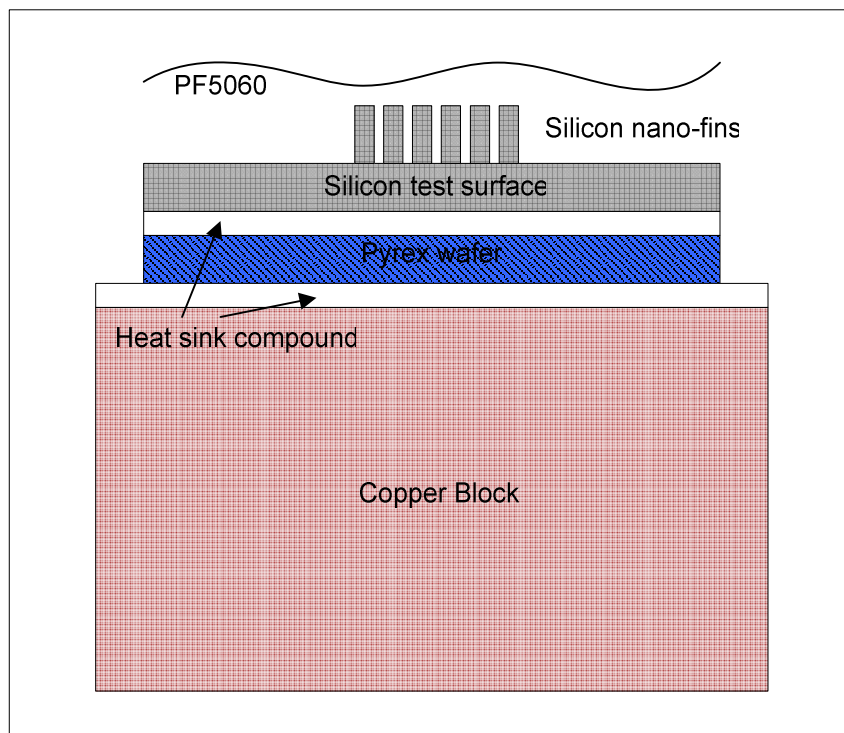
Fig. 11. Schematic diagram showing the placement of the test surface on the heater apparatus (figure not to scale).

Fig. 12 shows the schematic of the cylindrical copper block used in the heater apparatus.
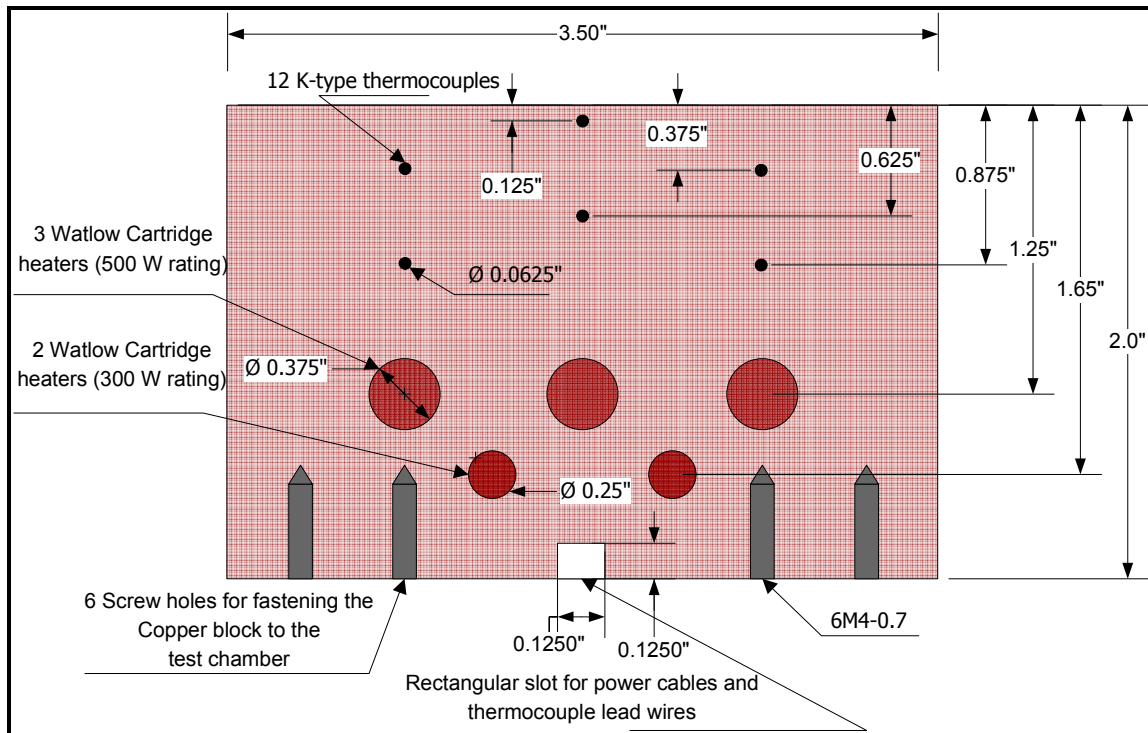
Fig. 12. Schematic diagram of the copper block (figure not to scale).

It is 3.5 inches (8.89 cm) in diameter and 2 inches (5.08 cm) in height. A steel jacket of 3.9 inches (9.9060 cm) inside diameter and 0.3 inch (0.762 cm) thickness is provided around the copper block. Horizontal holes are drilled in the copper block for embedding cartridge heaters. Two types of cartridge heaters (500 W rating and 300 W rating) are inserted horizontally in the copper block, parallel to the flat surfaces and in parallel to each other. Three 500 W rating cartridge heaters are inserted 0.75 inches (1.9050 cm) from the bottom and two 300 W rating cartridge heaters are inserted 0.35 inches (0.889 cm) from the bottom. The heat produced by these heaters and transferred eventually to the test surface above is measured through the temperature at different locations in the copper block using twelve, sheathed and calibrated thermocouples. They are inserted

into the solid copper block at four different depths of 0.125 (0.3175 cm), 0.375 (0.9525 cm), 0.625 (1.5875 cm) and 0.875 (2.2225 cm) inches from the top and at three different radial locations at each depth. A groove is provided at the bottom of the copper block so that these thermocouples and the power cords to the cartridge heaters can be directed out of the cubical chamber through the central hole on the bottom steel plate of the test chamber.

The copper block and the steel jacket are tightly secured to the bottom steel plate of the test chamber by means of six screws each. The test surface is held in place on top of the copper block using a steel clamp that is screwed to the top of the steel jacket using 6 screws. The steel clamp has an opening at the center to expose the test surface to the liquid pool. The exposed area is a 2.3125 inch (5.8738 cm) by 1.25 inch (3.175 cm) rectangle with rounded corners, each with a radius of 0.25 inches (0.635 cm). A Teflon gasket is provided between the steel clamp and the test surface. To make up for the height difference between the copper block with test surface arrangement and the steel jacket, silicone gaskets are provided between the steel clamp and the steel jacket and also between the steel jacket and the bottom steel plate of the test chamber. The overall arrangement provides a leak proof seal while at the same time exposing the test surface to the pool of liquid above.

In addition to this, an air gap is formed between the steel jacket and the copper block. Due to the poor thermal properties of air, it provides good insulation and helps ensure

that a larger proportion of the heat formed in the copper block is transferred to the test surface above ensuring 1-D heat conduction in the vertical direction. A highly conducting grease (Dow Corning®, 340 Heat Sink Compound) is applied between the copper block and the Pyrex wafer and also between the Pyrex wafer and the silicon test surface so that air gaps are avoided and thermal contact resistance is decreased. A tubular heater is provided around the steel jacket. The tubular heater is used for heating of the test fluid during the degassing step (that will be explained shortly) and can also be used for heating the pool of test fluid to saturation temperature during saturation condition experiments.

3.2 The refrigerating/heating circulation unit and cooling coil

In sub-cooling experiments, the test fluid (PF5060) is maintained at a fixed bulk temperature below its saturation temperature. To facilitate this, a refrigerating/heating circulation unit along with a cooling coil is used. The Polyscience® unit (Model 9612) consists of a 28 liter reservoir for the coolant fluid, a 5 speed duplex pump and a programmable RS232 interface which combine to provide temperature control from -25°C to +150°C. This very easily allows for a range of experiment types from saturation to highly sub-cooing types since the saturation temperature of PF5060 is 56°C. The present study will focus on pool boiling experiments for saturation, 10°C sub-cooling and 20°C sub-cooling conditions. The working fluid is a mixture of 10% ethylene glycol and water.

While the circulating unit is in use, the coolant is continuously pumped through a copper heat exchanger coil which is immersed in the pool of test fluid. The coolant fluid is maintained at a constant temperature and is used to cool the test fluid in the pool boiling experiment. The temperature of the test fluid (PF5060) is monitored by 3 calibrated K-type thermocouples positioned at different locations in the pool. The working fluid is then pumped back through the circulating unit to provide constant cooling of the test fluid. The cooling coil is made from 0.25 inch (0.635 cm) diameter copper tubes which are coiled to form a helix using a tube bender.

3.3 The power supply units

A variable transformer (Manufacturer: Staco Energy Products Co., Model: 3PN2210B, Series: 2200, Input: 120 Volts AC, Frequency: 50-60 Hz, Output: 0-140 volts) is connected to the tubular heater around the steel jacket. The tubular heater is usually activated during the degassing of the test fluid prior to the start of each experimental run and also can be used to maintain the saturation temperature (56°C) of the test fluid (PF5060) during the saturation runs. As explained above, the refrigerating/heating circulation unit allows for precise temperature control from -25°C to +150°C and thus can also easily be used for maintaining the required saturation conditions during those runs.

The power supply to the cartridge heaters in the copper block is provided by a Programmable DC Switch Mode Power Supply (Manufacturer: American Reliance, Inc.,

Model: SPS 120-10, Input: 120 volts AC, Frequency: 50-60 Hz, Maximum output voltage: 120 volts DC, Maximum output current: 10 amperes DC, Maximum output power: 1200 Watts).

3.4 The data acquisition system

The thermocouples inserted in the copper block transmit the data to a National Instruments® SCXI – 1000 Chassis with a SCXI – 1303 terminal block, analog MUX (32-channel thermocouple amplifier module) along with a PCI-6251 DAQ board. This setup is connected to a computer equipped with a Pentium – 4, 3.2 GHz processor. The real-time temperature monitoring and recording is done using LABVIEW® 7.1 software. The thermocouples are suitably labeled and connected to the corresponding ports in the National Instruments® data acquisition unit so that each temperature read-out is correlated to the correct thermocouple and its relative position in the copper block.

Using the thermocouple calibration data, the signals from the thermocouples are recorded, processed and conditioned by the LABVIEW® software. The thermocouples lead wires from the copper block are covered with aluminum foils and are placed on a rubber mat over the metal table to ensure that signal noise as well as electro magnetic interference (EMI) from the electric supply in the room is minimized. At each steady state, a two-minute temperature data is recorded at a frequency of 200 Hz. Each thermocouple read-out is then averaged over the period, which is later used to calculate the heat flux across the copper block.

At each steady state condition, five sets of voltage readings are recorded to measure the supply to the 500W cartridge heaters and the 300W cartridge heaters. This is facilitated by an Omega® True RMS Multimeter (Model: HHM 14; 0 – 1000 V DC, ±0.05%). The corresponding current readings are recorded using a TENMA® AC/DC True RMS digital clamp ammeter (Model: 72-6185, DC current: 40A, 400A).

3.5 Experimental procedure

The experimental procedure consists of the following steps.

3.5.1 Test surface assembly

First, the flat surface of the copper block is cleaned with Isopropyl alcohol. Similarly the 3 inch Pyrex wafer that is placed between the copper block and the test surface is cleaned as well. An optimum amount of the highly conducting grease (Dow Corning®, 340 Heat Sink Compound) is applied on the flat surface of the copper block as well as on either surface of the Pyrex wafer. This is done to ensure that no air pockets are trapped between the various surfaces and at the same time provides a conducting medium between them to ensure that the interfacial resistance is reduced. The heat sink compound has a thermal conductivity of 0.55 W/mK as opposed to that of air – 0.024 W/mK at room temperature. The cleaned test surface is then placed on top of the Pyrex wafer. A Teflon gasket is cut and glued to the underside of the steel clamp using silicone glue. The glue takes 45 minutes to cure. The Teflon gasket is provided to prevent direct contact between the clamp and the test surface and thus prevent damage to the test

surface. The steel clamp along with the Teflon gasket and opening at the center to expose the test surface is carefully placed on the test surface. It is then fastened to the steel jacket using 6 screws. A silicone gasket is placed between the steel clamp and the steel jacket to ensure a leak-proof seal. Initially, the 6 screws are tightened by hand. Now, the test chamber is now ready to be tested for leak.

3.5.2 The leak test

At the beginning of each experiment the test chamber is checked for any potential leaks. The test surface assembly on the copper block is also checked for any leaks. There are two major points at which leakage may occur through the test chamber following the test surface assembly described above. There may be leakage between the Teflon gasket under the steel clamp and the test surface. There may also be leakage near the silicone gasket between the steel clamp and the steel jacket. Typically, if too much heat sink compound is applied between the different layers of the test surface assembly, the test surface sits higher and causes a gap to be formed between the clamp and the jacket. On the other hand, if too little is applied, it causes a gap to be formed between the Teflon and the test surface. Thus, preventing gaps ultimately boils down to the optimum usage of the heat sink compound. Once the test surface has been assembled along with the other parts on the copper block, a leak test has to be performed to ensure that all leakage is prevented through the set-up. The test fluid used (PF5060) is highly wetting and has the potential to leak through very small gaps. This leakage is eliminated since PF5060 is a relatively expensive fluid. The leak test is done using distilled water. Also, during the

leak test, if any leak is present in the set-up, it is more easily detected using water since PF5060 is highly volatile and very quickly evaporates making it difficult to detect outside of the test chamber.

Water is first filled up to the top of the steel jacket and held there for a couple of minutes. This is used to test if there is a large leak between the steel clamp and the steel jacket. If no leak is detected, water is then filled up to the brim of the chamber. If any leak is present, it could still be from either of the above-mentioned points and is suitably corrected by tightening the screws on the steel clamp. This is because, in some cases, leakages near the silicone gasket or the top of the test surface will start only after a certain volume of water is added, where the weight of the water column may force it through small gaps. While tightening the screws, a torque wrench is used to ensure that equal torque is applied to all the screws. The test surface, being a thin silicon wafer, tends to be easily breakable and applying equal torque to all screws ensures that it is not subjected to differential stresses. During the experimental run too, the test surface is subjected to thermal stresses. Thus, care is taken to ensure that the applied torque is kept to a minimum. A lot of practice is required to master the preparation of the leak-proof test apparatus. Usually the leak test is performed first on an extra bare test surface to get an idea of the torque values to be applied before loading the actual test surface so that in case of breakage, a valuable test surface is not lost. In addition, the maximum torque that the test surfaces can withstand could be found by tightening the sample test surface until it breaks. That way, a factor of safety can be incorporated while applying torque for the

actual test surface. Once the chamber has been checked for leakage, water is allowed to stand up to the brim for approximately 30 minutes to ensure that absolutely no leakage is present. The water is then drained and the parts allowed to completely dry for approximately 12 hours before the start of the experiment.

3.5.3 The degassing step

Before the start of the actual experiment, degassing of the test fluid is performed. This is performed to remove any trapped gasses in it, which may cause premature nucleation. For this, the top steel cover along with the cooling coil is first lowered and secured to the top of the chamber. The drain line and the vapor line from the chamber are connected to glass containers. The valve on the drain line is closed and the vent line container is placed in an ice bath. The ice allows the test fluid vapors from the degassing step to be condensed and captured in the glass container. The test fluid is then poured into the chamber through the hole provided in the top steel cover plate until the cooling coil is sufficiently immersed in the pool. The hole is then sealed. The tubular heater is activated using the variable transformer while the circulating unit is switched on as well. The two are set in such a way that the pool of test fluid is maintained at a few degrees above its boiling point of 56° C for about 20 minutes. This ensures that all the trapped gases are released and condensed in the bottle below. The variable transformer is then switched off.

3.5.4 Data acquisition

Depending the type of experiment (saturation, 10 degree sub-cooling or 20 degree sub-cooling), the circulating unit is adjusted to maintain the bulk fluid at a particular temperature. The power is supplied to the cartridge heaters using the DC power supply unit described above. Every time a change is made to the power level, the system takes time to reach steady state. LABVIEW® 7.1 is used to closely monitor the temperature profile within the copper block as well as the bulk liquid temperature. The bulk liquid temperatures measured using the three calibrated K-type thermocouples positioned at different positions in the pool is controlled by making suitable adjustments to the circulating unit. Once the system reaches steady state for each power level, two minute data is recorded at 200 Hz. The temperature data collected is used to construct the boiling curve for the experiment. The multimeter is used to measure the voltages supplied to the two types of cartridge heaters and the clamp ammeter is used to measure the corresponding currents. The multimeter and ammeter readings are manually recorded in a data sheet. The time, circulating unit set-temperature and the temperature of the thermocouple closest to the surface of the copper block are also recorded in the data sheet. A Canon® Powershot S3 IS digital camera is used to capture still images of the boiling process at each steady state. Once all the data is recorded, the voltage is increased by 3 V for the next steady state point. As the system reaches Critical Heat Flux, the voltage steps are decreased to 2 V to get as close to the CHF as possible. If a voltage increment of 2 V causes the system to go into film boiling regime, the previous data is taken as representative of the value for the Critical Heat Flux condition.

After the CHF condition is reached, the system spontaneously transitions from nucleate boiling regime into the film boiling regime. During this process, the copper block temperatures increase rapidly because of the vapor layer formed on the test surface. At this time, the circulating unit is adjusted to maintain the given liquid bulk temperature. Also the power supply to the cartridge heaters is reduced to prevent burn-out. The system is allowed to reach steady state and the data is recorded. In the film boiling regime, after each steady state data acquisition, the power supplied is reduced gradually until the minimum heat flux point is reached. Further decrease in the power levels will cause the film to break and the system to transition back into the nucleate boiling regime. At this point, the power levels are decreased to zero and the copper block is allowed to cool while the bulk liquid is still contained in the chamber. The circulating unit is set at a temperature below room temperature to slightly expedite the process. This slow cooling prevents the copper block from developing internal stresses. Once the copper block reaches temperatures close to room temperature, the circulating unit is shut down and the test fluid is drained. The condensed liquid from the vapor line is also collected and can be re-used along with the drained test fluid if it is not contaminated by particles. Once the test surface has been completely tested, it is carefully dismantled by first removing the steel clamp, then the test surface, followed by the Pyrex wafer. The surfaces are then cleaned with Isopropyl alcohol to remove the heat sink compound. The set-up is then ready for mounting the next test surface.

4. RESULTS AND DISCUSSION

The pool boiling experiments are performed on the nano-structured surfaces and the results are compared with that of automatically smooth single crystal silicon test surfaces. The raw temperature data for the copper block is processed to obtain the heat flux in the vertical direction at each steady state condition. The heat flux is then plotted against the heater temperature for each experiment. As discussed earlier, Step and Flash Imprint Lithography (SFIL) was employed for the nano-fabrication of the test surfaces. Depending on the method of fabrication and the height of the nano-fins on the surfaces, the different enhanced test surfaces are denoted as *"100 nm"*, *"336 nm"*, *"259 nm"*. Since the bare silicon test surface is atomically smooth and does not have nano-fins on its surface, it was denoted as *"Bare"*. This nomenclature will be followed even in this section as before. This section is used to report and discuss the experimental results obtained from the experiments. The assistance provided by Vijaykumar Satyamurthi (Graduate student, Mechanical Engineering, Texas A&M University) in furnishing the experimental data for pool boiling on bare silicon is gratefully acknowledged.

4.1 Heat flux calculation

The heat flux through the copper block is calculated using Fourier's law of heat conduction [24],

$$q_{Cu}'' = -k_{Cu}\frac{\Delta T}{\Delta X} = -k_{Cu}\frac{(T_2 - T_9)}{\Delta X} \qquad (1)$$

Here, q_{Cu}" (W/cm^2) is the heat flux through the copper block, T_2 (°C) is temperature recorded by the thermocouple closest to the top of the copper block (0.125 inches or 0.3175 cm from the top) and T_9 (°C) is the temperature reading from the thermocouple that is in the same vertical plane and in the fourth horizontal level from the top of the copper block (0.875 inches or 2.2225 cm from the top). Both T_2 and T_9 are average values of the temperature recordings acquired for two minutes at 200 Hz at each steady state condition. Δx is the distance between the positions of the above two thermocouples (0.75 inches or 1.9050 cm). k_{Cu} is the thermal conductivity of copper taken to be 401 W/m K or 4.01 W/cm K with a relative uncertainty of ±1 %. At each steady state, the q_{Cu}" is calculated using the above equation. The point immediately after which transition into film boiling takes place is taken as the CHF. It has been mentioned that the copper block is surrounded by air on all sides. In addition, there is air trapped between the top of the copper block and the steel clamp in the areas other than that of the Pyrex wafer and the test surface. Also, thermal grease is applied on the different surfaces between the copper block and the test surface. Air being an insulator (thermal conductivity of 0.024 W/m K or 0.00024 W/cm K at room temperature) compared to the heat sink compound (0.55 W/m K or 0.0055 W/cm K at room temperature), 1-D heat conduction is assumed in the vertical direction. Hence, the heat transferred through the copper block passes through the exposed area of the test surface and the heat loss in the transverse direction

is neglected (error analysis for such an assumption is discussed in a later section). The comparison between the power input to the cartridge heaters and the average heat output from the calculations confirms that this is a valid approximation. As mentioned in the previous section ("Experimental Setup and Procedure"), the diameter of the cylindrical copper block is 3.5 inches (8.89 cm). Thus the top circular area of the copper block (A_{Cu}) is calculated to be 62.0716 cm^2. Also, it has been mentioned earlier that the exposed area of the silicon test surface to boiling is a 2.3125 (5.8738 cm) inches by 1.25 inches (3.175 cm) rectangle with rounded corners of 0.25 inches (0.635 cm) diameters. Thus the exposed area (A_w) is calculated to be 18.5626 cm^2. The ratio between the areas of the top surface of the copper block to the area of the test surface is calculated to be 3.3439 (A_{Cu}/A_w).

By law of conservation of energy, the heat passing through the copper block (Q_{Cu} - Watts) is equal to the heat through the test surface (Q_w -Watts). In other words,

$$Q_{Cu} = Q_w \tag{2}$$

Or,

$$q_{Cu}"\bullet A_{Cu} = q_w"\bullet A_w \tag{3}$$

Thus the heat flux through the test surface (q_w" in units of W/cm^2) is calculated as

$$q_w'' = \left(\frac{A_{Cu}}{A_w}\right) \cdot q_{Cu}'' \tag{4}$$

In other words,

$$q_w'' = 3.3439 \cdot q_{Cu}'' \tag{5}$$

All the curves comparing the results from different test surfaces are plotted between the heat fluxes as calculated above versus the corresponding temperatures T_2 (otherwise denoted as the *"heater temperature"*) since the surface temperatures are not directly measured during the experiments in the present study. Since the amounts of applied heat sink compound vary for each experiment, the thermal interface resistance between the copper block and the test surface can be different. Application of too little compound can introduce air gaps that increase the resistance. To estimate the wall temperature and hence its superheat for the present study, correlations are developed (that will be discussed shortly) from experiments that were undertaken with Thin-Film-Thermocouples (TFTs)[27] fabricated on the surface that measure the surface temperature. The application of correlations nevertheless introduces an approximation in the calculations and thus the first set of results will report and compare heat flux values plotted against the directly measured heater temperature in both the nucleate and film boiling regimes for the different test surfaces. The second set of results will use the wall superheat estimated through the correlations mentioned above to construct the boiling curve. Experiments were conducted at three levels of sub-cooling – 0 °C, 10 °C and 20

°C with the saturation temperature of the coolant (PF5060 – 3M® Co.) being 56 °C. All experiments were run at least twice to demonstrate repeatability.
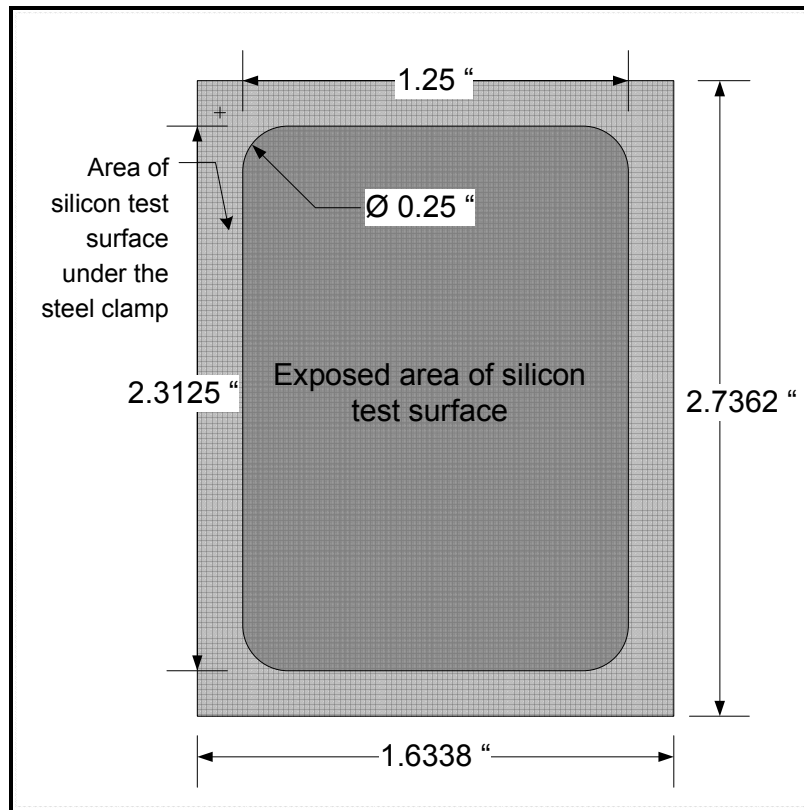
Fig. 13. Schematic showing the area of the test surfaces exposed to pool boiling (figure not to scale).

Upon nano-fabrication on four inch double-side-polished silicon wafers, the test surfaces are diced into rectangular pieces to be loaded on the set-up. The dicing is done using a DAD-2H/T dicing saw (DISCO® Co.) at the Materials Characterization Facility (Texas A&M University). The opening in the steel clamp has a width of 1.25 inches (3.175 cm) and a length of 2.3125 inches (5.8738 cm) with rounded corners of radius 0.25 inches (0.635 cm). The rectangular test surfaces 1.6336 inches by 2.7362 inches (4.15 cm by

6.95 cm) are made slightly larger than the opening of the steel clamp as shown in Fig. 13. This helps to clamp the Teflon gasket that is placed on the underside of the steel clamp to effectively clamp. The clamp presses the gasket on the test surface and provides a good seal.

4.2 Data processing for nano-fin coverage area

To accommodate for the stepping operation during the nano fabrication, the test surfaces are not completely covered with nano-fins. In addition, the test surfaces *"336 nm"* and *"259 nm"* suffered even lower coverage. Particles affected the imprinting process and all available regions on the surface could not be utilized for imprinting. Fig. 14 schematically illustrates the issues influencing surface coverage of nano-fins on silicon test surfaces. The regions of the test surfaces that were intended for nano-fins but could not be imprinted resulted in isolated regions with smooth silicon surface. To account for the loss of enhancement from lack of complete surface coverage, the experimental data had to be processed to obtain the heat flux through the projected nano-patterned plan area (q_n"). Further adjustments in results were explored by calculating the heat flux through the total nano-patterned area (q_{nc}"), which includes the surface area of the fins.
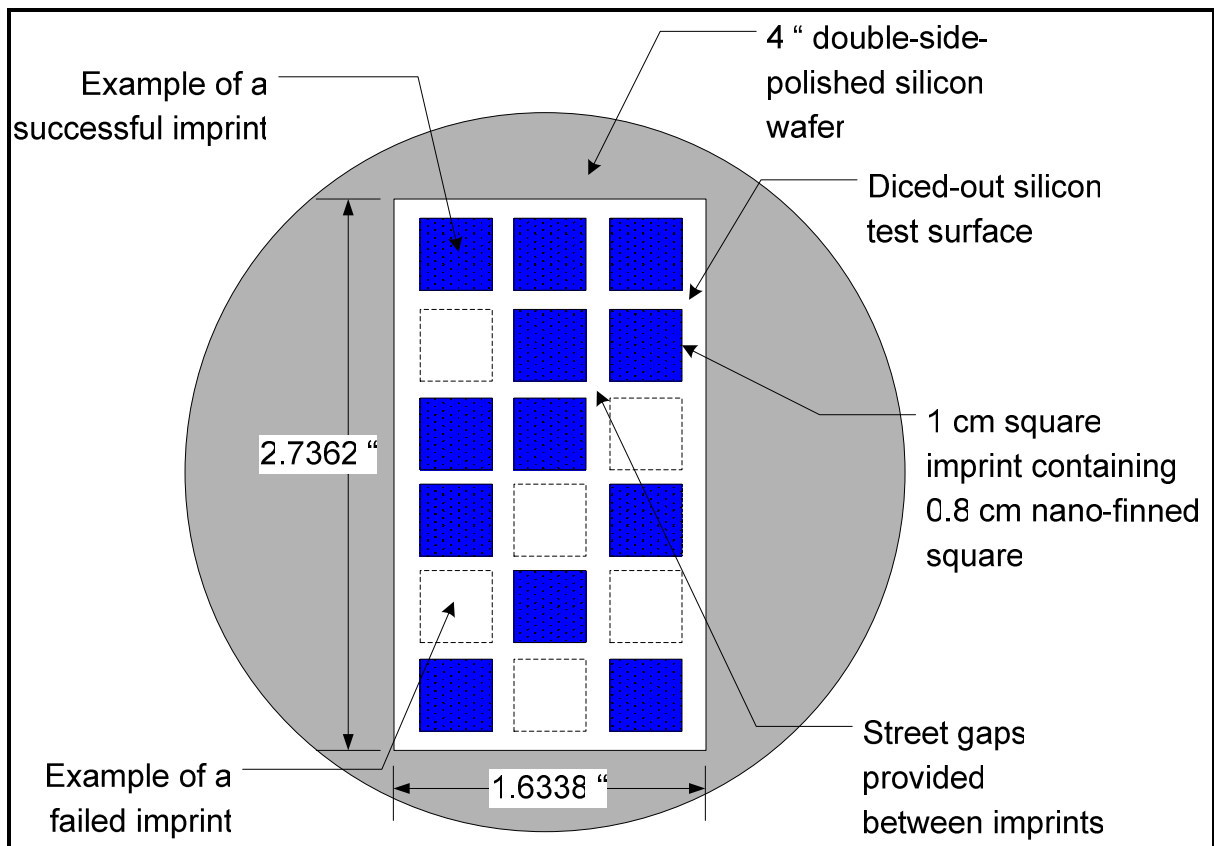
Fig. 14. Schematic diagram demonstrating the surface coverage issue of the enhanced test surfaces (figure not to scale).

Two sets of calculations are performed to account for the two different levels of heat fluxes that occur in these experiments. The first set of calculations account for the loss of enhancement because of the fact that the nano-fin patterns could not be fabricated over the entire exposed test surface due to technical limitations. The total heat flux through the complete test surface is divided into the higher heat flux through the nano-finned areas (side 8 cm) – q_n" (heat flux through the nano-patterned plan area) and lower heat flux through the smooth silicon areas, q_b". If the total area of the nano-patterned squares

is A_n, and the total area of the smooth silicon is A_b, where the total exposed area of the test surface to boiling is A_w (rectangular opening in the steel clamp). A_b is calculated as

$$A_b = A_w - A_n \qquad (6)$$

where A_n is calculated as below.

$$A_n = (0.64 cm^2) \cdot N \qquad (7)$$

In the above equation (0.64 cm^2) is the area of each nano-patterned square and N is the number of such nano-finned squares on the given test surface.

By the law of conservation of energy:

$$q_n" A_n + q_b" A_b = q_w" A_w = x \cdot q_b" A_w \qquad (8)$$

where q_w" (W/cm^2) is the raw data for the total heat flux through the test surface (prior to the data processing). In other words, q_w" is the experimental heat flux obtained directly from the data for the nano-finned surfaces. x is the factor by which the total experimental heat flux (q_w") through the partially-covered nano-finned test surface is greater than the experimental heat flux through the bare test surface q_b" (W/cm^2) for each corresponding heater temperature configuration.

$$x = \frac{q_w{}''_{(T2)}}{q_b{}''_{(T2)}} \qquad (9)$$

Equation (8) is then solved for q_n'' as follows,

$$q_n'' = \frac{q_w'' A_w - q_b'' A_b}{A_n} \qquad (10)$$

where q_b'' is the calculated bare silicon heat flux corresponding to a given steady-state heater temperature and sub-cooling configuration of the nano-finned surfaces. To obtain this, a trend-line is drawn to the experimental data of q_b'' versus T_2 (heater temperature) curve and the corresponding trend-line equations are found using Microsoft® Excel. The equations are then applied to find q_b'' at given T_2 values.

In some cases, the heater temperature corresponding to CHF for a given nano-finned surface exceeds the heater temperature corresponding to experimental CHF for the bare surface. In other words $T_{2,CHF}$ for the nano-finned surface is slightly greater than the $T_{2,CHF}$ for the bare surface. In such cases, the q_b'' value calculated is forced to $q_{CHF,b}''$ obtained from the bare test surface experimental data. This is done because the trend-line equation does not hold good beyond $T_{2,CHF}$ of the bare surface experimental data and also because $q_{CHF,b}''$ is the maximum possible heat flux with the bare silicon surface.

The next level of data processing is performed to incorporate the total surface area of the fins and to find the heat flux through the nano-fins and their base areas (in other words, the heat flux through the nano-patterned area) – q_{nc}". As explained earlier, *"100 nm"* test surface contains 200 nm diameter cylinders with a height of 100 nm. *"336 nm"* has fins in the form of frustums of cones. The average height of these structures was found to be 336 nm with the larger and smaller diameters of 100 nm and 65 nm respectively. *"259 nm"* has well-defined cylindrical structures with an average height of 259 nm and diameter of 186 nm. The pitch of all three enhanced test surfaces is 1 μm in the longitudinal direction and 0.9 μm in the transverse direction. From the pattern created, each imprinted square contains 8000 columns and 8890 rows of nano-fins. Thus, a total of approximately 7.1×10^{7} nano-fins are present in an 8 cm by 8 cm nano-finned square irrespective of the shape of the structures obtained from the final etching step. By law of conservation of energy:

$$q_{nc}" A_{nc} = q_{n}" A_{n} \tag{11}$$

Here, q_{nc}" (W/cm^2) is the heat flux through nano-patterned area. A_{nc} (cm^2) is the total nano-finned area exposed to boiling which is the summation of the total nano-finned square base area of the test surface and the total lateral surface area of the nano-fins. A_{nc} is calculated as follows for test surfaces *"100 nm"* and *"259 nm"* because the nano-fins are in the form of cylinders.

$$A_{nc} = A_n + (2\pi rh) \bullet N \bullet n \qquad (12)$$

In the above equation, r (nm) is radius of the nano-fin and h (nm) is the height of the

nano-fin. N is the number of nano-finned squares and n is the number of nano-

fins/square (approximately 7.112×10^7 nano-fins/square). Because of the size of the

imprinted squares and the intended gap between them, a maximum of 16 nano-finned

squares can be present in the exposed rectangular area of the test surface (5.8738 cm by

3.175 cm). For the *"100 nm"* test surface the number of nano-finned squares (N) is 16.

For the *"259 nm"* test surface, the value of N was 9 because of particles disrupting the

imprinting process.

In the case of test surface *"336 nm"*, the nano-fins were in the form of frustums of

cones. In this case, A_{nc} is calculated as below.

$$A_{nc} = A_n + \left[\pi(r_1 + r_2)l\right] \bullet N \bullet n \qquad (13)$$

The slant height l (nm) is calculated as follows

$$l = \sqrt{(r_2 - r_1)^2 + h^2} \qquad (14)$$

In equation(13), r_1 (nm) is the smaller radius, r_2 (nm) is the larger radius, and l (nm) is

the slant height of the frustum where l is calculated using equation(14). As in the

previous case, N is the number of nano-finned squares and n is the number of nano-fins/square (approximately 71 billion nano-fins/square). In equation(14), h (nm) is the height of the frustums. For the *"336 nm"* test surface, the number of nano-finned squares is only 7 because of particles disrupting the imprinting process. Using equation(11), the value of q_{nc}" is calculated as the heat flux through nano-patterned areas.

4.3 Estimation of uncertainty

The uncertainty of measurement was done based on the Kline and Mc-Clintock procedure [28]. The expression used for calculating the relative uncertainty is given below

$$\frac{\omega_q"}{q"} = \sqrt{\left(\frac{\omega_k}{k}\right)^2 + \left(\frac{\omega_{T_2}}{T_2 - T_9}\right)^2 + \left(\frac{\omega_{T_9}}{T_2 - T_9}\right)^2 + \left(\frac{\omega_{\Delta x}}{\Delta x}\right)^2} \qquad (15)$$

Here, ω is the uncertainty in the particular value denoted by its subscript. The uncertainty in the thermal conductivity k_{Cu} of copper is taken as ±1 %. The relative uncertainty in the positioning of the thermocouples and hence Δx is taken as ±3 %. Finally, the uncertainties in the average thermocouple readings for the two minute data are determined using a 95% confidence. The absolute uncertainty in the heat flux is then calculated using the equation above and plotted on the boiling curve as error bars for heat flux data.

4.4 Results – Set 1

4.4.1 Saturation condition results- set 1

The first set of results is shown for experiments run under saturation condition. Fig. 15, Fig. 16, Fig. 17, and Fig. 18 show the results for the heat flux through the test surface (q_w"), the heat flux through the nano-patterned plan area (q_n"), and the heat flux through the nano-patterned area (q_{nc}") respectively. All the results are plotted with respect to heater temperature. The experiments for each of the modified test surfaces were conducted twice and both the runs are shown in the results below. The results are compared with that of a bare test surface. All the plots include error bars depicting the absolute error in heat flux calculation. The relative uncertainty in the heat flux measurements was found to be 8 % near CHF condition and 41 % at and incipience for the *"100 nm"* nano-finned surface. Similarly the relative uncertainty for the *"259 nm"* and *"336 nm"* test surfaces were between 9% and 38 %, and 9% and 37 % respectively.

It is evident from the plot for q_w" (Fig. 15) that the enhancement in heat fluxes for the nano-finned surfaces is negligible in the film boiling regime. Thus the data for q_n" and q_{nc}" did not include the results in the film boiling regime for both the first and second sets of results. Also, the interpolation of the bare heat flux data q_b" could not be performed to calculate q_n" and hence q_{nc}" in some cases since the heater temperatures for the nano-finned surfaces did not overlap those of the bare surfaces as in the nucleate boiling regime. In addition, literature [29, 30] suggests that the vapor layer in film boiling is estimated around 15 μm which is too thick even for the tallest nano-fins (336

nm height) in the present study. Hence the data processing for q_n and q_{nc} did not include film boiling.

From Fig. 15, in the nucleate boiling regime, the nano-finned surfaces exhibit a higher heat flux compared to the bare silicon surface. The boiling incipience for the nano-finned surfaces occurs at higher heater temperatures (5-7 °C) compared to the bare surface. The heat flux levels are similar for the nano-finned surfaces at lower heater temperatures of up to approximately 95 °C after which the curves start diverging with higher heater temperatures and near the CHF. The *"100 nm"* test surface shows the highest CHF (enhancement of about 57 % compared to the bare surface) followed by the *"259 nm"*, *"336 nm"* and the bare test surfaces. It is also observed that the CHF for the bare surface occurs at a higher heater temperature compared to the *"259 nm"* test surface and almost at the same temperature as that of the *"100 nm"* test surface. The *"336 nm"* test surface however reached CHF at a slightly higher heater temperature than that of the bare surface. The repeat experiments showed good corroboration with the first set of runs. As mentioned earlier, the film boiling regime does not show much enhancement within the range of experimental uncertainty. Thus, the same plot is shown only for nucleate boiling regime in Fig. 16.

Fig. 17 shows the results for heat flux through the nano-patterned plan areas (q_n"), plotted against T_2. It is clear that the data processing has an effect on the predicted heat flux. It is interesting to note that the curves for the three enhanced test surfaces tend to overlap within the limits of the experimental error. In addition, all nanostructured surface data show enhancement compared to the atomically smooth silicon surface, beyond the limits of the experimental uncertainity. Comparison between Fig. 16 and Fig. 17 shows that the nucleate boiling heat flux levels are higher for the nano-finned squares. The $q_{n,CHF}$" being between 22 and 24 W/cm^2 compared to a maximum of 17 W/cm^2 for $q_{w,CHF}$". The heat flux curves have better convergence towards the higher heat flux levels especially near CHF. Within the range of experimental uncertainty, the three enhanced surfaces do not show heat flux enhancement between each other at CHF. The repeatability of experiments is proved in the multiple experiments that were performed for the same values of the experimental parameters.

Fig. 18 shows the results of heat flux through the nano-patterned areas (q_{nc}"). The overall trend is the same as q_n". The curves for the different runs on the various surfaces tend to increasingly overlap with each other towards the CHF condition. The overall nucleate boiling heat flux is slightly lower (about 19 – 22 W/cm^2) compared to 22 - 24 W/cm^2 for q_n". This is because of the additional area for the inclusion of the lateral surface area of the nano-fins. The maximum heat flux (q_n") value is highest for *"336 nm"* followed by *"100 nm"*, *"259 nm"*, and the bare test surface and the heat flux values overlap within the bounds of experimental uncertainty. The heater temperatures at CHF also follow the same decreasing order as the heat flux data at the CHF condition with the *"336 nm"* showing the highest heater temperature and *"259 nm"* showing the lowest heater temperatures for the three nano-structured surfaces.

The results for saturation condition show that the projected heat flux through the nano-fins seems to be independent of the height of the nano-fins (due to overlap of the boiling curves).
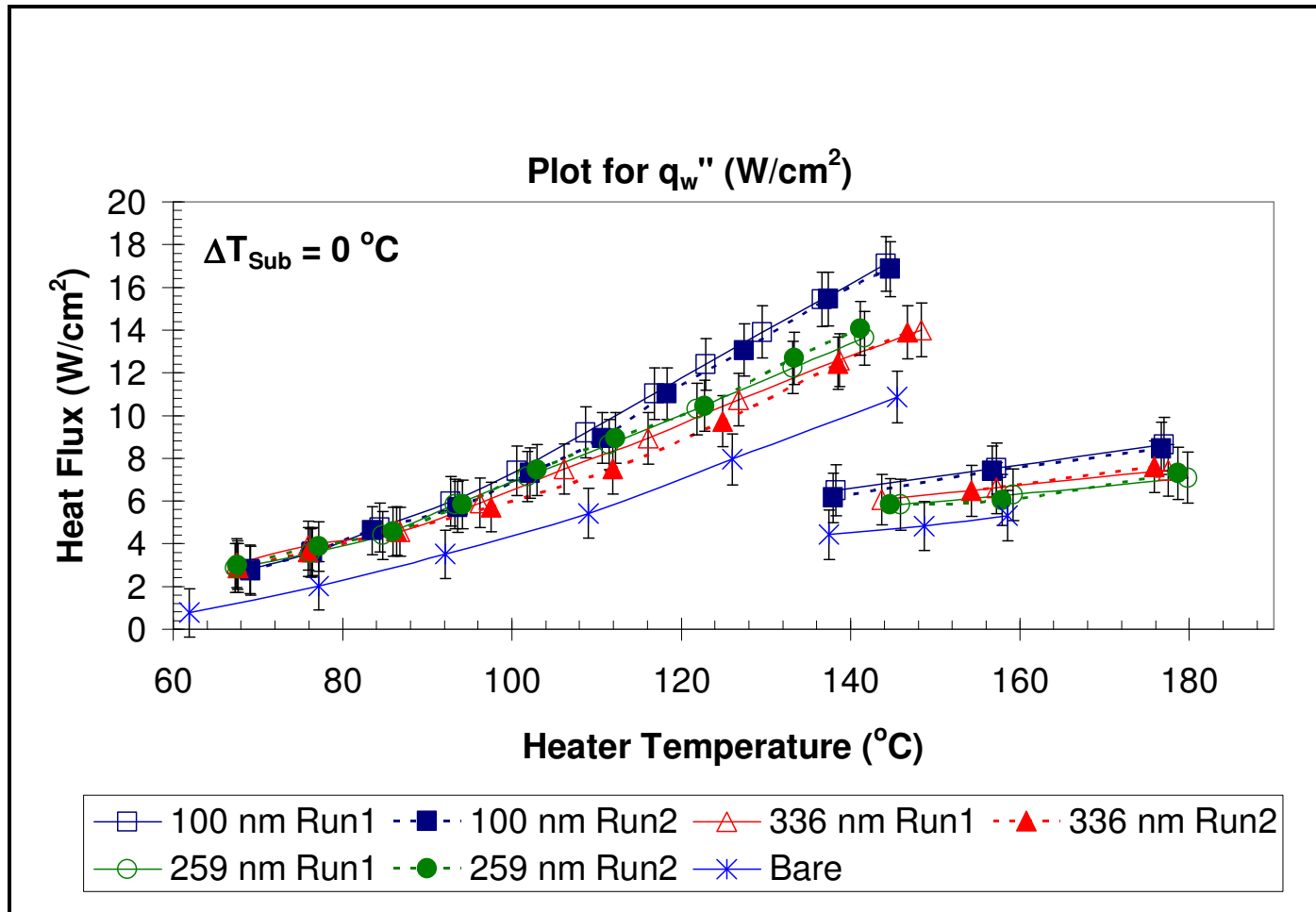
Fig. 15. Plots comparing the heat fluxes through the enhanced test surfaces (q_w'') with the heat flux through the bare test surface (q_b'') under saturation condition for both nulceate and film boiling regimes. Heat flux data is plotted against heater temperature (T_2).
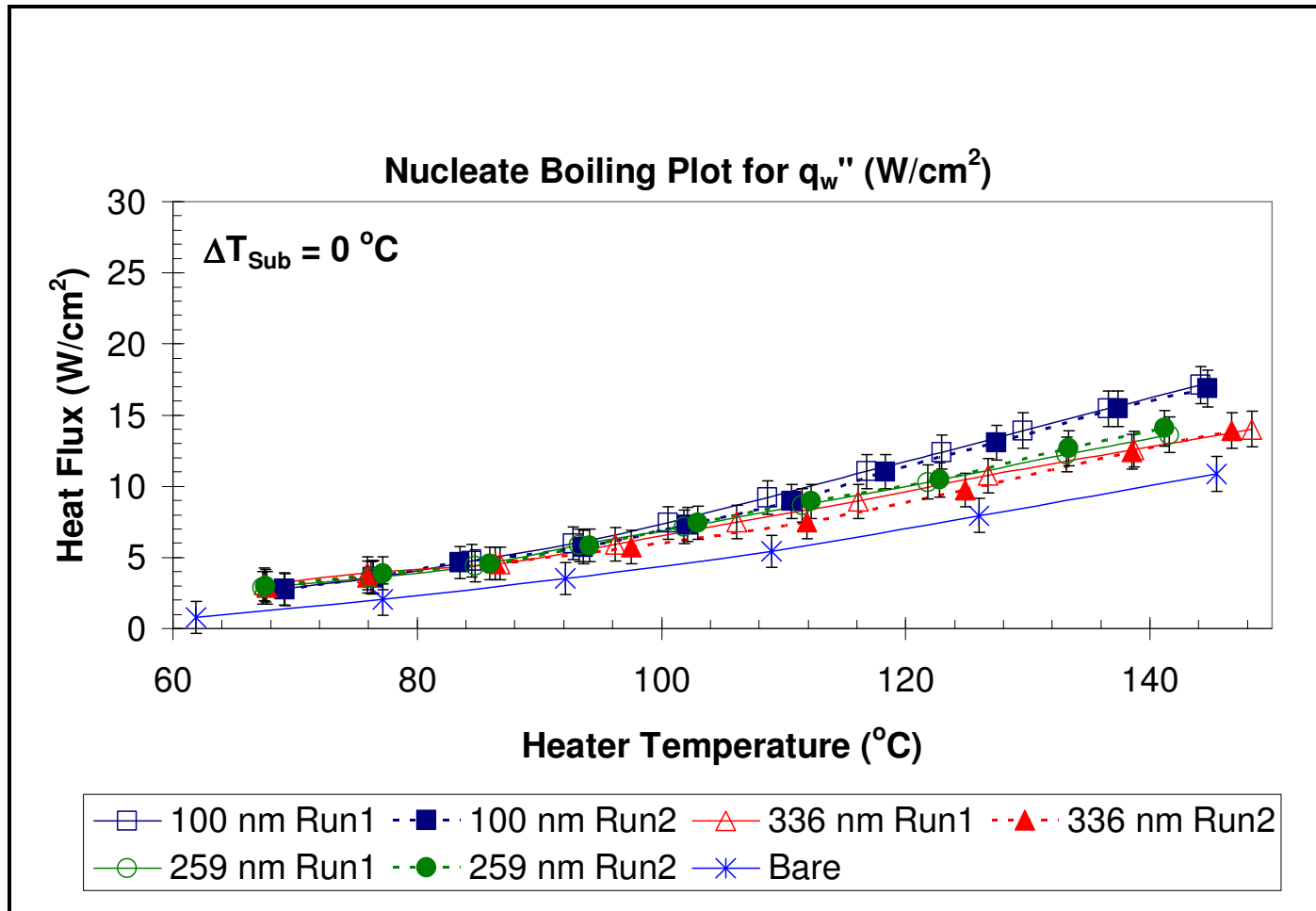
Fig. 16. Plots comparing the heat flux through the enhanced test surfaces (q$_w$'') with the heat flux through the bare test surface (q$_b$'') under saturation condition for the nucleate boiling regime. Heat flux data is plotted against heater temperature (T$_2$).

Fig. 17. Plots comparing the heat flux through the nano-patterned plan areas for the enhanced test surfaces (q_n") with the heat flux through the bare test surface (q_b") under saturation condition for the nucleate boiling regime. Heat flux data is plotted against heater temperature (T_2).

Fig. 18. Plots comparing the heat flux through the nano-patterned areas for the enhanced test surfaces (q_{nc}'') with the heat flux through the bare test surface (q_b'') under saturation condition for the nucleate boiling regime. Heat flux data is plotted against heater temperature (T_2).

4.4.2 10 °C sub-cooling condition results- set 1

Fig. 19, Fig. 20, Fig. 21 and Fig. 22 show the results from the 10 °C sub-cooling experiments. Experiments were run at least twice in this condition to check for repeatability. The q_w" versus T_2 curve shows that the enhanced surfaces have a slightly higher heat flux compared to the bare surface in the nucleate boiling regime but the enhancement is only marginal. The *"100 nm"* test surface shows the maximum enhancement in $q_{w,CHF}$" followed by *"336 nm"*, *"259 nm"* and the bare test surfaces. There is an anomalous trend for the first run of the *"336 nm"* test surface experiment with a lower CHF value compared to the *"259 nm"* test surface. The overlap of the enhanced surface curves is prominent up to about 110 °C heater temperature after which they start diverging as in the saturation condition. The degree of divergence is not as high as in the saturation case. The boiling incipience again occurs at a slightly higher heater temperature compared to the bare surface and all but one enhanced surface curve have a $T_{2,CHF}$ lower than that of the bare surface. The one run that slightly exceeded this temperature was for the second run of *"336 nm"* test surface. The different curves in the 10 °C sub-cooling condition do not show as good a repeatability as the saturation condition runs. As mentioned earlier, there is lack of notable enhancement in the film boiling regime and is within the experimental uncertainty limits. In addition, the *"336 nm"* and *"259 nm"* test surfaces show anomalous behavior with poor repeatability in the film boiling regime. Fig. 20 shows the comparison of plots for q_w" in the nucleate boiling region alone.

The relative uncertainty in the heat flux measurements was found to be between 7 % near the CHF condition and 37 % at incipience for the *"100 nm"* nano-finned surface. Similarly the relative uncertainty for both the *"259 nm"* and *"336 nm"* test surfaces were found to be between 9% and 39 % respectively.

Fig. 21 and Fig. 22 show the results for q_n" and q_{nc}" for the 10 °C sub-cooling condition. Even though the experiments do not show as good a repeatability as in the saturation condition, the nano-finned surface curves clearly tend to overlap with each other towards the CHF condition as in the saturation condition. As would be expected, the heat flux $q_{n,CHF}$" is slightly higher (20.5 – 23.5 W/cm^2) compared to $q_{nc,CHF}$" (18 – 21 W/cm^2) because of the added surface area of the fins for q_{nc}" calculation. The above data excludes the result from the first run of the *"259 nm"* test surface since it shows an anomalous trend compared to the other two runs. Thus, there is an anomalous trend for the first runs of both the *"336 nm"* and the *"259 nm"* test surfaces. The highest $q_{nc,CHF}$" is shown by the third run of *"336 nm"* test surface with an enhancement of about 58 % compared to the smooth surface.
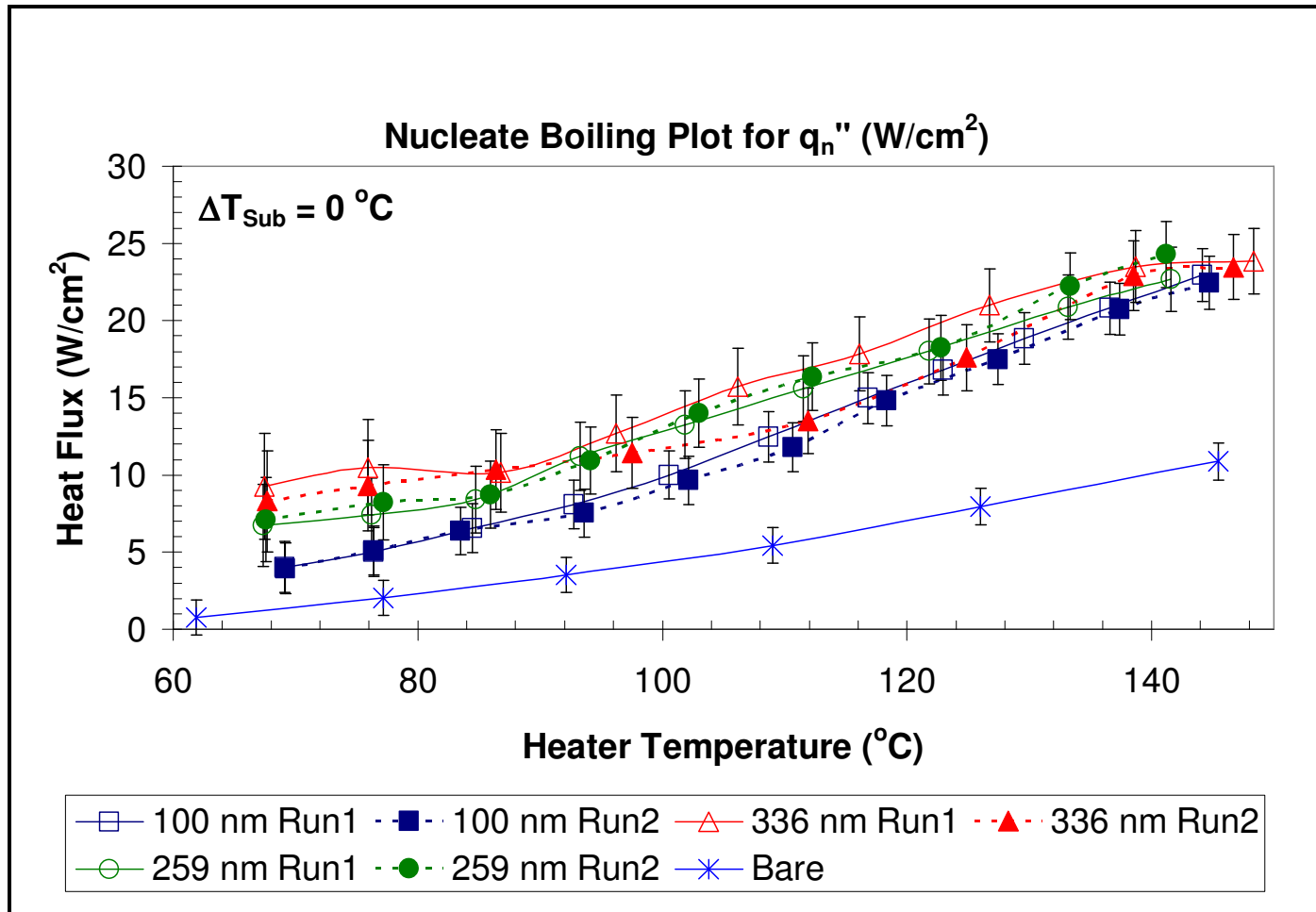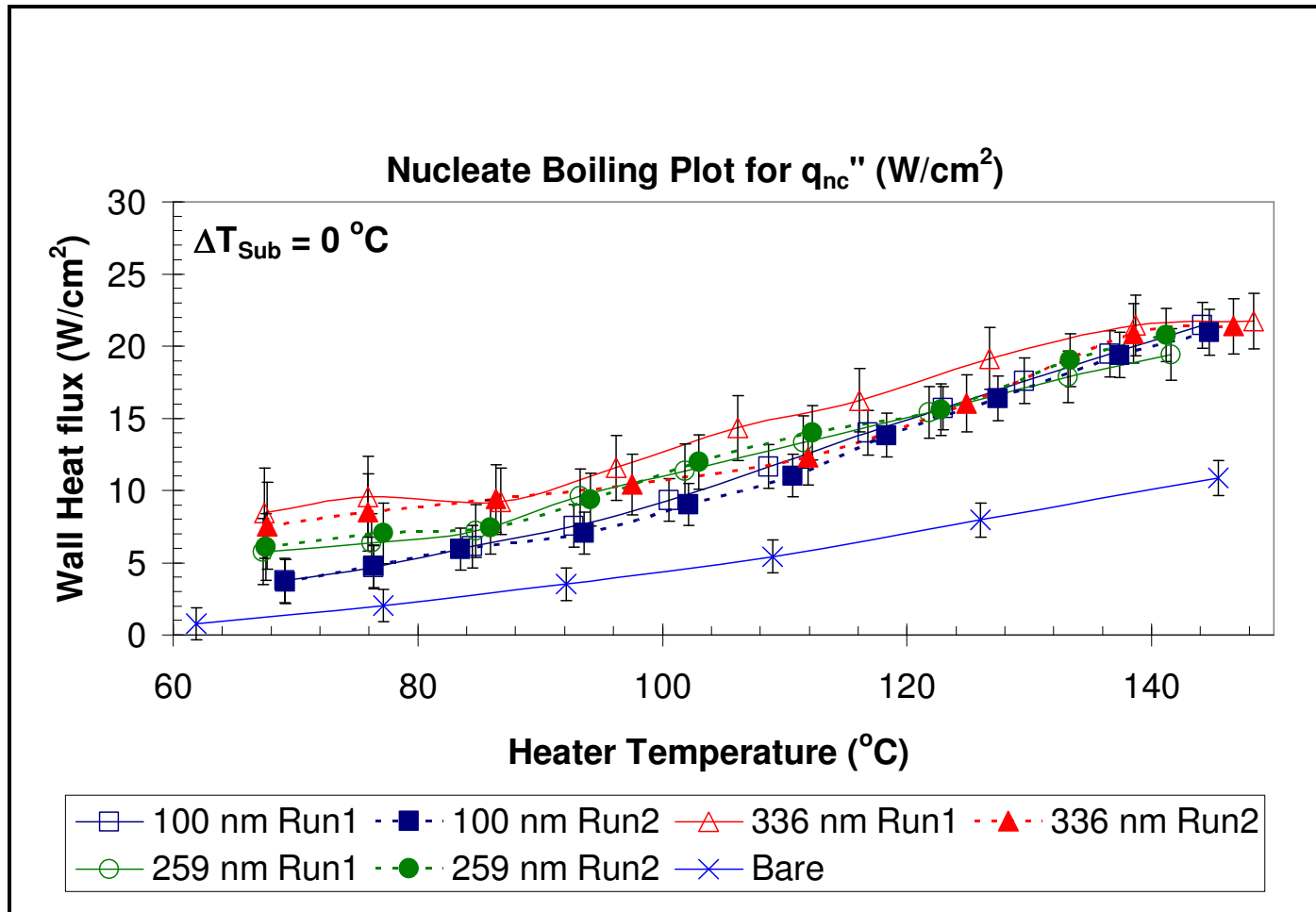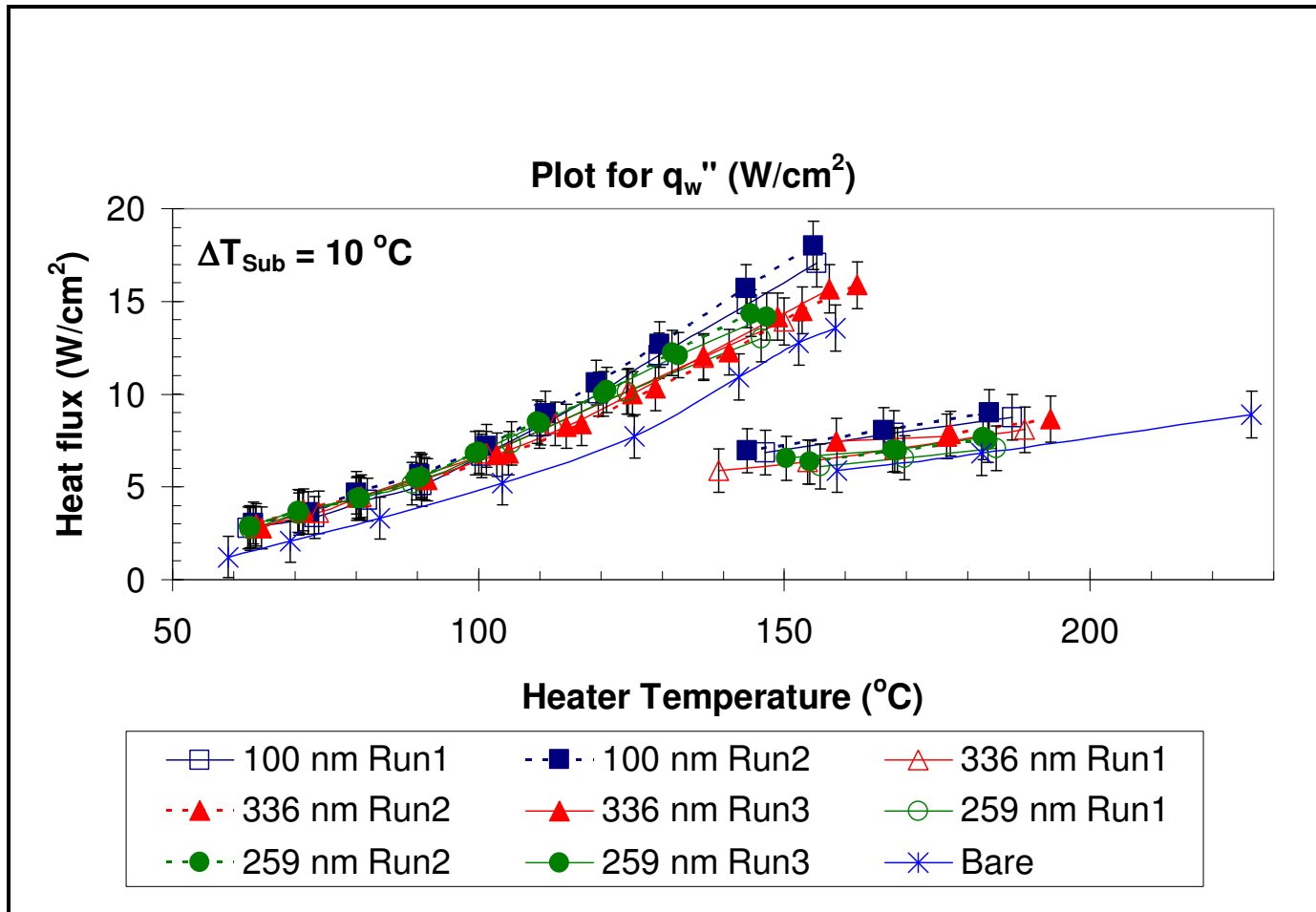
Fig. 19. Plots comparing the heat flux through the enhanced test surfaces (q_w'') with the heat flux through the bare test surface (q_b'') under 10 °C sub-cooling condition for both nulceate and film boiling regimes. Heat flux data is plotted against heater temperature (T_2).

Fig. 20. Plots comparing the heat flux through the enhanced test surfaces (q$_w$") with the heat flux through the bare test surface (q$_b$") under 10 °C sub-cooling condition for the nucleate boiling regime. Heat flux data is plotted against heater temperature (T$_2$).

Fig. 21. Plots comparing the heat flux through the nano-patterned plan areas for the enhanced test surfaces (q_n") with the heat flux through the bare test surface (q_b") under 10 °C sub-cooling condition for the nucleate boiling regime. Heat flux data is plotted against heater temperature (T_2).

Fig. 22. Plots comparing the heat flux through the nano-patterned areas for the enhanced test surfaces (q_{nc}") with the heat flux through the bare test surface (q_b") under 10 °C sub-cooling condition for the nucleate boiling regime. Heat flux data is plotted against heater temperature (T_2).

4.4.3 20 °C sub-cooling condition results- set 1

The q_w" data results (Fig. 23) show that the curves for the nano-finned surfaces overlap until about a heater temperature of 110 °C after which they start diverging, the divergence being not as high as in the saturation case. The nano-finned surfaces show a slightly higher heat flux values compared to the bare surface. The $q_{w,CHF}$" is the highest for the *"100 nm"* surface followed by the *"336 nm"*, *"259 nm"* and the bare surfaces. The heater temperature at CHF is the highest for the *"336 nm"* test surface among the nano-finned surfaces and is higher than even that of the bare test surface by about 5 °C in the first run. The next highest $T_{2,CHF}$ is exhibited by *"100 nm"* test surface followed by the *"259 nm"* test surface both of which are lower than that of the bare surface. There is good repeatability of data between the different runs of the nano-finned surface experiments for the q_w" data. The enhancement in the film boiling regime is only within the limits of uncertainty. In addition, the *"336 nm"* and *"259 nm"* test surfaces show anomalous behavior with poor repeatability. Thus this data is excluded while reporting q_n" and q_{nc}" as mentioned earlier. The q_w" data for the nucleate boiling regime alone is represented in Fig. 24.

The relative uncertainty in the heat flux measurements was found to be between 6 % near the CHF condition and 39 % at incipience for the *"100 nm"* test surface. Similarly the relative uncertainty for the *"259 nm"* and *"336 nm"* test surfaces were between 8 % and 40 %, and 7% and 38 % respectively.

Fig. 25 and Fig. 26 show the q_n" and q_{nc}" results plotted versus the heater temperature. Again, it is clear that there is merging of the heat flux data for the nano-finned surfaces as in the saturation and 10 °C sub-cooling cases. The nucleate boiling regime on the whole for the nano-finned surfaces shows an enhancement in heat flux compared to the bare surface. Analysis of the q_{nc}" results show that the *"336 nm"* test surface shows the greatest $q_{nc,CHF}$" followed by the *"100 nm"* test surface followed by the *"259 nm"* test surface. Even the heater temperatures at CHF followed the same decreasing order for the different enhanced surfaces. The *"336 nm"* test surface showed an enhancement of about 54 % in $q_{nc,CHF}$" compared to the bare surface.

The plots for q_{nc}" in the saturation, 10 °C sub-cooling and 20 °C sub-cooling conditions show that for a given heater temperature, the heat flux is almost the same for the nano-finned surfaces with a certain degree of enhancement compared to the bare surface. Thus, it is clear that certain nano-scale transport phenomena are responsible for this trend in the results.
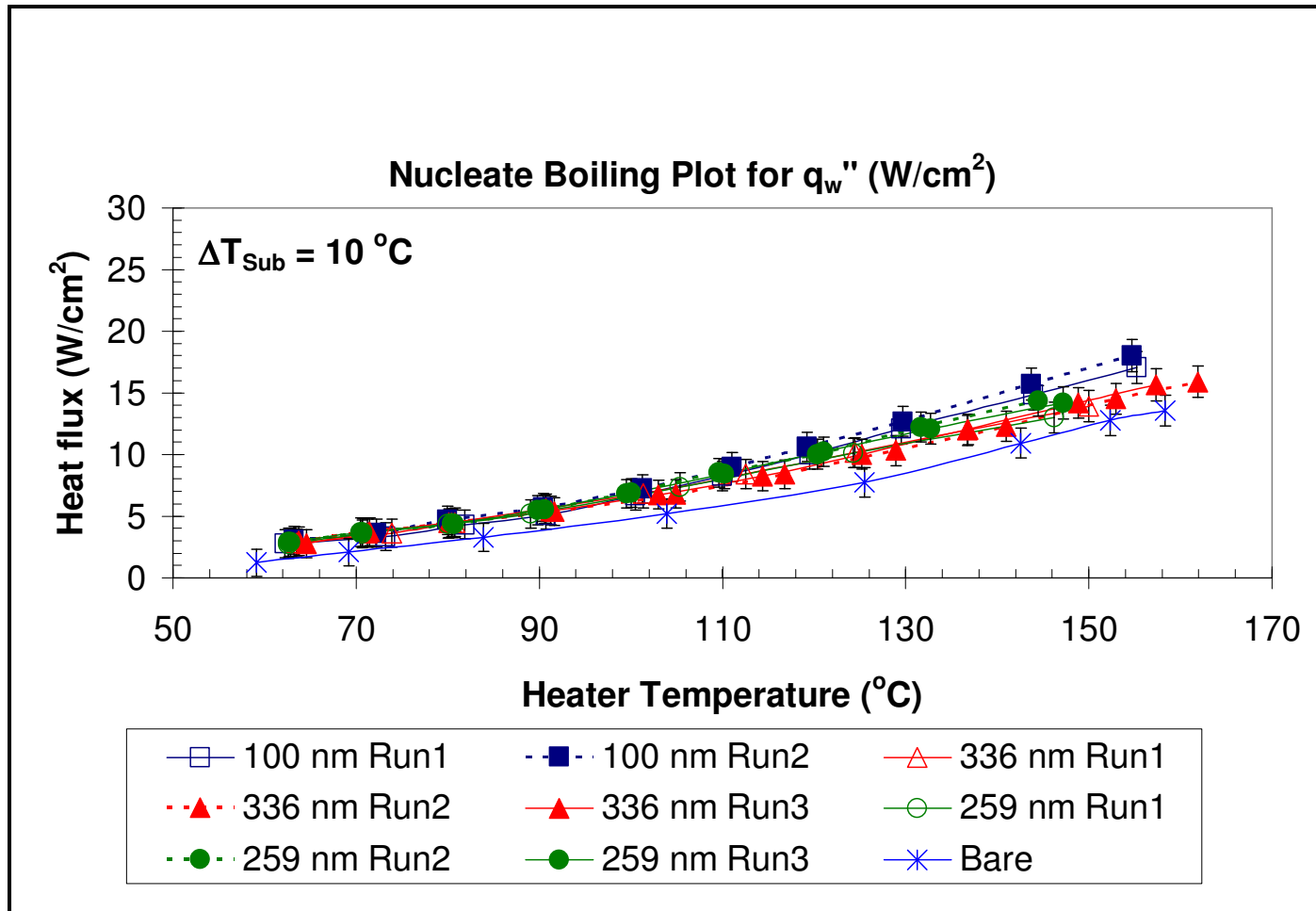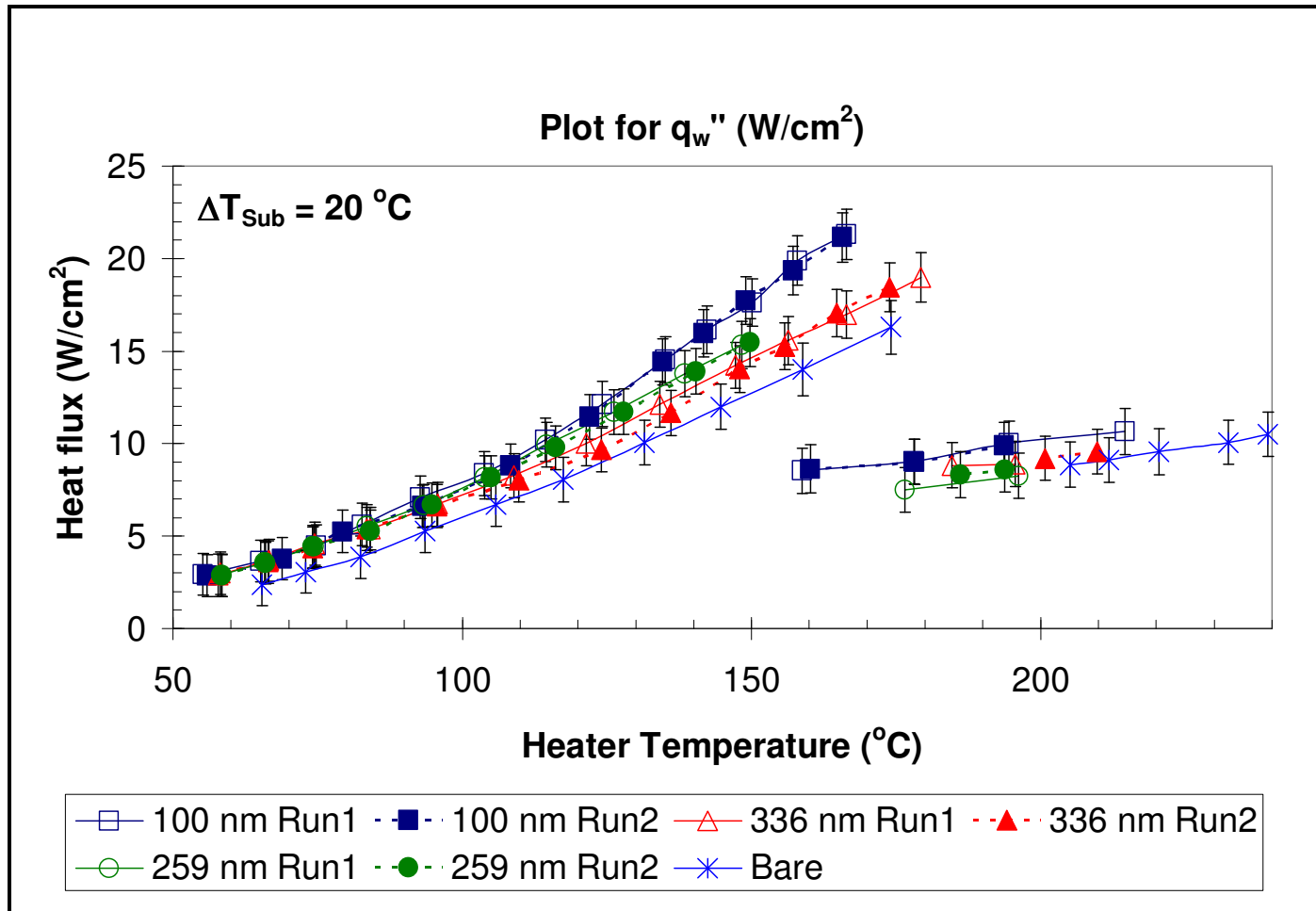
Fig. 23. Plots comparing the heat flux through the enhanced test surfaces (q_w'') with the heat flux through the bare test surface (q_b'') under 20 °C sub-cooling condition for both nulceate and film boiling regimes. Heat flux data is plotted against heater temperature (T_2).
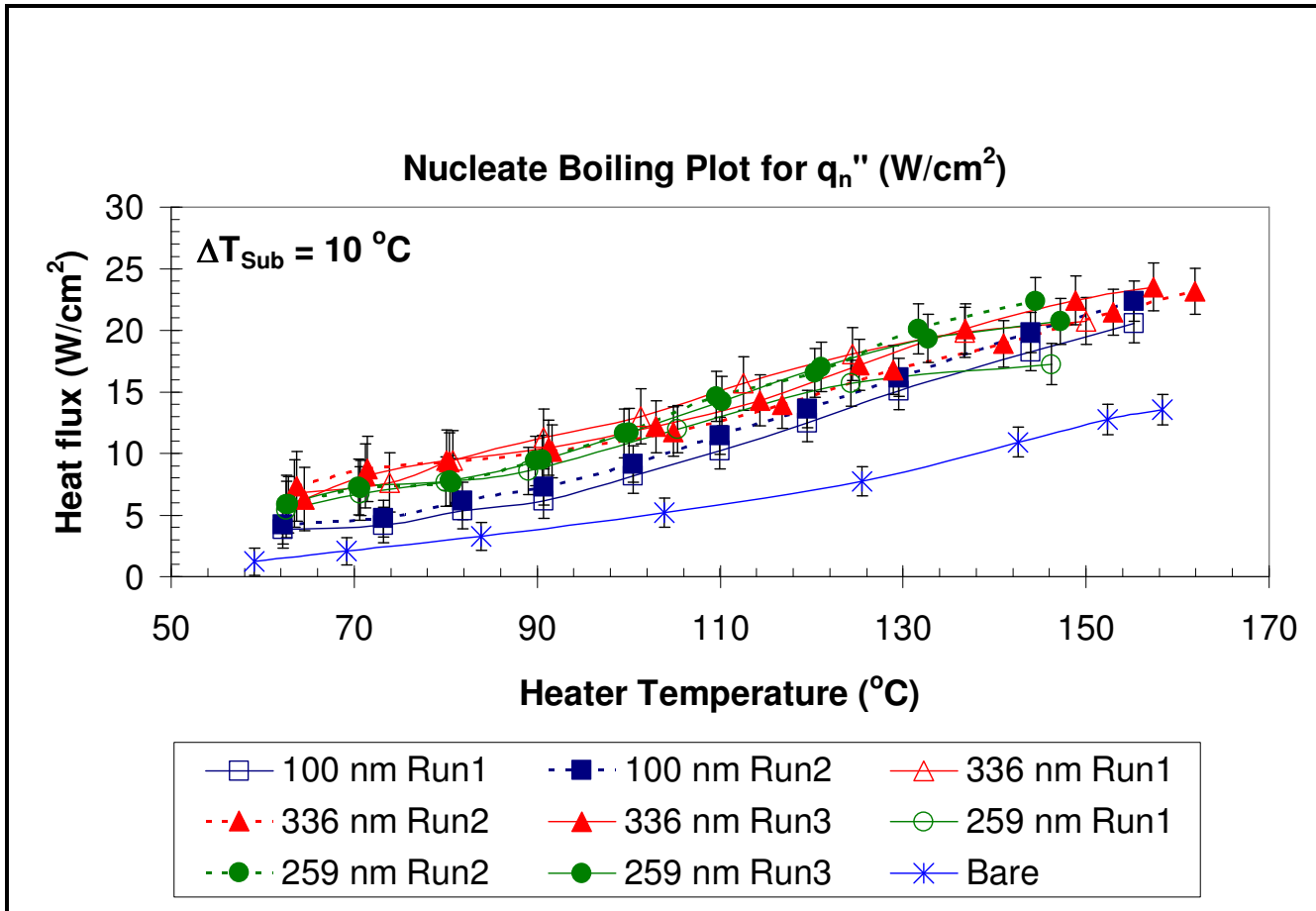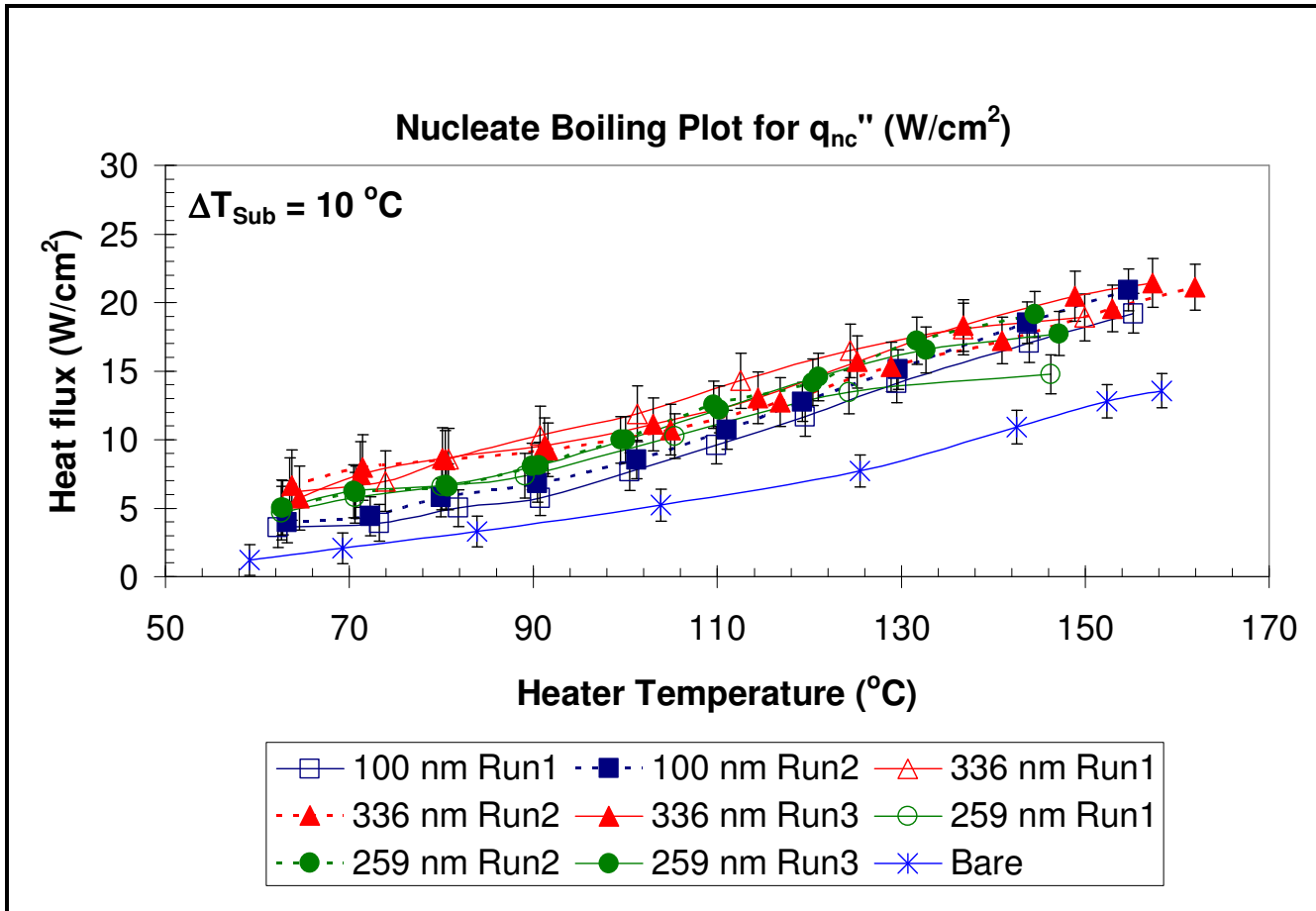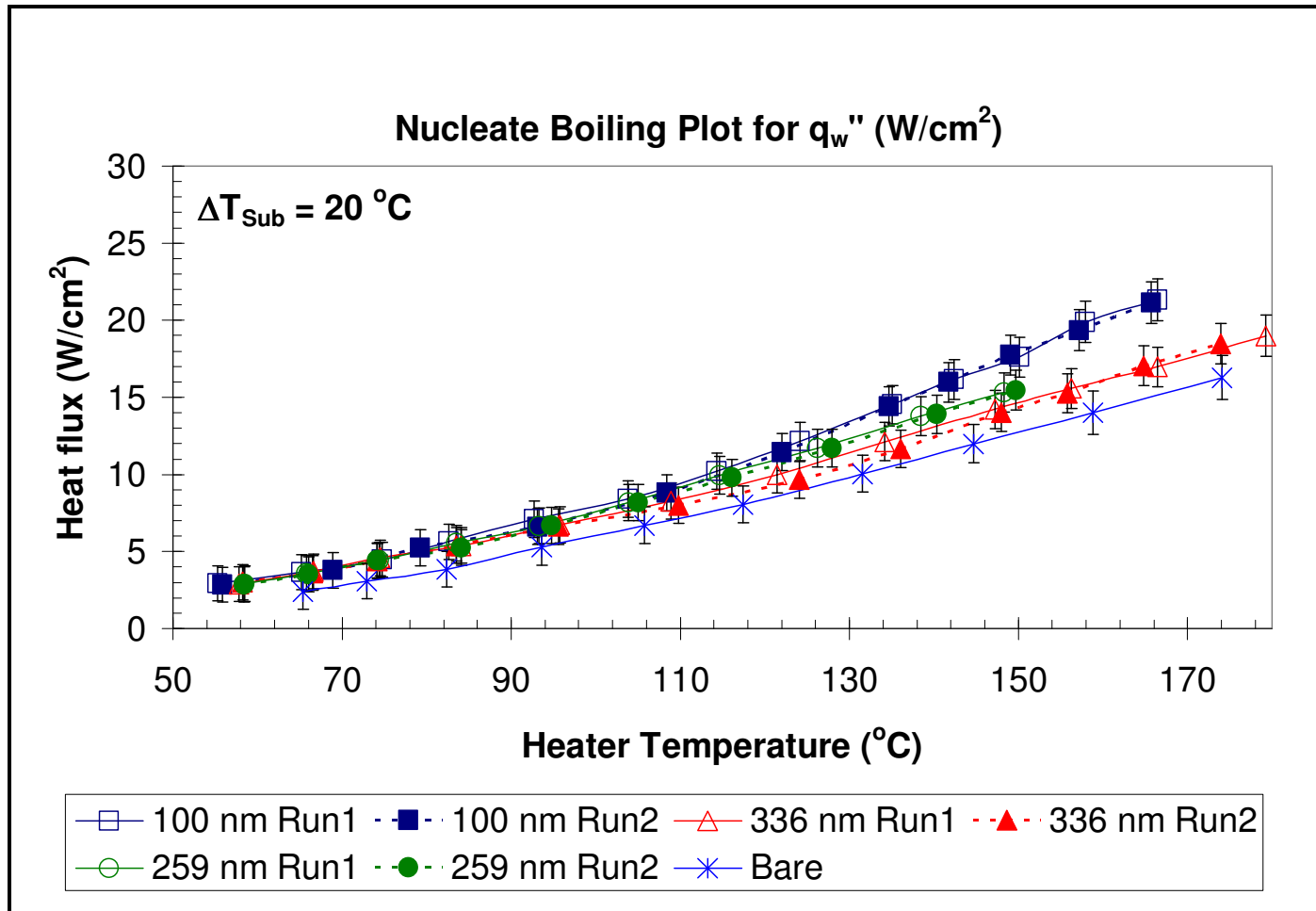
Fig. 24. Plots comparing the heat flux through the enhanced test surfaces (q_w'') with the heat flux through the bare test surface (q_b'') under 20 °C sub-cooling condition for the nucleate boiling regime. Heat flux data is plotted against heater temperature (T_2).
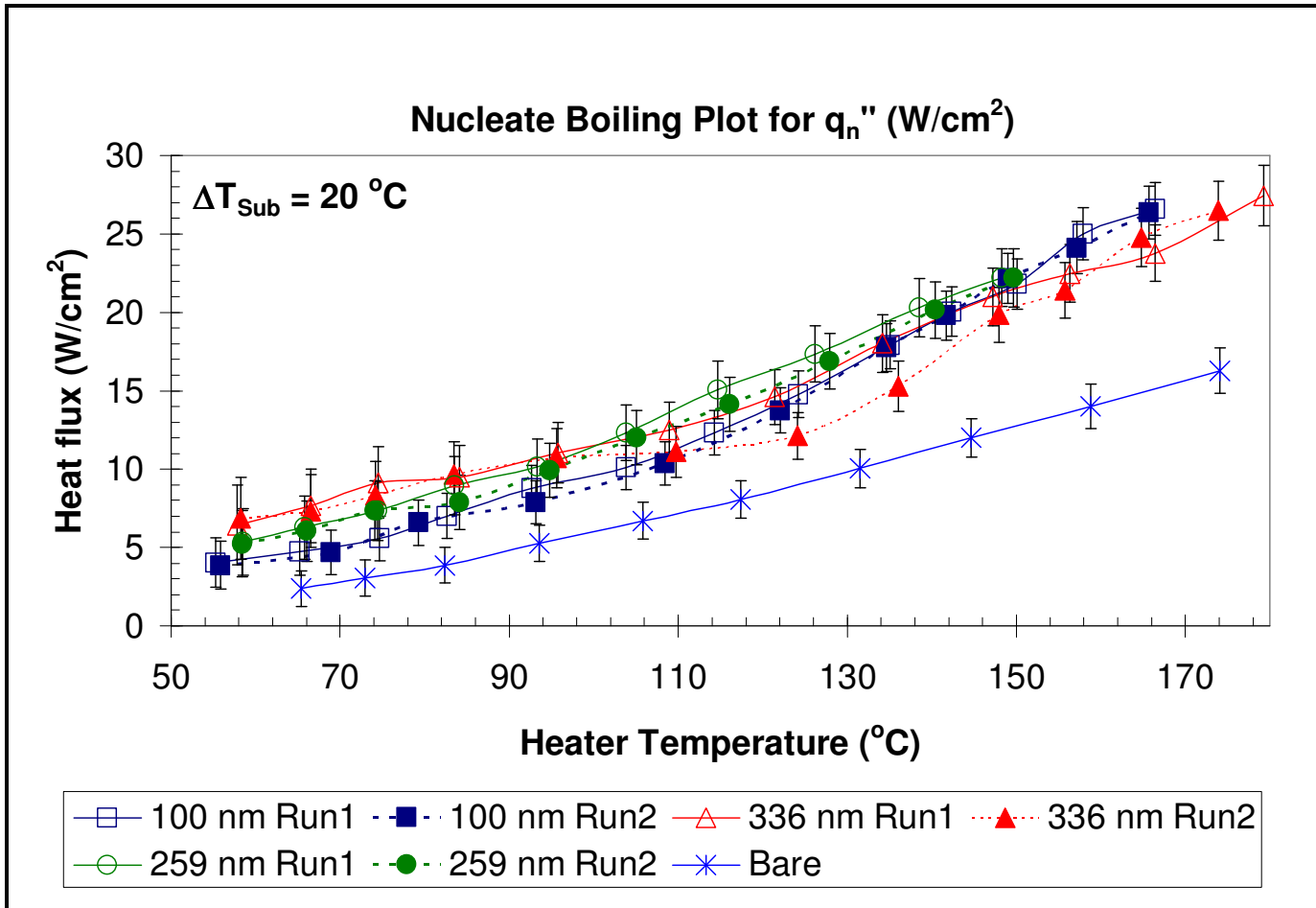
Fig. 25. Plots comparing the heat flux through the nano-patterned plan areas for the enhanced test surfaces (q_n") with the heat flux through the bare test surface (q_b") under 20 °C sub-cooling condition for the nucleate boiling regime. Heat flux data is plotted against heater temperature (T_2).
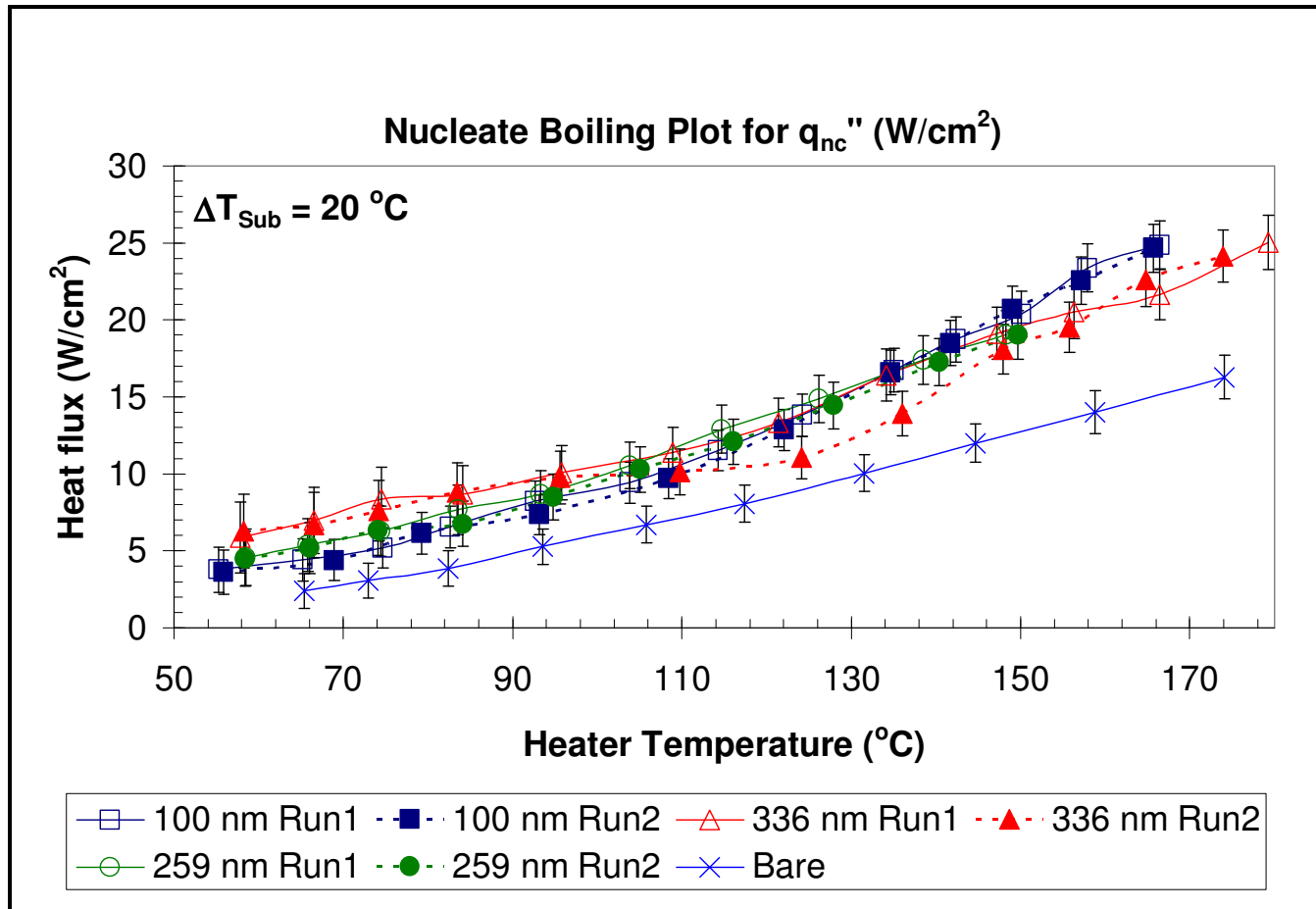
Fig. 26. Plots comparing the heat flux through the nano-patterned areas for the enhanced test surfaces (q_{nc}") with the heat flux through the bare test surface (q_b") under 20 °C sub-cooling condition for the nucleate boiling regime. Heat flux data is plotted against heater temperature (T_2).

4.5 Results - Set 2

The above results are reported with respect to the heater temperature that is directly measured using a thermocouple inserted in the copper block. The boiling curve is typically plotted between the wall heat flux (W/cm^2) and the wall superheat (°C). Thin-Film-Thermocouples (TFTs) are used to measure the wall temperature during pool boiling experiments on bare silicon surfaces [27, 31]. TFTs are fabricated on silicon test surfaces through a series of photolithography steps. Once fabricated, TFTs are packaged using a cold weld compound (J-B Weld, J-B Weld Co.). The next step is the calibration of the TFTs. TFT calibration is done using a standard k-type thermocouple in air which in-turn is calibrated in a constant temperature bath using a NIST thermometer. Experiments are then conducted under saturation condition from which the surface temperature data is obtained. The analysis of the experimental temperature data revealed that a there exists a piece-wise linear dependence of the wall temperature (T_w - °C) of bare silicon surface to the copper block surface temperature (T_{Cu} - °C). T_{Cu} is obtained for each steady-state by extrapolating the average temperatures from the thermocouple readings in each row of the copper block to its surface. The regimes are spilt in ranges of copper block temperatures. The T_w values are plotted against T_{Cu} over the different copper block temperature ranges and the linear relationship between the two for a given T_{Cu} range is given by

$$T_w = m{\cdot}T_{Cu} + c \tag{16}$$

where, m and c are constants.

Using the relationship between T_w and T_{Cu}, the values of m and c are found for the given T_{Cu} range. This can be done by plotting the values between T_w and T_{Cu} for a given range and fitting a linear trend-line to the curve. The values of m and c can be obtained from the corresponding trend-line equations. The value of wall temperature can then be recalculated using(16) for the experimental data used in the present study. The linear dependence is valid for both nucleate and film boiling. The wall superheat [or "$(\Delta T)_{wall}$"] is then given by

$$\left(\Delta T\right)_{Wall} = T_w - T_{Sat} \tag{17}$$

where T_{sat} is the saturation temperature of the test fluid used (for PF5060 $T_{sat} = 56$ °C). Pool boiling experiments are performed with two TFTs fabricated on the bare silicon surface. Using the data from these experiments, two sets of correlations are developed to obtain the wall temperature. The assistance provided by Vijaykumar Sathyamurthi (graduate student, Mechanical Engineering, Texas A&M University) in setting-up and running the TFT experiments and finally arriving at the correlations is greatly appreciated. Using the data from the two TFTs, the following correlations (shown in Table 1 and Table 2) are obtained.

Table 1. Correlations obtained from TFT1

Tcu (^{o}C)	Correlation set 1
56-74.81	$T_w = 0.2705*Tcu + 41.762$
74.82-82.91	$T_w = 0.1815*T_{Cu} + 48.426$
82.92-91.20	$T_w = 0.0976*T_{Cu} + 55.378$
91.21-100.69	$T_w = 0.1194*T_{Cu} + 53.393$
100.7-114.0	$T_w = 0.1283*Tcu + 52.498$
114.01-125.11	$T_w = 0.1178*T_{Cu} + 53.687$
125.12-136.99	$T_w = 0.1069*T_{Cu} + 55.049$
137-150.53	$T_w = 0.0759*T_{Cu} + 59.3$

Table 2. Correlations obtained from TFT2

Tcu (^{o}C)	Correlation set 2
56-74.81	$T_w = 0.2478*T_{Cu} + 43$
74.82-82.91	$T_w = 0.18*Tcu + 48.076$
82.92-91.20	$T_w = 0.1293*T_{Cu} + 52.281$
91.21-114	$T_w = 0.1074*T_{Cu} + 54.277$
114.01-150.53	$T_w = 0.0725*T_{Cu} + 58.255$

The final wall temperature is taken as the average of the temperatures calculated using each of the above correlations. The uncertainty in the estimated surface temperature is found to be ± 0.8 °C. Analysis of several experimental data reveals that the relationship between the copper block surface temperature and the wall temperatures measured is independent of the wall heat flux for saturated and sub-cooled experiments. While calculating the wall temperature (T_w) for some cases using the above correlations, the T_{Cu} may exceed the maximum T_{Cu} limit in the last correlation range in nucleate boiling or be lower than the minimum T_{Cu} limit in the first correlation in nucleate boiling. In

these cases, the final correlation and the first correlations are used to estimate T_w respectively.

4.5.1 Saturation condition results - set 2

Since the correlations are independent of the wall heat flux, the heat flux remains the same as in the first set of results (set 1). Fig. 27 shows the boiling curve for the heat flux through the test surface (q_w") under saturation condition. The overall trend is the same as in the first set of results with the same heat flux values. The film boiling regime does not show notable enhancement outside the limits of experimental uncertainty and thus is neglected while reporting results for q_n" and q_{nc}". Fig. 28 shows the nucleate boiling curve for q_w" alone for better clarity of results.

Fig. 29 and Fig. 30 show the boiling curve for q_n" and q_{nc}" under saturation condition. The trend in boiling is the same as in the previous set of results with the predicted heat fluxes (q_n" and q_{nc}") for the different enhanced surfaces tending to overlap with each other as they get closer to CHF. Also the relative enhancement with respect to the bare test surface is also shown.

Table 3. Heat flux at the CHF condition ($q_{b,CHF}$") for the bare silicon test surface under different sub-cooling conditions (ΔT_{Sub})

$(\Delta T)_{sub}$ (℃)	0	10	20
$q_{b,CHF}$" (W/cm^2)	10.87	13.57	16.28

Table 4. Wall superheat at the CHF condition $(\Delta T)_{wall,CHF}$ for the bare silicon test surface under different sub-cooling conditions (ΔT_{Sub})

$(\Delta T)_{Sub}$ (°C)	0	10	20
$(\Delta T)_{Wall,CHF}$ (°C)	13.56	14.51	15.68

Table 3 shows the heat flux at CHF condition $(q_{b,CHF}")$ for the bare silicon surface. Table 4 shows the wall superheat at CHF condition $(\Delta T)_{wall,CHF}$ for the bare silicon surface. Table 5 and Table 6 below show the percentage enhancement in the heat fluxes $(q_n")$ and $(q_{nc}")$ for the nano-finned surfaces compared to the bare test surface (under saturation condition). Table 7 shows the reduction in $(\Delta T)_{wall,CHF}$ (wall superheat at CHF condition) for the nano-finned surfaces relative to the bare test surface under saturation condition.

Table 5. Percentage enhancements in $q_{n,CHF}"$ for the nano-finned surfaces relative to the bare test surface under saturation condition

Run	Nano-finned surface		
	100 nm	259 nm	336 nm
1	111%	109%	119%
2	106%	123%	116%

Table 6. Percentage enhancements in $q_{nc,CHF}"$ for the nano-finned surfaces relative to the bare test surface under saturation condition

Run	Nano-finned surface		
	100 nm	259 nm	336 nm
1	97%	79%	100%
2	93%	91%	97%

Table 7. Increase in $(\Delta T)_{wall,CHF}$ for the nano-finned surfaces relative to the bare test surface under saturation condition

Run	Nano-finned surface		
	100 nm	259 nm	336 nm
1	-0.08 °C	-0.27 °C	0.24 °C
2	-0.04 °C	-0.30 °C	0.11 °C
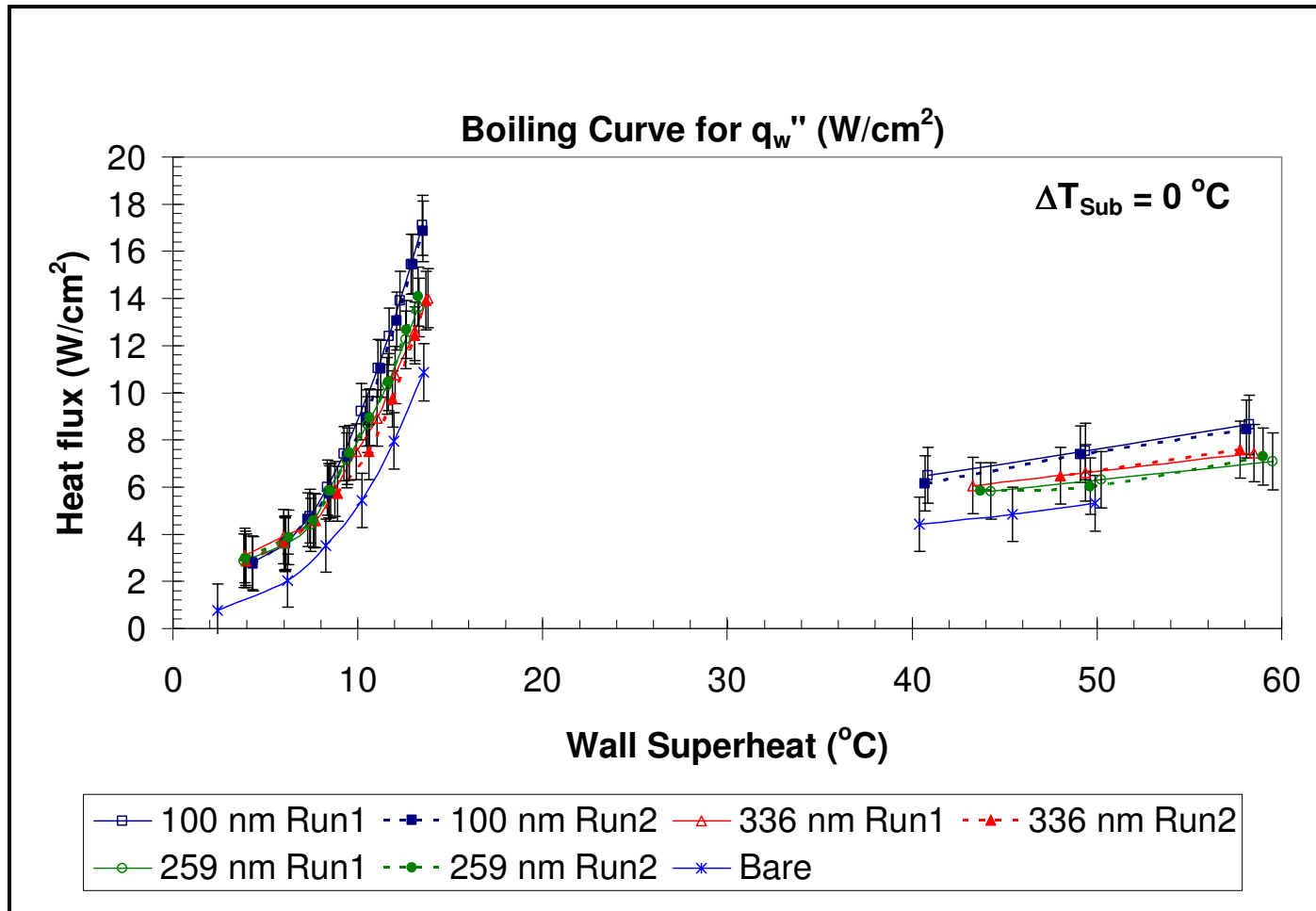
Fig. 27. Pool boiling curves comparing the heat flux through the enhanced test surfaces (q_w") with the heat flux through the bare test surface (q_b") under saturation condition.

Fig. 28. Nucleate pool boiling curves comparing the heat fluxes through the enhanced test surfaces (q_w'') with the heat flux through the bare test surface (q_b'') under saturation condition.

Fig. 29. Nucleate pool boiling curves comparing the heat flux through the nano-patterned plan areas for the enhanced test surfaces (q_w") with the heat flux through the bare test surface (q_b") under saturation condition.

Fig. 30. Nucleate pool boiling curves comparing the heat flux through the nano-patterned areas for the enhanced test surfaces (q_w") with the heat flux through the bare test surface (q_b") under saturation condition.

4.5.2 10 °C sub-cooling results - set 2

Fig. 31 shows the pool boiling curves for heat flux through the test surfaces (q_w") under 10 °C sub-cooling condition. The curve hardly shows any significant enhancement in the film boiling regime and thus the film boiling data is neglected while reporting results for (q_n") and (q_{nc}"). Since the nucleate boiling curves are plotted too close to each other, Fig. 32 shows the nucleate boiling curve for q_w" alone for better clarity. The overall trend in the boiling curves is similar to the first set of results (Set 1).

Fig. 33 and Fig. 34 show the nucleate pool boiling curve for q_n" and q_{nc}". Again the overall trend in the boiling curve is similar to the first set of results (Set 1). However the repeatability of the data is inferior to the data for the saturation case. The curves are also observed to overlap increasingly towards the CHF condition with an overall enhancement in CHF compared to the bare test surface.

Table 8 and Table 9 below summarizes the enhancement in $q_{n,CHF}$" and $q_{nc,CHF}$" for the nano-finned surfaces relative to the bare test surface for the different experimental runs in the 10 °C sub-cooling condition.

Table 8. Percentage enhancements in $q_{n,CHF}$" for the nano-finned surfaces relative to the bare test surface under 10 °C sub-cooling condition

Run	Nano-finned surface		
	100 nm	259 nm	336 nm
1	51%	27 %	53 %
2	65 %	65 %	71 %
3	-	53 %	73 %

Table 9. Percentage enhancements in $q_{nc,CHF}$" for the nano-finned surfaces relative to the bare test surface under 10 °C sub-cooling condition

Run	Nano-finned surface		
	100 nm	259 nm	336 nm
1	42 %	9 %	39 %
2	54 %	41 %	56 %
3	-	31 %	58 %

Table 10 below demonstrates the reduction in wall superheat for the nano-finned surfaces relative to the bare test surface for the different runs in 10 °C sub-cooling condition.

Table 10. Increase in $(\Delta T)_{wall,CHF}$ for the nano-finned surfaces relative to the bare test surface under 10 °C sub-cooling condition

Run	Nano-finned surface		
	100 nm	259 nm	336 nm
1	-0.22 °C	-0.89 °C	-0.60 °C
2	-0.25 °C	-1.01 °C	0.29 °C
3	-	-0.81 °C	-0.05 °C

Table 11 and Table 12 show the relative enhancements in q_n" and $q_{n,CHF}$" for the nano-finned surfaces and the reduction in wall superheat under 10 °C sub-cooling condition relative to the average of the values of the saturation condition.

Table 11. Percentage enhancement in $q_{n,CHF}$" and $q_{nc,CHF}$" of the nano-finned surfaces under 10 °C sub-cooling condition relative to the saturation condition

Nano-finned surface	100 nm	259 nm	336 nm
% enhancement in $q_{n,CHF}$", $q_{nc,CHF}$"	-5 %	-14 %	-5 %

Table 12. Increase in $(\Delta T)_{wall,CHF}$ for the nano-finned surfaces under 10 °C sub-cooling condition relative to the saturation condition

Nano-finned surface	100 nm	259 nm	336 nm
Increase in $(\Delta T)_{wall,CHF}$	0.78 °C	0.33 °C	0.66 °C
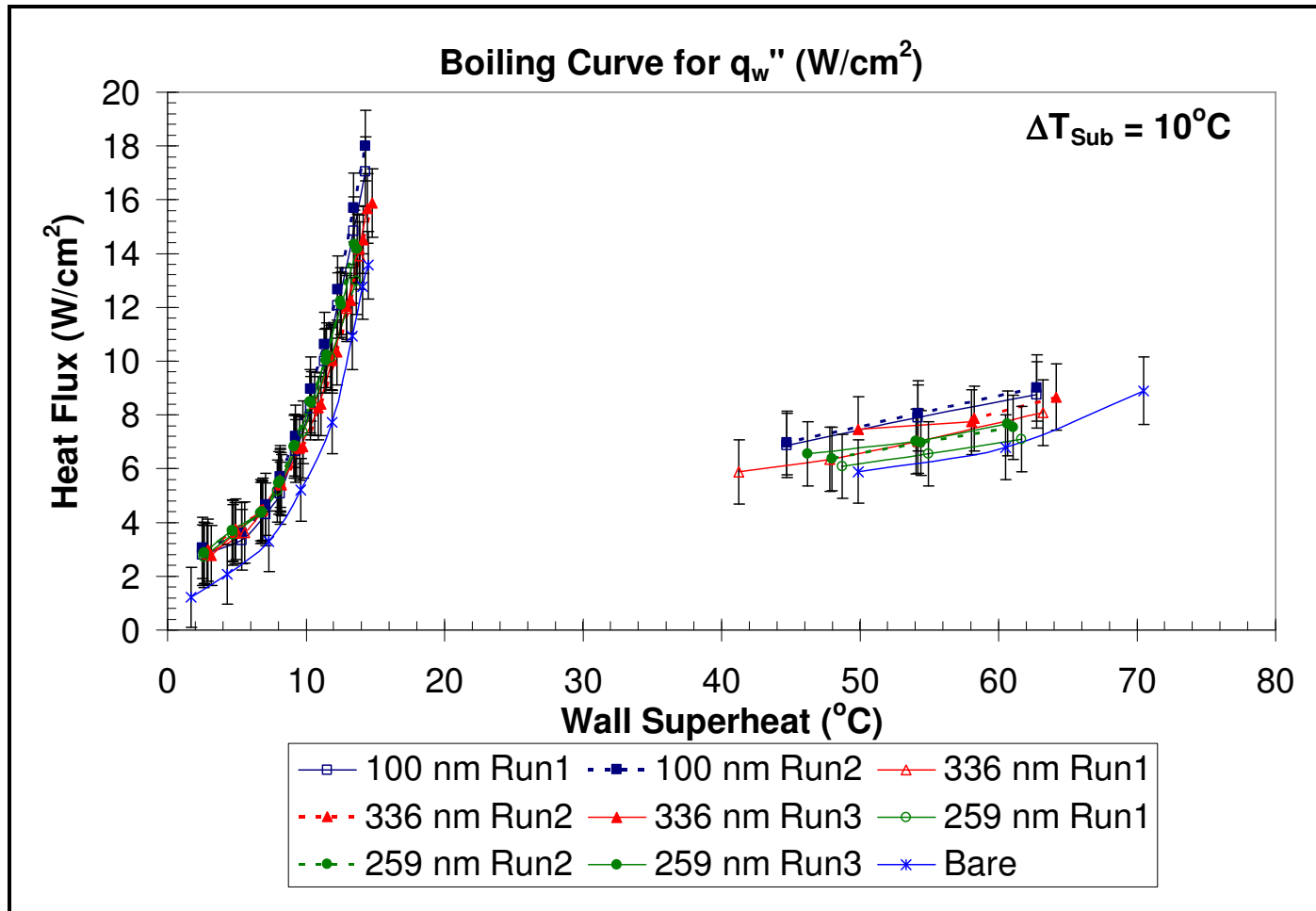
Fig. 31. Pool boiling curves comparing the heat flux through the enhanced test surfaces (q_w") with the heat flux through the bare test surface (q_b") under 10 °C sub-cooling condition.
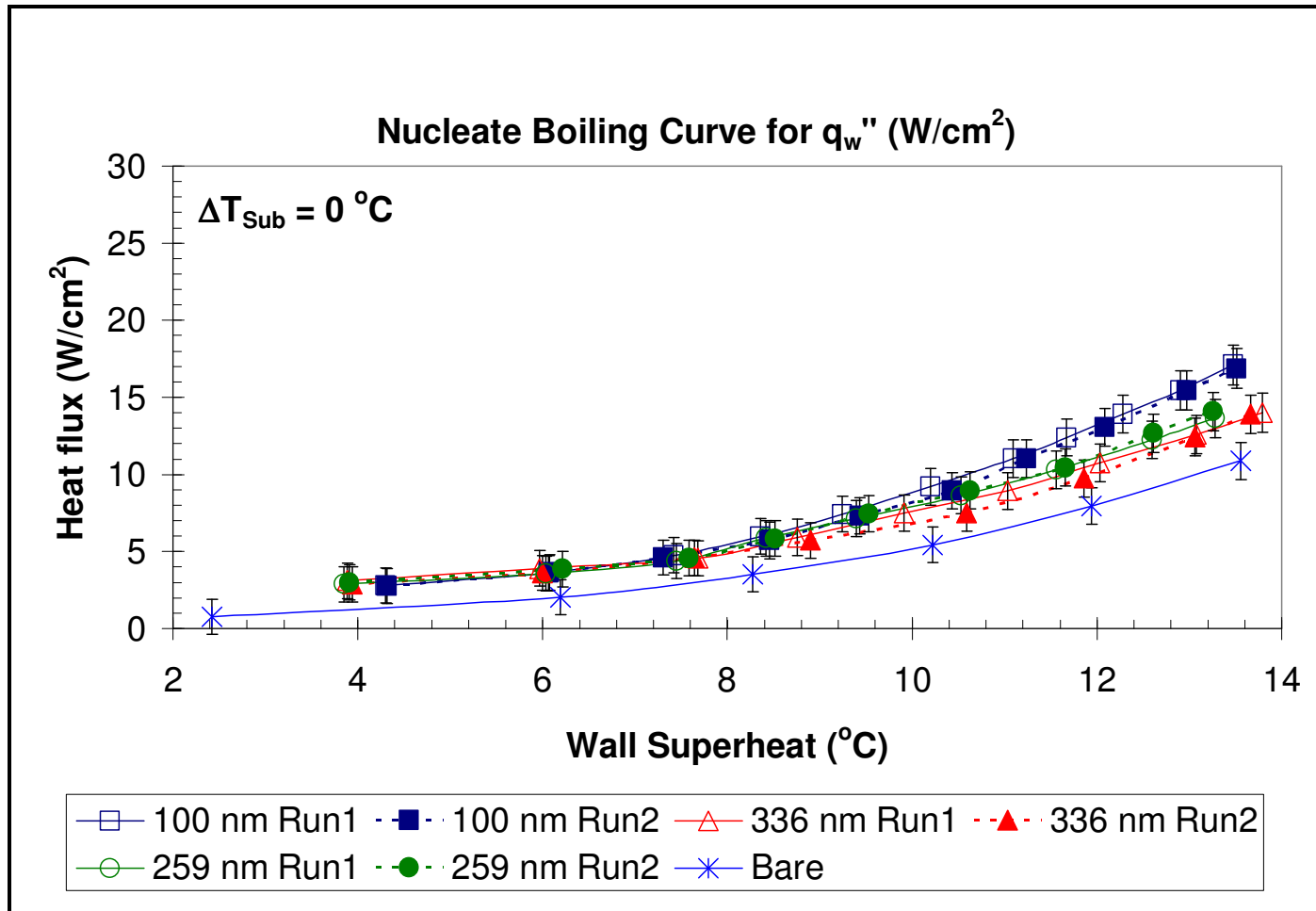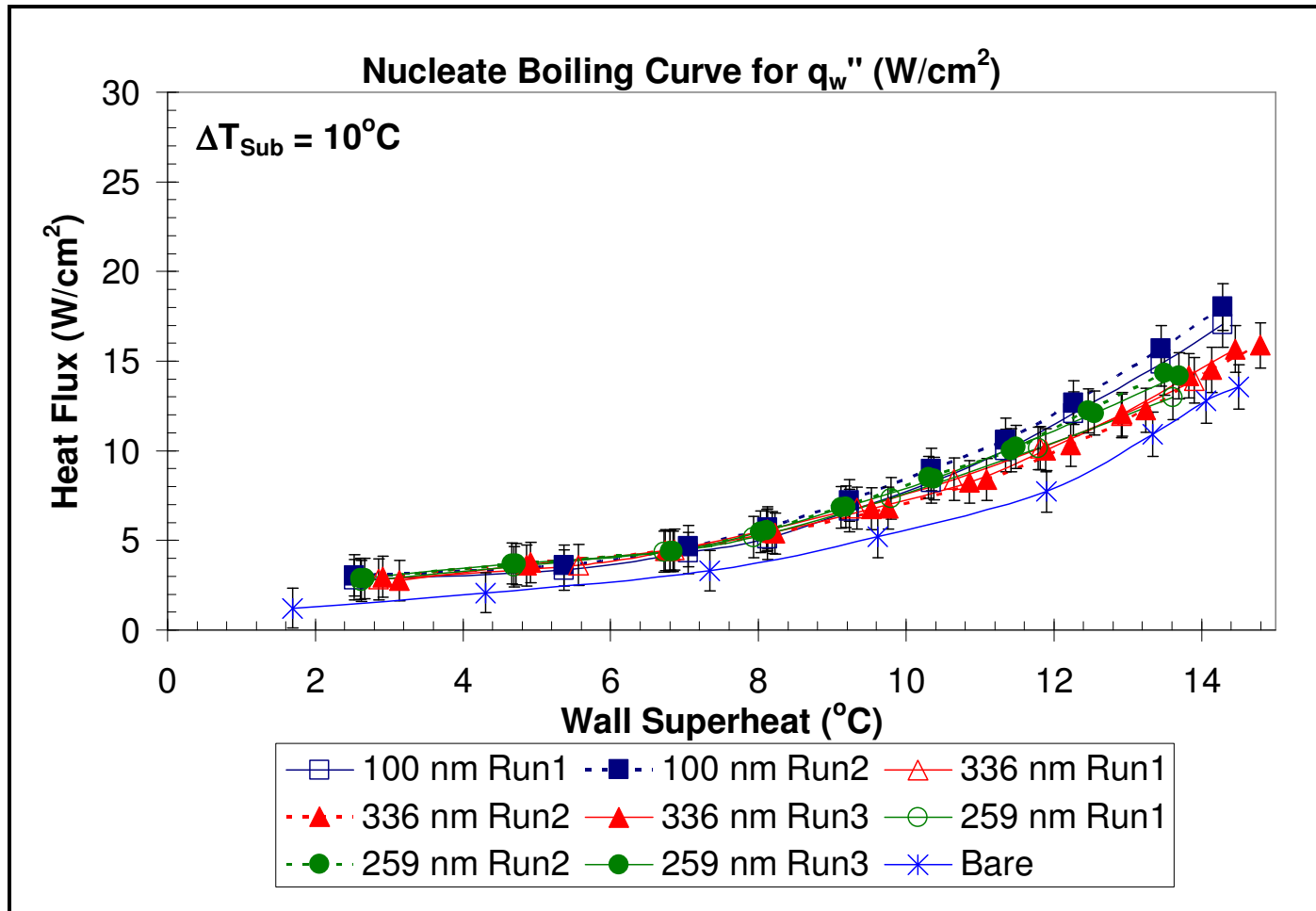
Fig. 32. Nucleate pool boiling curves comparing the heat fluxes through the enhanced test surfaces (q_w") with the heat flux through the bare test surface (q_b") under 10 °C sub-cooling condition.
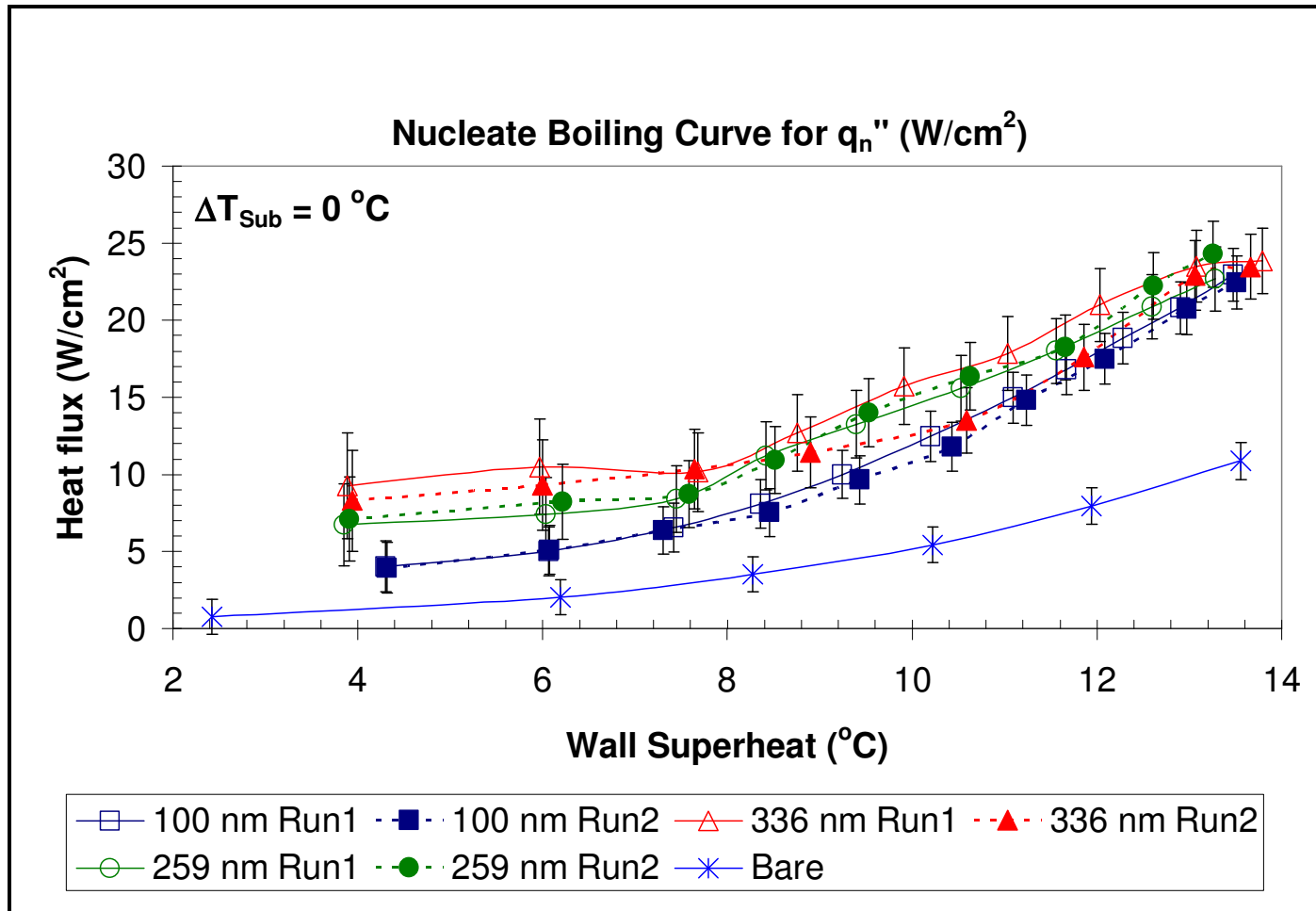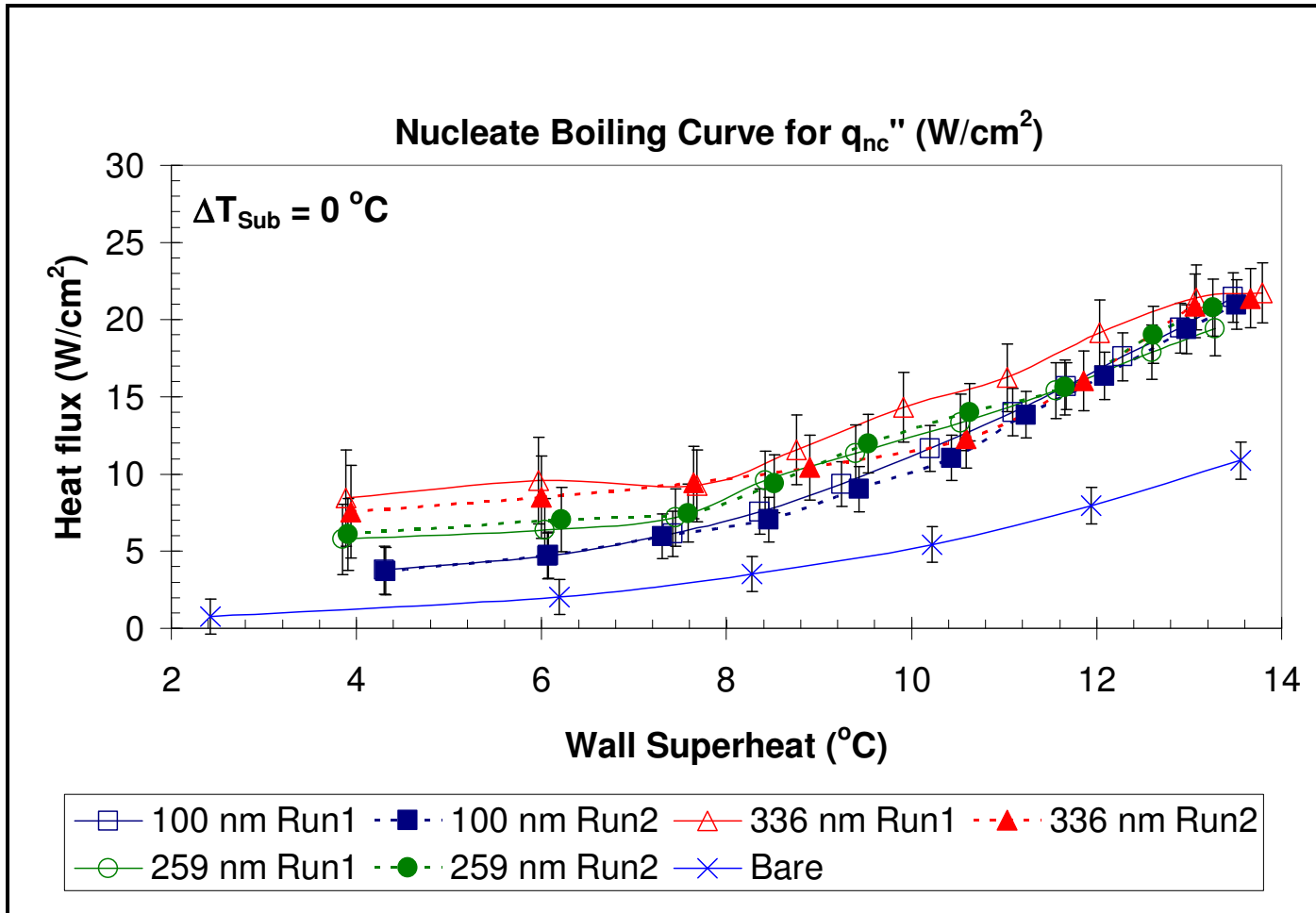
Fig. 33. Nucleate pool boiling curves comparing the heat flux through the nano-patterned plan areas for the enhanced test surfaces (q_w") with the heat flux through the bare test surface (q_b") under 10 °C sub-cooling condition.

Fig. 34. Nucleate pool boiling curves comparing the heat flux through the nano-patterned areas for the enhanced test surfaces (q_w") with the heat flux through the bare test surface (q_b") under 10 °C sub-cooling condition.

*4.5.3 20 °C Sub-cooling results*

Fig. 35 shows the pool boiling curves for q_w" under 20 °C sub-cooling and the results are compared with that of the bare test surface. The overall trend is the same as in the first set of results (set1) with no significant enhancement in the nucleate boiling regime. Fig. 36, Fig. 37 and Fig. 38 show the nucleate pool boiling curves for the different test surfaces. The results are reported for q_w", q_n" and q_{nc}". The trend again goes to show that the boiling curves overlap with each other with increase in heat flux towards the CHF condition as in the first set of results (set 1)

Table 13 and Table 14 show the percentage enhancements in $q_{n,CHF}$" and $q_{nc,CHF}$" for the nano-finned surfaces under the 20 °C sub-cooling condition relative to the bare test surface.

Table 13. Percentage enhancements in $q_{n,CHF}$" for the nano-finned surfaces relative to the bare test surface under 20 °C sub-cooling condition

Run	Nano-finned surface		
	100 nm	259 nm	336 nm
1	63 %	36 %	69 %
2	62 %	36 %	63 %

Table 14. Percentage enhancements in $q_{nc,CHF}$" for the nano-finned surfaces relative to the bare test surface under 20 °C sub-cooling condition

Run	Nano-finned surface		
	100 nm	259 nm	336 nm
1	53 %	17 %	54 %
2	51 %	17 %	48 %

Table 15 shows the reduction in wall superheat for the nano-finned surfaces under 20 °C

sub-cooling condition experiments relative to that of the bare test surfaces.

Table 15. Increase in $(\Delta T)_{wall,CHF}$ for the nano-finned surfaces relative to the bare test surface under 20 °C sub-cooling condition

Run	Nano-finned surface		
	100 nm	259 nm	336 nm
1	-0.55 °C	-1.91 °C	0.41 °C
2	-0.61 °C	-1.80 °C	0.00 °C

Table 16 and Table 17 show the relative enhancement in the $q_{n,CHF}$" and $q_{nc,CHF}$" and the

reduction in wall superheat for the nano-finned surfaces relative to the average values in

the saturation condition experiments.

Table 16. Percentage enhancement in $q_{n,CHF}$'' and $q_{nc,CHF}$'' of the nano-finned surfaces under 20 °C sub-cooling condition relative to the saturation condition

Nano-finned surface	100 nm	259 nm	336 nm
% enhancement in $q_{n,CHF}$", $q_{nc,CHF}$"	17%	-5%	14%

Table 17. Increase in $(\Delta T)_{wall,CHF}$ for the nano-finned surfaces under 20 °C sub-cooling condition relative to the saturation condition

Nano-finned surface	100 nm	259 nm	336 nm
Increase in $(\Delta T)_{wall,CHF}$	1.60 °C	0.56 °C	2.15 °C
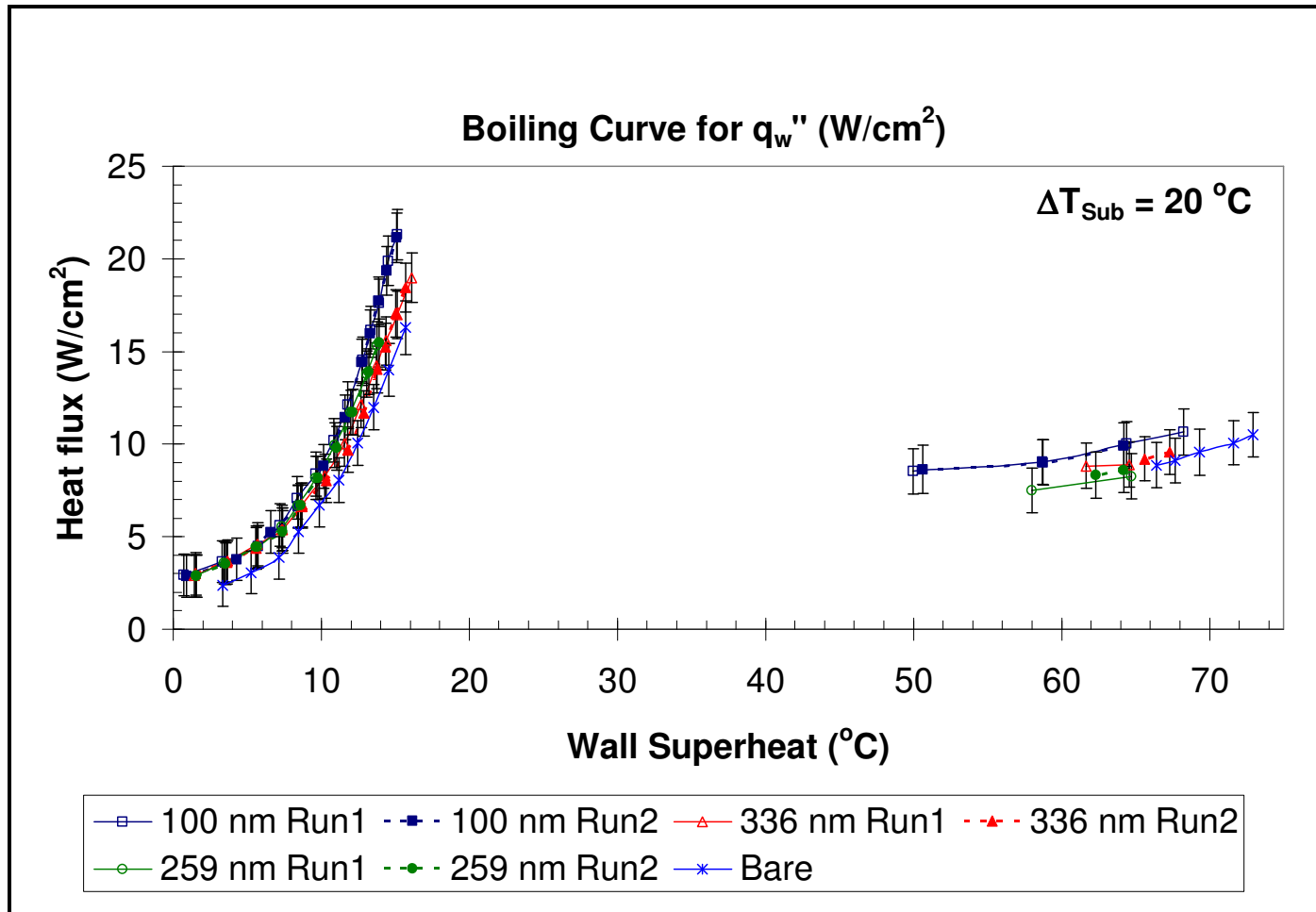
Fig. 35. Pool boiling curves comparing the heat flux through the enhanced test surfaces (q$_w$") with the heat flux through the bare test surface (q$_b$") under 20 °C sub-cooling condition.
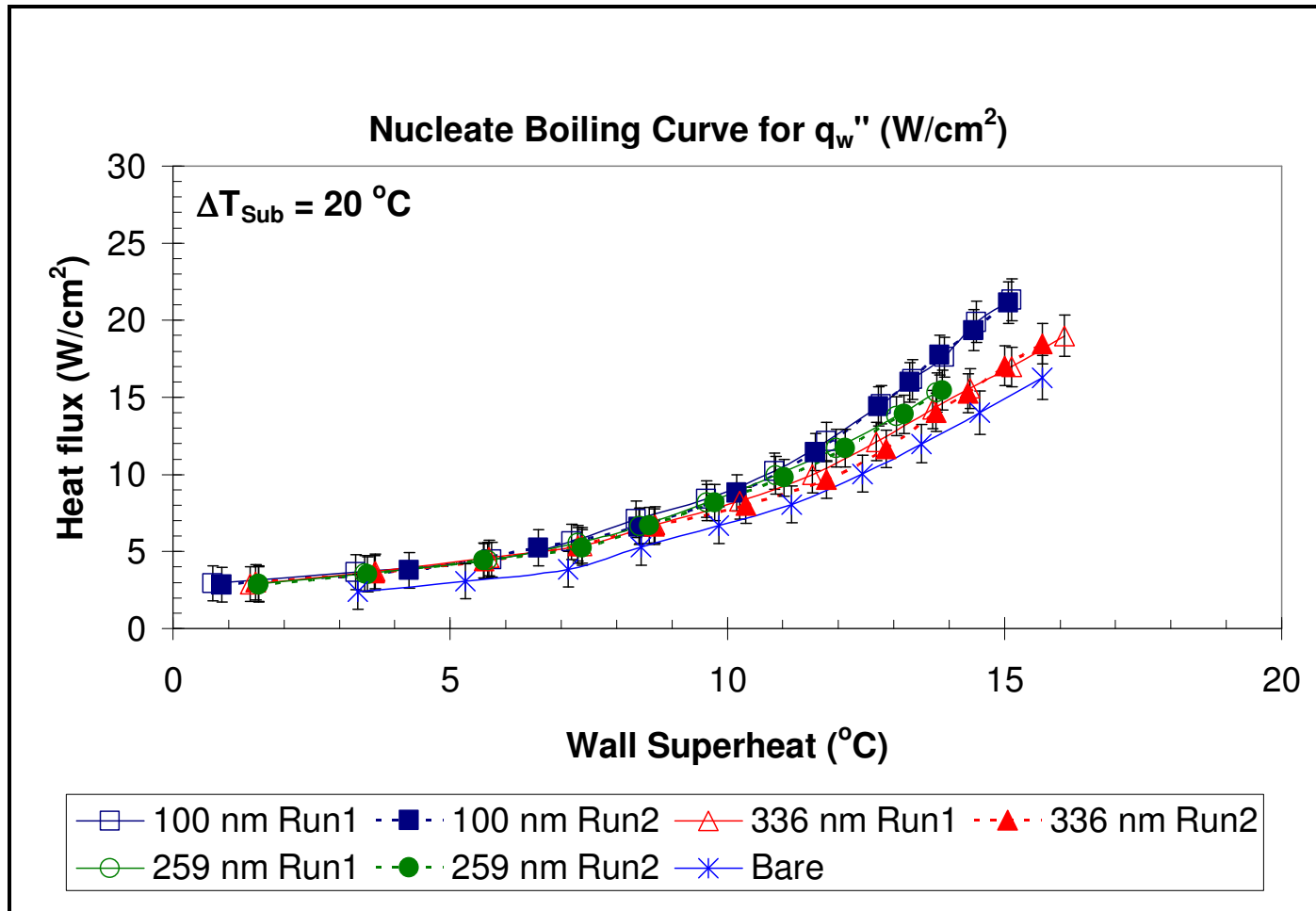
Fig. 36. Nucleate pool boiling curves comparing the heat fluxes through the enhanced test surfaces (q_w") with the heat flux through the bare test surface (q_b") under 20 °C sub-cooling condition.
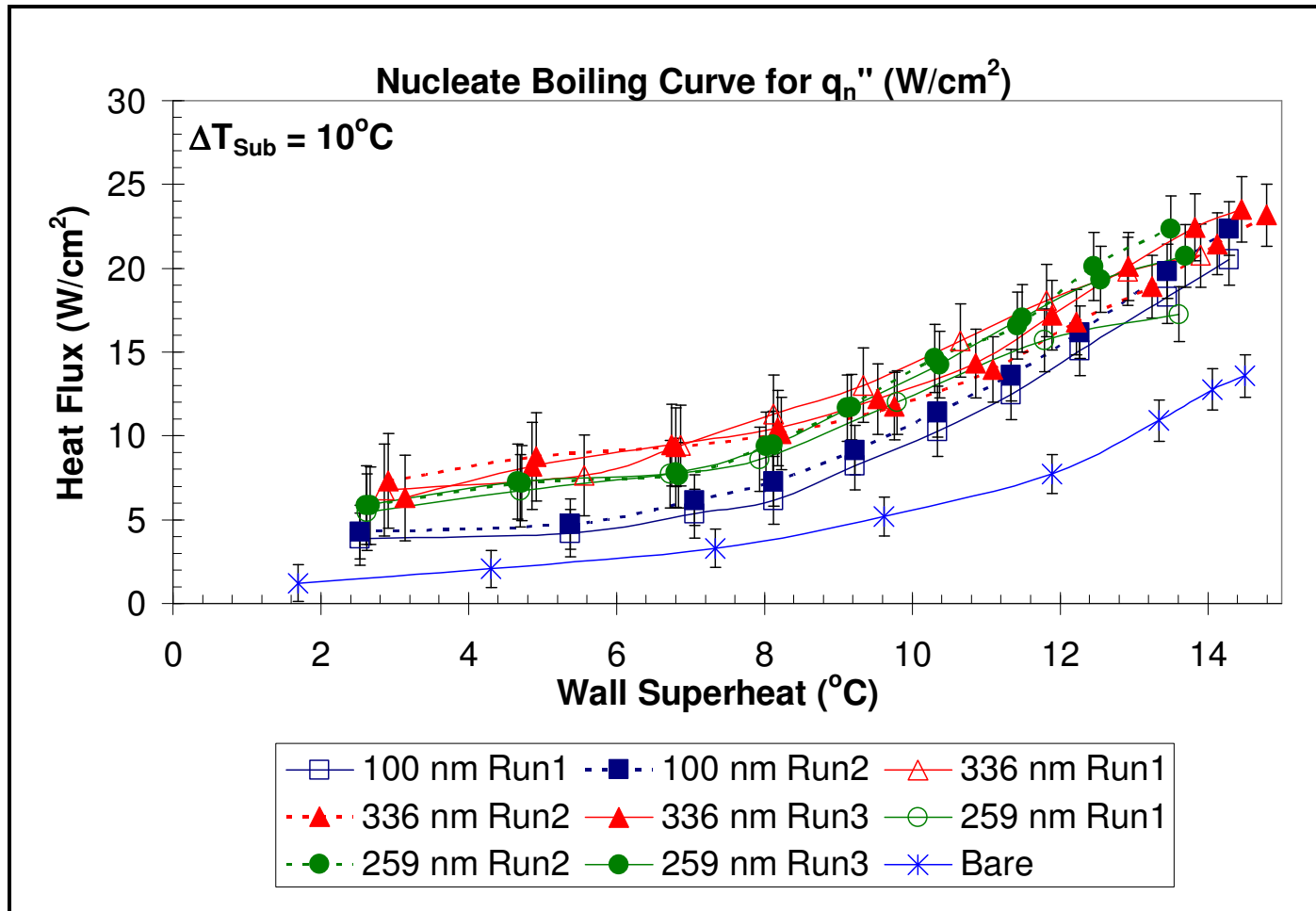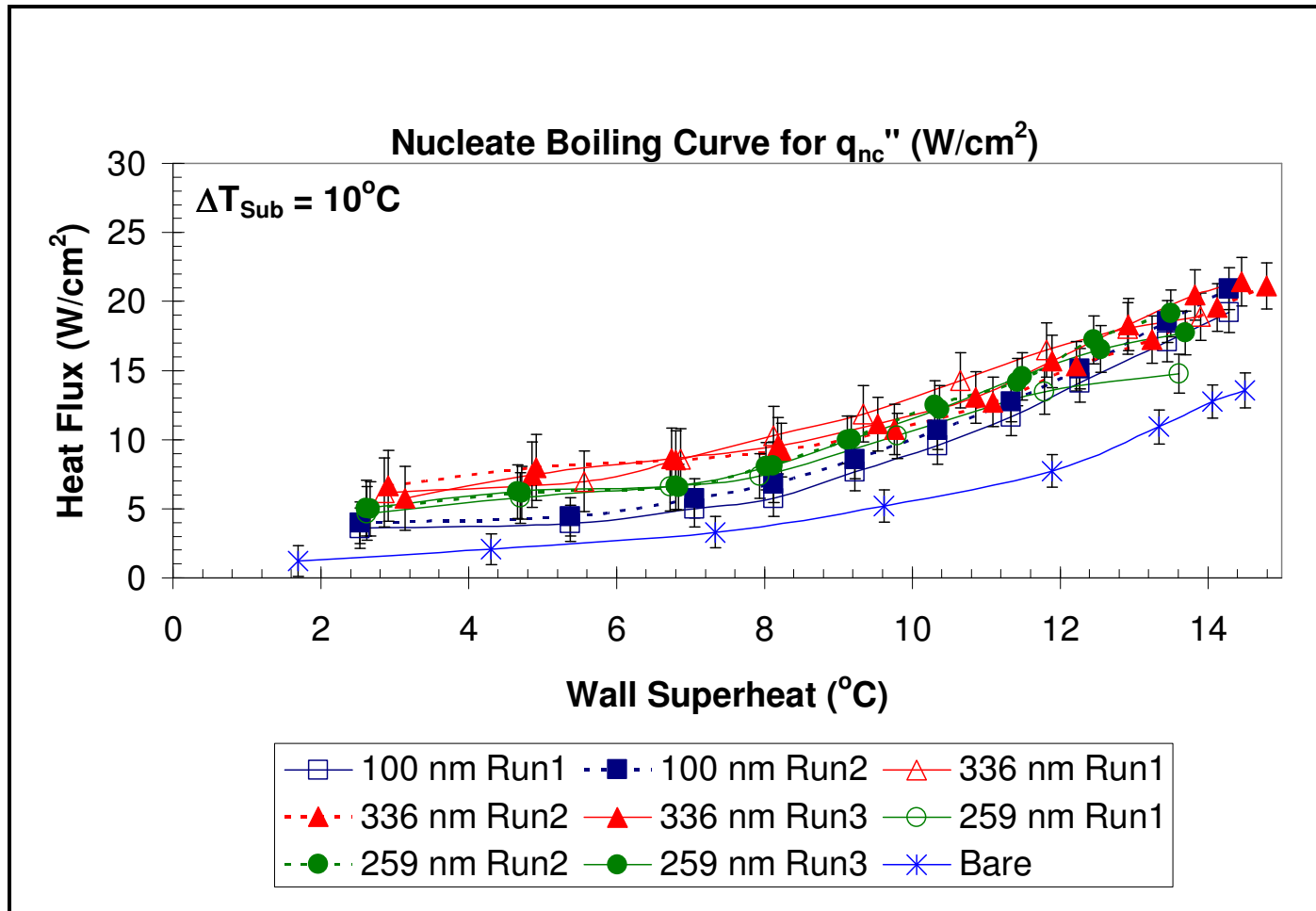
Fig. 37. Nucleate pool boiling curves comparing the heat flux through the nano-patterned plan areas for the enhanced test surfaces (q_w'') with the heat flux through the bare test surface (q_b'') under 20 °C sub-cooling condition.

Fig. Error! Unknown switch argument.**. Nucleate pool boiling curves comparing the heat flux through the nano-patterned areas for the enhanced test surfaces (q_w") with the heat flux through the bare test surface (q_b") under 10 °C sub-cooling condition.**

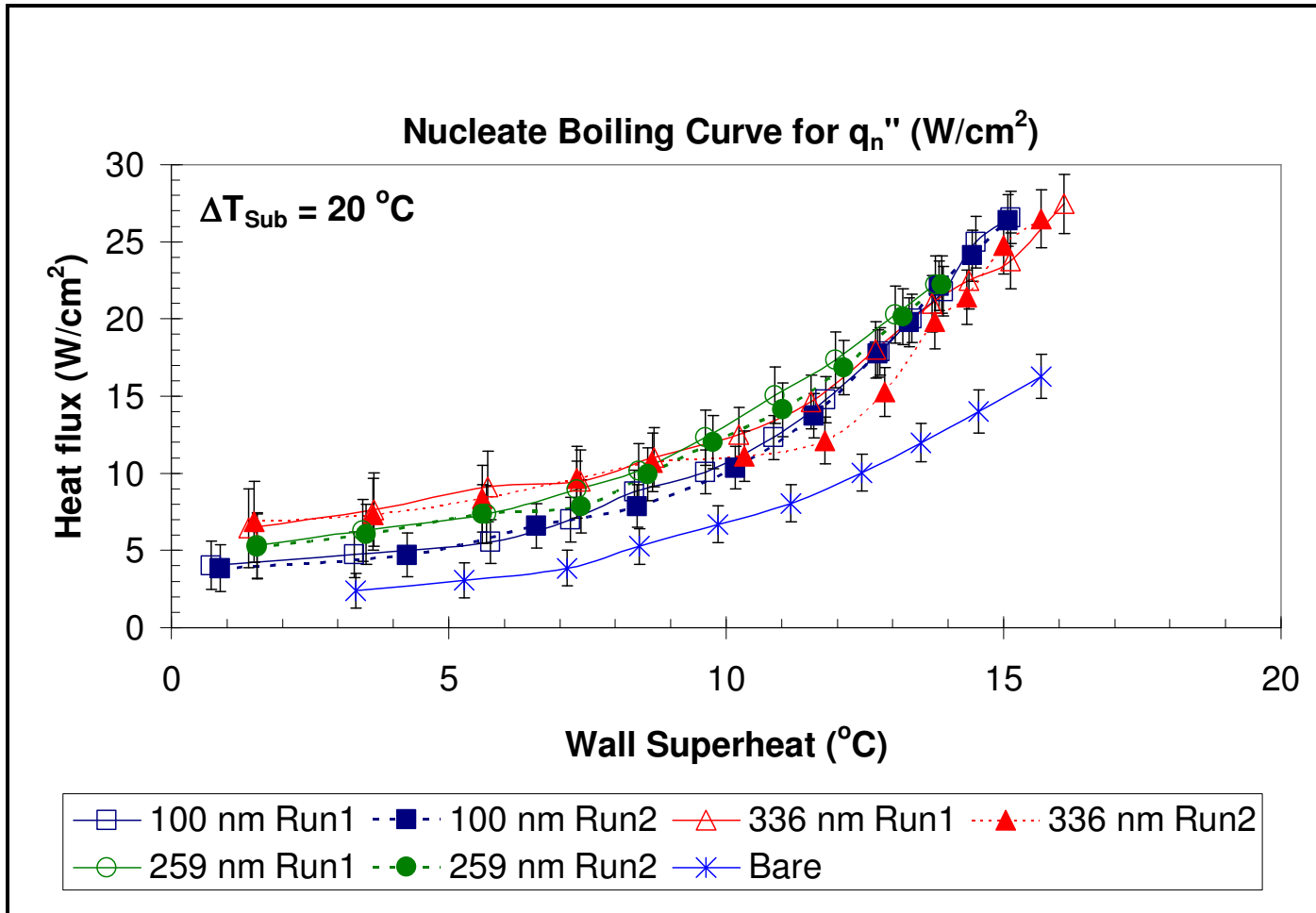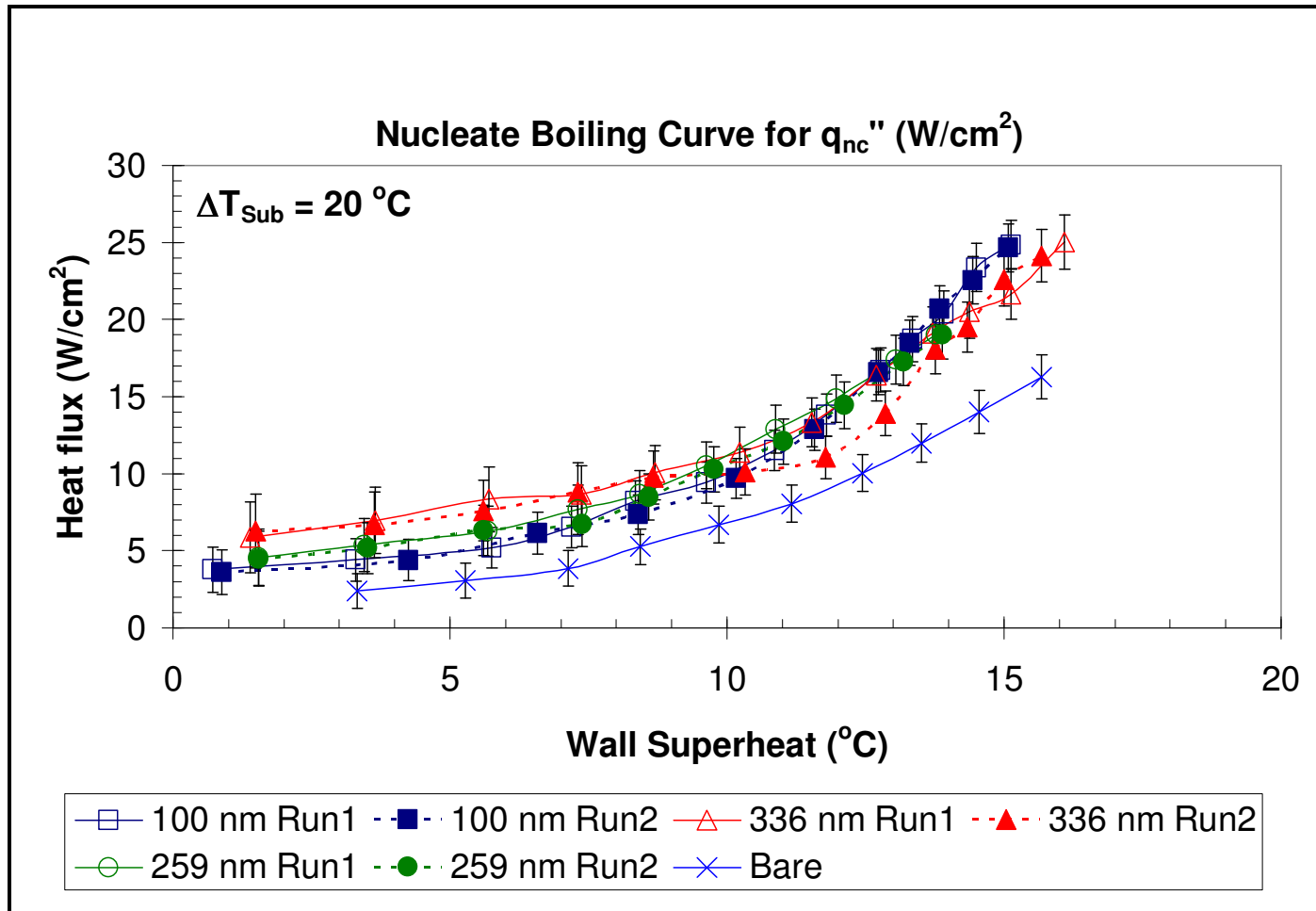**Fig. 39. Digital photograph showing pool boiling on a bare test surface under 20 °C sub-cooling condition very close to CHF**

Fig. 40. Digital photograph showing pool boiling on the *"336 nm"* test surface under 20 °C sub-cooling condition very close to CHF

Fig. 39 shows a digital image taken during the boiling of PF5060 under 20 °C sub-cooling condition on a bare test surface. The image was taken just before the system reached CHF. Fig. 40 shows a similar image taken during boiling on the *"336 nm"* test surface, again under 20 °C sub-cooling conditions and very close to CHF. A comparison between the two photographs shows that more bubble nucleation is occurring for the *"336 nm"* test surface compared to the bare test surface. This shows that there is an increase in the number of active nucleation sites for the enhanced test surface.

4.5 Contact angle variation

It is known that the contact angle of the working liquid on the boiling surface has an influence on the boiling heat transfer. Large temperature at boiling incipience that occurs with the use of highly wetting fluoroinerts is of major concern in electronic chip cooling applications [9, 32]. The receding dynamic contact angle is shown to have an effect on the CHF as well [33]. Thus the liquid-surface interaction is of paramount importance while understanding the transport processes in boiling. Literature has shown that the physical properties of the surface influence the wettability. In the 1930s, the effectiveness of the water-proofing material for fabrics was of concern. In 1936, Wenzel [34] found that, contrary to the usual notion, the wettability of a material depended also on the physical properties of the material and not only on the interfacial tension. He found that the tendency of the coatings that cause granular deposits rather than smooth deposits, helped increase the contact angle and decrease wettability. Cassie and Baxter [35] then extended this analysis to porous surfaces. They derived formulae for contact angles and found that they had good conformity to experimental observations. Recently,

Krupenkin et al. [36] fabricated five chemically identical test surfaces with varying roughness. They found that the cosine of the contact angle had a linear dependence on the roughness for a liquid with the highest surface tension. On the other hand, the dependence was non-linear for liquids with low surface tension. This was contradictory to the equations originally developed by Wenzel [34].

In the present study, the wettability of selected test surfaces fabricated using SFIL are studied with de-ionized water and the test fluid (PF5060) used for experimentation. The contact angle measurements were done using a contact angle goniometer at the Texas Transportation Institute laboratory (Texas A&M University). The test surfaces are initially spray-cleaned with isopropyl alcohol and acetone prior to loading on the goniometer. The sample is then loaded on the sample holder. The syringe on the goniometer is filled with either de-ionized water or PF5060 and the measurements are taken. The results reported in this study are for de-ionized water only since it is more stable than PF5060. It also forms a high, easily observable contact angle on most materials. PF5060 on the other hand is highly volatile and tends to evaporate before a reliable measurement could be made. Once the drop is dispensed on the surface, an initial live video image is obtained and the camera focus is adjusted for clarity. Subsequent to adjusting the image quality, a snapshot of the image is obtained using which the software calculates the contact angle.

Two approaches were undertaken for measuring the contact angle. First approach was the sessile drop method where the drop of liquid was dispensed on the test surface and made to sit on it. Dispensing is done slowly to ensure that the kinetic energy does not spread it over the surface and alter the reading. Fig. 41 shows an example of a sessile drop on a smooth silicon surface.
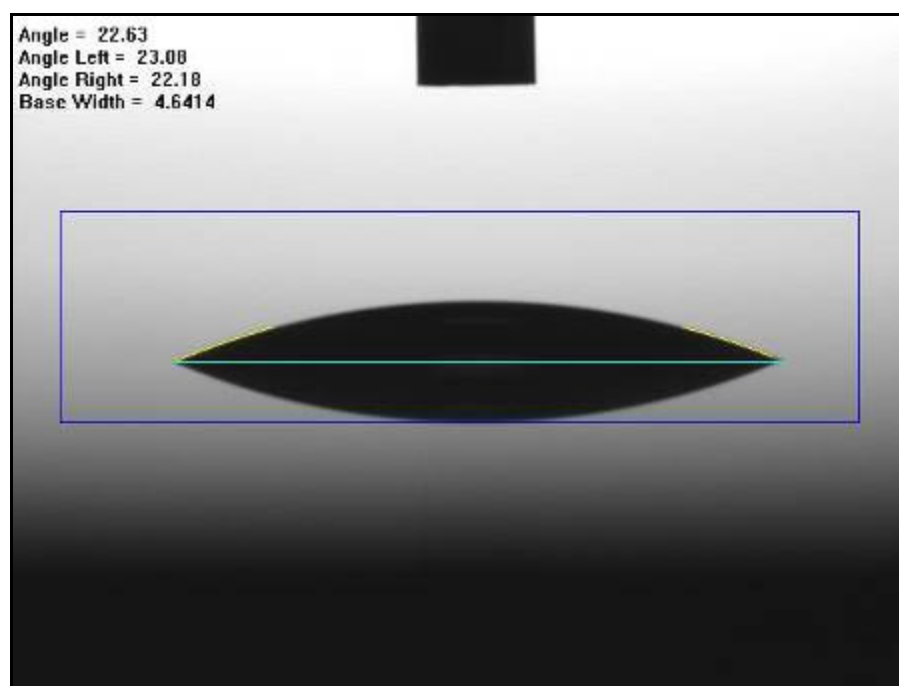
Fig. 41. Sessile droplet on a smooth silicon surface

The second method used was the captive needle/captive drop approach. Here the dispensing needle is brought very close to the surface and the drop is dispensed in contact with both the needle and the surface. Fig. 42 shows an example of a captive drop held between the dispensing needle and a smooth silicon surface. The average of four to six measurements is then reported as the contact angle for each case. The standard

deviation of the measurements is then plotted as the error in the contact angle measurement.
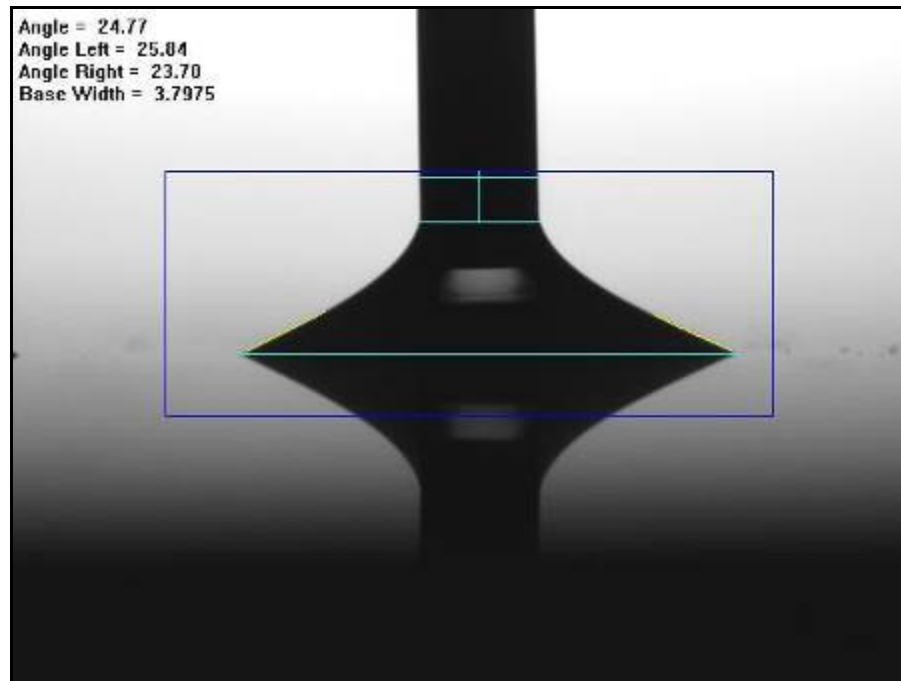
Fig. 42. Captive droplet held between the dispensing needle and the silicon test surface

The fresh test surfaces that were used are denoted as *"Bare"*, *"13 nm"*, *"100 nm"*, *"259 nm"*, and *"600 nm"*. The *"100 nm"* and the *"259 nm"* test surfaces are similar to the ones used for boiling experiments. The *"13 nm"* test surface was also fabricated using SFIL followed by dry RIE (Reactive Ion Etching) as in the *"100 nm"* case. The *"600 nm"* test surface was fabricated using SFIL followed by DRIE (Deep Reactive Ion Etching) as in the *"259 nm"* case. The test surfaces *"13 nm"* and *"600 nm"* were not used on the boiling setup because of very poor coverage with nano-fins. Fig. 43 and Fig. 44 show SEM images of the *"600 nm"* test surface in two different magnification levels.
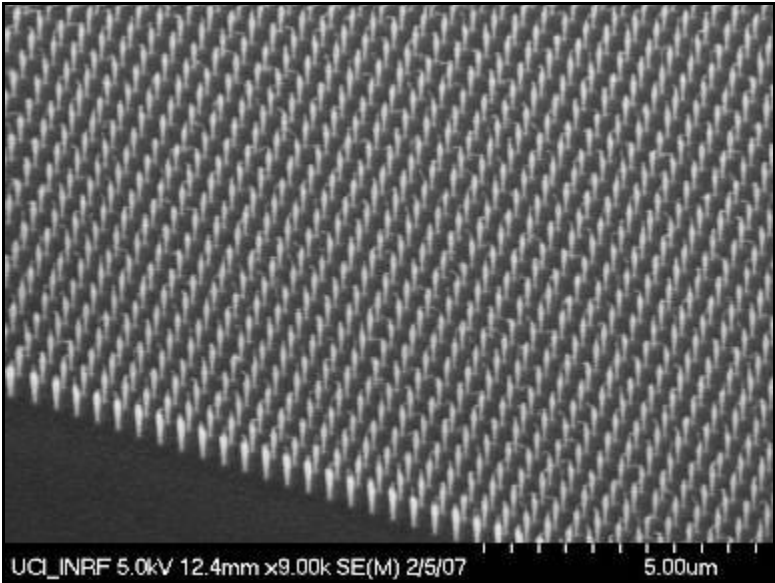
Fig. 43. *"600 nm"* test surface*:* Scanning Electron Microscope (SEM) image showing an array of 600 nm tall nano-fins fabricated on the *"600 nm"* test surface using Step and Flash Imprint Lithography (SFIL) followed by Deep Reactive Ion Etching (DRIE)
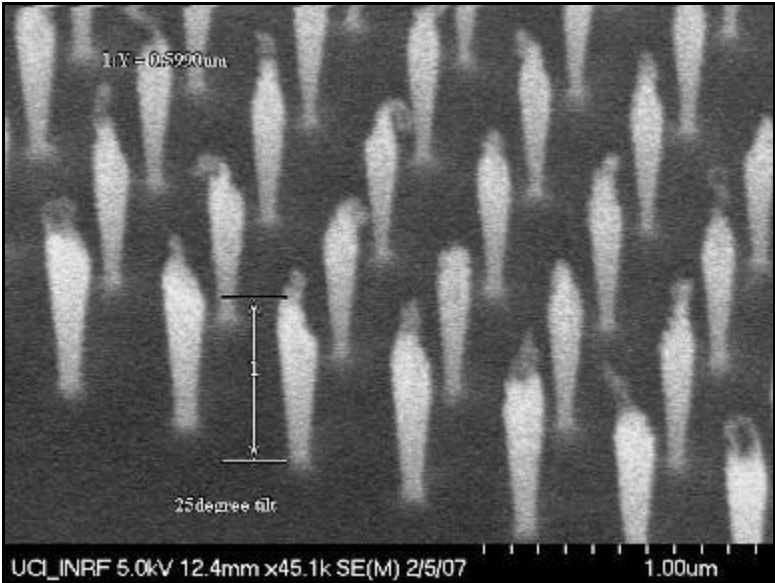
Fig. 44. *"600 nm"* test surface*:* SEM image showing the measured height of a nano-fin on the silicon test surface.

The variation of contact angle with the nano-fin height for fresh test surfaces (test surfaces not use on the pool boiling set-up) is shown in Fig. 45. It is clear that there is a variation of contact angle with the height of the pillars even for heights as low as 13 nm. There seems to be no linear dependence of contact angle on the height of the fins.
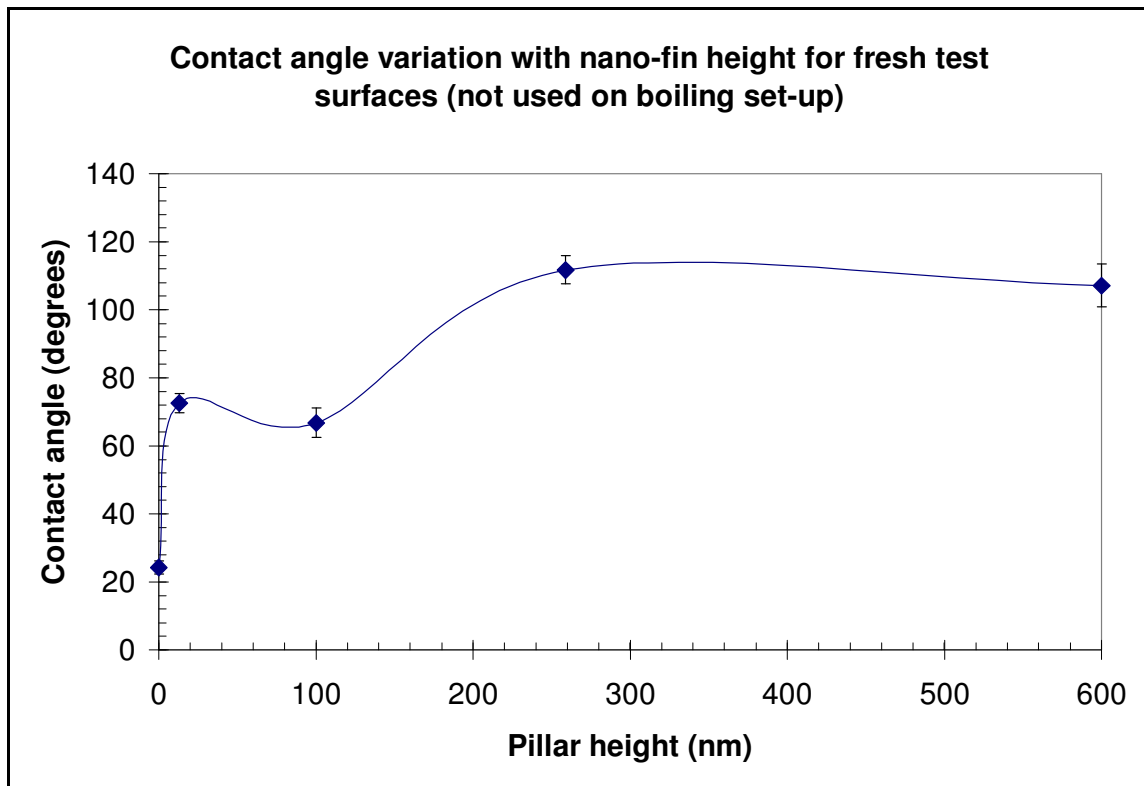
Fig. 45. Variation of contact angle of de-ionized water on fresh silicon test surfaces with varying height of the nano-fins.

Fig. 46 shows the variation of contact angle with nano-fin height for the *"100 nm"* and the *"336 nm"* test surfaces that were used on the pool boiling set-up. The results show that the contact angle for the *"100 nm"* test surface increased from about 67 ° to 107 ° after its use in the pool boiling set-up. In addition, there is hardly any variation in contact

angle in spite of the variation in height between the *"100 nm"* and the *"336 nm"* test surfaces.
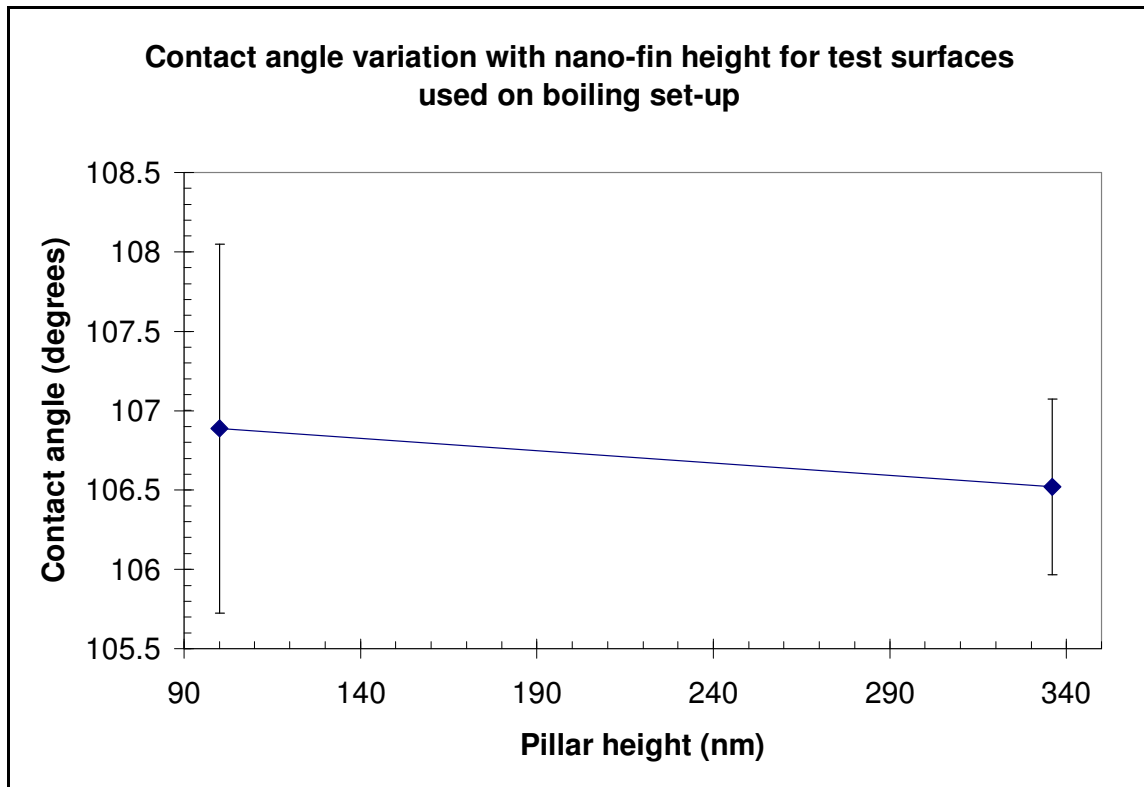
Fig. 46. Variation of contact angle of de-ionized water on silicon test surfaces used in boiling experiments with varying height of the nano-fins.

Two observations are thus apparent from the contact angle measurements on fresh and test surfaces used for pool boiling experiments. First, there is variation of contact angle with the height of the nano-fins with no specific trend. Second, the contact angle that de-ionized water makes with the test surface also depends on whether the test surface has been used for the pool boiling experiments. Surfaces that have been tested show very similar contact angles with de-ionized water.

4.6 Discussion of results

The results for the nano-structured test surfaces under different levels of sub-cooling show that there is an interesting interaction between the different phases during boiling. Upon nucleation from a cavity, the vapor bubble grows over the nano-fins as shown in Fig. 47 below.
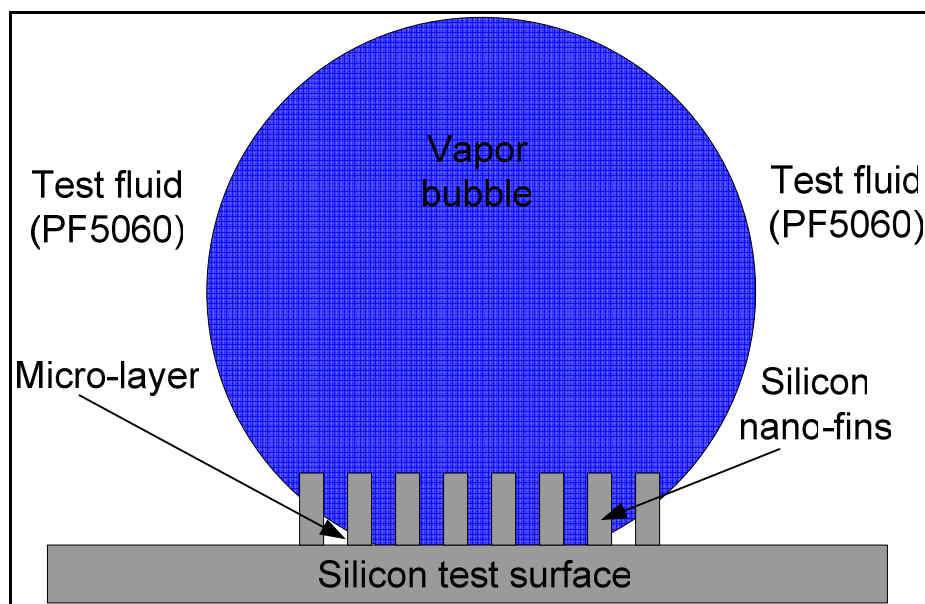
Fig. 47. Growing vapor bubble on a silicon test surface with nano-fins (figure not to scale)

Derjaguin and Zorin [37] suggested that the interfacial resistance to mass transfer allows the existence of a very thin film on the solid surface thus hindering the flow of evaporated liquid. Beyond this film thickness, the thin-film is capable of evaporating and enhancing the heat transfer. Wayner et al. [38] studied the interline heat transfer characteristics of an evaporating film. The study was done considering non-polar wetting fluids on solid surfaces. They define the *"interline"* as the junction between the vapor,

adsorbed non-evaporating thin film and adsorbed evaporating thin film. In the non-evaporating region, the film is kept intact through the Van Der Waals dispersion forces between the solid surface and the liquid film. On the other hand, as the film gets tapered, its thickness increases and at one point the thickness is sufficient to allow evaporation. The interline is thus the junction between the solid surface, the evaporating segment of the film, the non-evaporating segment of the film and the vapor layer. They found that the heat transfer coefficient changes from a value of zero at the interface to a value of liquid-vapor interfacial heat transfer coefficient at distances as short as 300 nm from the interface.
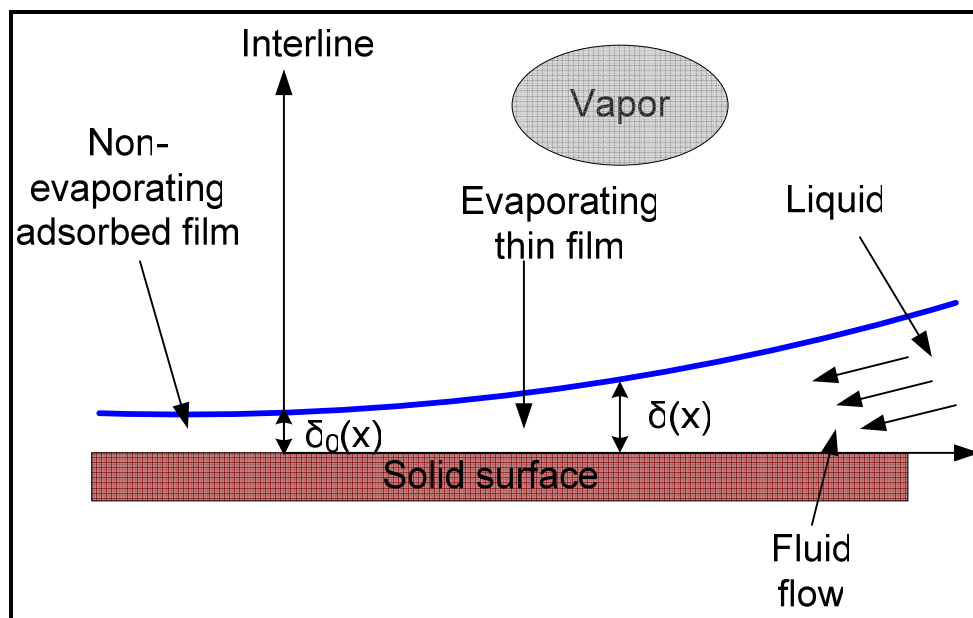
Fig. 48. Schematic diagram showing the interline junction [38] (figure not to scale).

They then further corrected the model to include the effect of conductivity of the solid in contact [39] since the above study was based on constant liquid-vapor interfacial

temperatures. They found that the initial portion of the evaporating thin film (after the interline) follows the constant temperature model until thermal resistance limits the heat flux to a constant value with a small increase in film thickness. Nevertheless, it was found that the interline region has a tremendous potential to enhance the phase-change heat transfer if exploited properly.

For a possible explanation to the heat transfer processes occurring in the present study, it is important to consider the thickness of the film (δ_0) at the interline region (See Fig. 48). Table 18 below shows some of the thin film thickness values reported in the literature.

Table 18. Interline thickness reported in literature

Literature Source	Details	Film thickness at interline
Carey[40]	CCl_4 on glass	8 A (or 0.8 nm)
Wayner et.al[38]	Non-polar wetting fluid on smooth solid	50 A (or 5 nm)
Catton et. al[41]	Partially submerged inclined copper plate in a stationary fluid	100 nm (at 0 ° inclination)
Stephan et al.[42]	Aluminium/ammonia heat pipe	10 nm
Dasgupta et al.[43]	Heptane on silicon substrate with power-controlled evaporation	15 nm (0 W) to 4.8 nm (2W)

The disparities in the literature data shows that the characteristics of the interline region is complex and may be specific to the given liquid and solid mediums interacting along with other parameters such as solid surface inclination [41] and the use of power control for evaporation [43]. Even though a number of notable studies have been undertaken in

this field [38, 39, 41, 44-46], it is difficult to exactly predict the point of maximum heat transfer in the interline region in spite of its widely accepted potential.
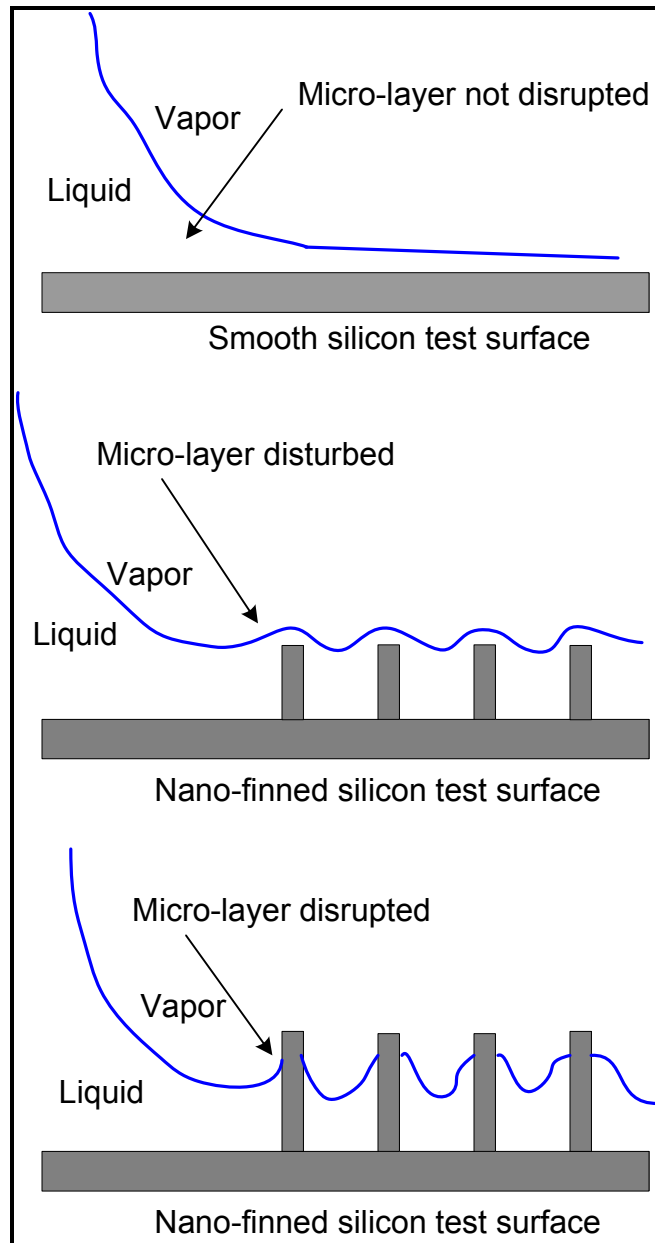
Fig. 49. Microlayer disruption/enhancement by nano-fins (figure not to scale).

From the results obtained in the present study, it can be argued that the nano-fins on the silicon test surfaces are influencing the nano-scale processes in the evaporating thin-film region (see Fig. 49). It can be hypothesized that the nano-fins (with heights greater than 100 nm) are able to disturb or disrupt the evaporating thin film region. By disturbing the evaporating film in the regions of maximum heat transfer, it is possible that the fins increase the surface area of contact of the micro-layer with the nano-fins (as part of the heated surface) and increase the heat transfer rates.

5. CONCLUSION

5.1 A synopsis

1. The effect of silicon nano-fins on the pool boiling heat transfer was explored in this investigation.

2. Experiments were conducted using PF5060 as the test fluid under saturation, 10 °C sub-cooling and 20 °C sub-cooling conditions using a constant-flux type apparatus. The boiling heat flux data for the nano-structured surfaces were compared with that of bare test surfaces.

3. Three different enhanced test surfaces were fabricated on 4 inch, double-side-polished silicon wafers using Step and Flash Imprint Lithography followed by either Reactive Ion Etching (RIE) or Deep Reactive Ion Etching (DRIE). The first test surface *"100 nm"* (fabricated using SFIL and RIE) contains an array of cylindrical silicon nano-fins 200 nm in diameter and with pitches of 1 μm in the longitudinal direction and 0.9 μm in the transverse direction. The second test surface *"336 nm"* (fabricated using SFIL and DRIE) consists of an array of silicon nano-fins in the form of frustums of cones. The fins have larger and smaller diameters of 100 nm and 65 nm respectively and have the same pitches as in the first case. The third test surface *"259 nm"* (also fabricated using SFIL and DRIE) again contains an array of cylindrical nano-fins 186 nm in diameter, the pitches being the same as in the first case. All the above test surfaces are named after the height of the nano-fins in each case. Upon fabrication, the

rectangular test surfaces are diced from the silicon wafer and loaded in the boiling set-up.

4. Raw experimental data revealed that the nano-finned surfaces enhance the heat flux in the nucleate boiling regime compared to the bare surfaces. The heat flux through the enhanced surfaces (q_w" W/cm^2) was found to be higher than that from bare test surfaces (q_b" W/cm^2). Due to the varying coverage of nano-fins on the three surfaces, data processing was undertaken to estimate the heat flux through the projected (plan) nano-patterned area (q_n" W/cm^2) and the heat flux through the total nano-patterned area (q_{nc}" W/cm^2). Subsequent to plotting heat flux data with heater temperature (thermocouple reading closest to the top of the copper block), the results show that the boiling curves for the different nano-structured test surfaces tend to overlap on each other in the nucleate boiling regime and also showing an overall enhancement compared to bare surfaces. This showed that the nano-scale transport processes were not influenced by the varying height of the nano-fins (with the merging of the curves) but were influenced by their presence (with the overall enhancement compared to bare test surfaces). Processing of the heat flux data (q_w") revealed that the nano-structured surfaces do not show significant enhancement in the film boiling regime. Thus the film boiling results are omitted while reporting q_n" and q_{nc}" with respect to both the heater termperature and wall superheat.

5. Surface temperature measurements were obtained for experiments using Thin-Film-Thermocouples in a separate study and correlations for the estimation of the

wall temperature were developed by taking advantage of its piecewise linear dependence on the copper block surface temperature. The correlations were employed in estimating the wall superheat for the experiments in the present study. The boiling curves were plotted for $q_w"$, $q_n"$ and $q_{nc}"$. The film boiling curves are neglected for $q_n"$ and $q_{nc}"$ because of the reasons mentioned above.

6. Contact angle measurements were performed with de-ionized water and PF5060 on selected surfaces and their variation with the nano-fin height was studied for both fresh test surfaces as well as those used for boiling experiments. Results are reported for de-ionized water alone because of the difficulty of measurement with PF5060 given its volatile and wetting natures. A variation in contact angle is shown with the variation in the nano-fin height for the fresh test surfaces. Measurements revealed that used test pieces made larger contact angles with de-ionized water subsequent to use in the boiling setup which did not depend on the height of the nano-fins on the surface.

5.2 Nano-scale transport processes

From the experimental results, the following heat transfer mechanisms were identified for the enhancement in heat transfer during pool boiling on the nano-structured surfaces.

5.2.1 Microlayer disruption

As discussed in detail in the previous section, the disruption/enhancement of the thin evaporating film under the vapor bubble has a high potential in being responsible for the

heat transfer enhancement given the high heat transfer coefficients close to the interline region (junction between the adsorbed non-evaporating film, adsorbed evaporating film, vapor bubble and the solid surface)

5.2.2 Increased number of active nucleation sites

Digital images captured during the boiling process (Fig. 39 and Fig. 40) show that more bubble nucleation occurs on the enhanced surface in the nucleate boiling regime, especially close to the CHF. This shows that the presence of nano-fins on the silicon surfaces presents an increased number of active spots for bubble nucleation and growth which in-turn may be responsible for the heat transfer enhancement relative to the bare test surface.

5.2.3 Enlargement in size of cold spots

Literature report suggests [47] that cold spots are formed due to the increased non-linear coupling of hydrodynamic and thermal mechanisms resulting in surface temperature fluctuations. The presence of the nano-fins on the silicon surface could potentially increase the size of the cold spots leading to increase in heat transfer rates compared to bare surfaces.

5.2.4 Contact angle variation

As discussed in the previous section, the contact angle that de-ionized water makes with the different enhanced test surfaces is influenced by the height of the nano-fins. As

discussed in the previous section, contact angle influences boiling incipience for highly wetting fluids like PF560 [9, 32] and the dynamic receding contact angle also influences the CHF condition during boiling [33]. Since the contact angle is increased in the presence of the nano-fins this could be a contributing factor that is responsible for the enhancement in pool boiling heat transfer.

5.3 Future directions

The present study shows that boiling is enhanced by nano-fins but the enhancement is independent of the height of the nano-fins for heights ranging between 100 nm and 336 nm. In addition, the fins slightly differ in diameter and shape as explained previously, however this is observed not to influence the boiling phenomenon significantly. Since the pitch between the fins for all the test surfaces was the same, the next step would be to fabricate test surfaces with variations in pitch and study their effect on pool boiling. For this, the SFIL process would need to be optimized to obtain the best possible coverage of nano-fins on the boiling surface.

On a similar note, the wall temperature measurements can be performed directly by fabricating TFTs on silicon wafers along with the nano-fins rather than approximating them using correlations. Perfecting this complicated process will present a great challenge since imprinting by itself is a very sensitive process, which is easily disrupted by very small particles (even in controlled environments). Fabricating and packaging TFTs along with nano-fabrication would lead to better understanding of the wall

temperature variations during boiling. The use of high-speed photography in place of standard digital photography can lead to a better understanding of the bubble dynamics. Once the most significant transport mechanisms are identified, numerical models incorporating the parameters affecting them can be developed and checked for validity with the experimental results.

Experimental data in the present study shows that the boiling process on the nanostructured surfaces is rather complex with different parameters interacting non-linearly in enhancing the transport processes. The effect of surface modification along with liquid sub-cooling is undertaken in the present study. Since the pool boiling process on nano-structured surface is sensitive to the different parameters identified in this study, the effective contribution from each parameter to the total heat flux enhancement needs to be explored in order to identify the dominant mechanism(s). A fundamental insight into these nano-scale transport processes can help in designing pool boiling heat flux enhancement schemes for various practical applications.

REFERENCES

[1] J. D. Cockcroft, "The temperature distribution in a transformer or other laminated core of rectangular cross section in which heat is generated at a uniform rate," *Proc. Cambridge Philos. Soc.,* vol. 22, pp. 759-772, 1925.

[2] A. Bar-Cohen, M. Arik, and M. Ohadi, "Direct liquid cooling of high flux micro and nano electronic components," *Proceedings of the IEEE,* vol. 94, no. 8, pp. 1549-70, 2006.

[3] I. E. Mouromtseff, and H. N. Kozanowski, "Comparative analysis of water-cooled tubes as class B audio amplifiers," *Institute of Radio Engineers -- Proceedings,* vol. 23, no. 10, pp. 1224-1251, 1935.

[4] S. G. Kandlikar, M. Shoji, and V. Dhir, eds., *Handbook of Phase Change: Boiling and Condensation*, Philadelphia: Taylor and Francis, 1999.

[5] R. F. Gaertner, and J. W. Westwater, "Population of active sites in nucleate boiling heat transfer," *Chem. Eng. Prog. Symp. Ser.*, pp. 39-48, 1960.

[6] R. F. Gaertner, "Photographic study of nucleate pool boiling on a horizontal surface," *Journal of Heat Transfer (U.S.);* vol: 87, pp: 17-29, 1965.

[7] J. G. Leidenfrost, "De Aquae Communis Nonnullis Qualitatibus Tractatus, (A Tract about Some Qualities of Common Water), Duisburg, 1756," *Pertinent portions reprinted in Journal of Heat and Mass Transfer,* vol. 9, pp. 1153-1166, 1966.

[8]   S. Nukiyama, "The maximum and minimum values of the heat Q transmitted from metal to boiling water under atmospheric pressure," *International Journal of Heat and Mass Transfer,* vol. 9, no. 12, pp. 1419-1434, 1966.

[9]   I. Mudawar, "Assessment of high-heat-flux thermal management schemes," in *ITHERM 2000. The Seventh Intersociety Conference on Thermal and Thermomechanical Phenomena in Electronic Systems (Cat. No.00CH37069),* Las Vegas, NV, USA, pp. 1-20.

[10]   I. L. Pioro, W. Rohsenow, and S. S. Doerffer, "Nucleate pool-boiling heat transfer. I: Review of parametric effects of boiling surface," *International Journal of Heat and Mass Transfer,* vol. 47, no. 23, pp. 5033-5044, 2004.

[11]   N. H. Afgan, L. A. Jovic, S. A. Kovalev, and V. A. Lenykov, "Boiling heat transfer from surfaces with porous layers," *International Journal of Heat and Mass Transfer,* vol. 28, no. 2, pp. 415-22, 1985.

[12]   H. H. Bau, and K. E. Torrance, "Thermal convection and boiling in a porous medium," *Letters in Heat and Mass Transfer,* vol. 9, no. 6, pp. 431-41, 1982.

[13]   A. E. Bergles, and M. C. Chyu, "Characteristics of nucleate pool boiling from porous metallic coatings," *Transactions of the ASME. Journal of Heat Transfer,* vol. 104, no. 2, pp. 279-85, 1982.

[14]   K. Cornwell, B. G. Nair, and T. D. Patten, "Observation of boiling in porous media," *International Journal of Heat and Mass Transfer,* vol. 19, no. 2, pp. 236-238, 1976.

[15] S. M. Lu, and R. H. Chang, "Pool boiling from a surface with a porous layer," *AIChE Journal,* vol. 33, no. 11, pp. 1813-28, 1987.

[16] S. G. Liter, and M. Kaviany, "Pool-boiling CHF enhancement by modulated porous-layer coating: theory and experiment," *International Journal of Heat and Mass Transfer,* vol. 44, no. 22, pp. 4287-311, 2001.

[17] S. Vemuri, and K. J. Kim, "Pool boiling of saturated FC-72 on nano-porous surface," *International Communications in Heat and Mass Transfer,* vol. 32, no. 1-2, pp. 27-31, 2005.

[18] J. Y. Chang, and S. M. You, "Boiling heat transfer phenomena from microporous and porous surfaces in saturated FC-72," *International Journal of Heat and Mass Transfer,* vol. 40, no. 18, pp. 4437-47, 1997.

[19] J. J. Wei, L. J. Guo, and H. Honda, "Experimental study of boiling phenomena and heat transfer performances of FC-72 over micro-pin-finned silicon chips," *Heat and Mass Transfer,* vol. 41, no. 8, pp. 744-55, 2005.

[20] J. J. Wei, and H. Honda, "Effects of fin geometry on boiling heat transfer from silicon chips with micro-pin-fins immersed in FC-72," *International Journal of Heat and Mass Transfer,* vol. 46, no. 21, pp. 4059-4070, 2003.

[21] K. N. Rainey, and S. M. You, "Pool boiling heat transfer from plain and microporous, square pin-finned surfaces in saturated FC-72," *Transactions of the ASME Journal of Heat Transfer,* vol. 122, no. 3, pp. 509-16, 2000.

[22]   S. Launay, A. G. Fedorov, Y. Joshi, A. Cao, and P. M. Ajayan, "Hybrid micro-nano structured thermal interfaces for pool boiling heat transfer enhancement," *Microelectronics Journal,* vol. 37, no. 11, pp. 1158-1164, 2006.

[23]   S. O. Ujereh Jr, I. Mudawar, P. B. Amama, T. S. Fisher, and W. Qu, "Enhanced pool boiling using carbon nanotube arrays on a silicon surface," *American Society of Mechanical Engineers, Heat Transfer Division, (Publication) HTD.* pp. 691-696.

[24]   A. F. Mills, *Basic Heat and Mass Transfer*, 2nd ed., Upper Saddle River, NJ: Prentice Hall, 1998.

[25]   S. Y. Chou, P. R. Krauss, and P. J. Renstrom, "Nanoimprint lithography," *Journal of Vacuum Science & Technology B: Microelectronics Processing and Phenomena,* vol. 14, no. 6, pp. 4129, 1996.

[26]   S. C. Johnson, "Step and flash imprint lithography: materials and process development," Ph.D dissertation, Department of Chemical Engineering, University of Texas, Austin, 2005.

[27]   N. Sinha, "Design, fabrication, packaging and testing of thin film thermocouples for boiling studies," M.S. thesis, Department of Mechanical Engineering, Texas A&M University, College Station, 2006.

[28]   S. J. Kline, and F. A. McClintock, "Describing uncertainties in SingleSample experiments," *Mechanical Engineering,* vol. 75, no. 1, pp. 38, 1953.

[29] D. Banerjee, and V. K. Dhir, "Study of subcooled film boiling on a horizontal disc: part I-Analysis," *Transactions of the ASME Journal of Heat Transfer,* vol. 123, no. 2, pp. 271-84, 2001.

[30] D. Banerjee, and V. K. Dhir, "Study of subcooled film boiling on a horizontal disc: part 2-Experiments," *Transactions of the ASME. Journal of Heat Transfer,* vol. 123, no. 2, pp. 285-93, 2001.

[31] H. S. Ahn, V. Sathyamurthi, N. Sinha, S. Lau, and D. Banerjee, "Boiling experiments on vertically aligned carbon nanotubes and using surface micromachined Thin Film Thermocouple (TFT)," *Collection of Technical Papers in Proceedings of the 9th AIAA/ASME Joint Thermophysics and Heat Transfer Conference,* San Francisco, California, USA, AIAA 2006-2916, 5-8 June, 2006, pp. 84-93.

[32] W. Tong, A. Bar-Cohen, T. W. Simon, and S. M. You, "Contact angle effects on boiling incipience of highly-wetting liquids," *International Journal of Heat and Mass Transfer,* vol. 33, no. 1, pp. 91-103, 1990.

[33] S. G. Kandlikar, "A theoretical model to predict pool boiling CHF incorporating effects of contact angle and orientation," *Transactions of the ASME. Journal of Heat Transfer,* vol. 123, no. 6, pp. 1071-9, 2001.

[34] R. N. Wenzel, "Resistance of solid surfaces to wetting by water," *Industrial & Engineering Chemistry,* vol. 28, no. 8, pp. 988-994, 1936.

[35] A. B. D. Cassie, and S. Baxter, "Wettability of porous surfaces," *Transactions of the Faraday Society,* vol. 40, pp. 546-551, 1944.

[36]   T. N. Krupenkin, J. A. Taylor, T. M. Schneider, and S. Yang, "From rolling ball to complete wetting: The dynamic tuning of liquids on nanostructured surfaces," *Langmuir,* vol. 20, no. 10, pp. 3824-3827, 2004.

[37]   B. V. Derjaguin, and Z. M. Zorin, "Optical study of the absorption and surface condensation of vapors in the vicinity of saturation on a smooth surface," in *Proc. 2nd International Cogress on Surface Activity (London),* vol. 2, pp. 145-152, 1957.

[38]   P. C. Wayner, Jr., Y. K. Kao, and L. V. LaCroix, "The interline heat-transfer coefficient of an evaporating wetting film," *International Journal of Heat and Mass Transfer,* vol. 19, no. 5, pp. 487-92, 1976.

[39]   P. C. Wayner, Jr., "A constant heat flux model of the evaporating interline region," *International Journal of Heat and Mass Transfer,* vol. 21, no. 3, pp. 362-4, 1978.

[40]   V. P. Carey, *Liquid-vapor Phase-change Phenomena*, New York: Hemisphere Publishing Co., 1992.

[41]   A. Mirzamoghadam, and I. Catton, "A physical model of the evaporating meniscus," *Transactions of the ASME Journal of Heat Transfer,* vol. 110, no. 1, pp. 201-7, 1988.

[42]   P. C. Stephan, and C. A. Busse, "Analysis of the heat transfer coefficient of grooved heat pipe evaporator walls," *International Journal of Heat and Mass Transfer,* vol. 35, no. 2, pp. 383-91, 1992.

[43]   S. DasGupta, J. A. Schonberg, and P. C. Wayner, Jr., "Investigation of an evaporating extended meniscus based on the augmented Young-Laplace equation," *Transactions of the ASME Journal of Heat Transfer,* vol. 115, no. 1, pp. 201-8, 1993.

[44]   P. C. Wayner, Jr., "The effect of the London-Van der Waals dispersion force on interline heat transfer," *Transactions of the ASME Journal of Heat Transfer,* vol. 100, no. 1, pp. 155-9, 1978.

[45]   M. Potash, Jr., and P. C. Wayner, Jr., "Evaporation from a two-dimensional extended meniscus," *International Journal of Heat and Mass Transfer,* vol. 15, no. 10, pp. 1851-63, 1972.

[46]   A. V. Mirzamoghadam, and I. Catton, "Holographic interferometry investigation of enhanced tube meniscus behavior," *Transactions of the ASME Journal of Heat Transfer,* vol. 110, no. 1, pp. 208-13, 1988.

[47]   D. Banerjee, G. Son, and V. K. Dhir, "Conjugate thermal and hydrodynamic analyses of saturated film boiling from a horizontal surface," *American Society of Mechanical Engineers, Heat Transfer Division, (Publication) HTD.* pp. 57-64.

VITA

Sharan Ram Sriraman was born as the first child to T. R. Sriraman and Parvathi Sriraman in Chennai, Tamil Nadu, India. He pursued his primary and secondary education in Vidya Mandir, Chennai. He obtained his Bachelor of Engineering degree in mechanical engineering from Anna University (Chennai), in the year 2005.

Sharan was admitted into the masters program in Fall 2005, with the Mechanical Engineering Department, Dwight Look College of Engineering at Texas A&M University, College Station. He joined the Multi Phase Flow and Heat Transfer Laboratory with Dr. Debjyoti Banerjee as his research advisor in Spring 2006.

He pursued his research in the field of Boiling Heat Transfer under the guidance of Dr. Debjyoti Banerjee and his committee members Dr. Kalyan Annamalai and Dr. Arul Jayaraman. He received his M.S. degree in mechanical engineering in December 2007.

Sharan R. Sriraman's permanent address is:

3C Akshaya apartments, 10 Krishnaswamy Avenue, Mylapore, Chennai

Tamil Nadu – 600 004, India